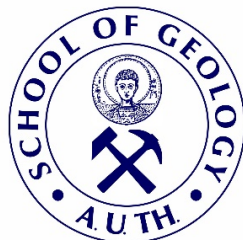




ARISTOTLE UNIVERSITY OF THESSALONIKI
SCHOOL OF GEOLOGY
DEPARTMENT OF
MINERALOGY-PETROLOGY-ECONOMIC GEOLOGY

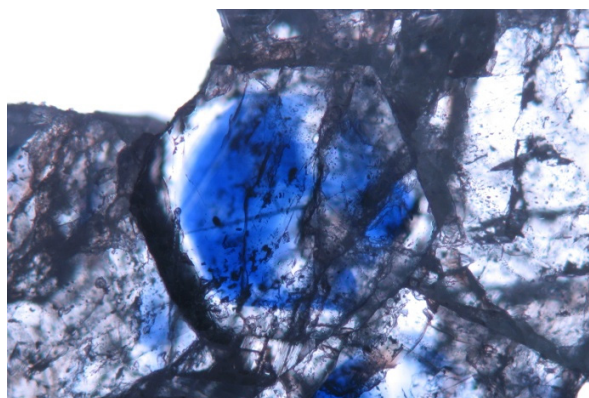


VILELMINI D. KARANTONI
Geologist

GEMOLOGICAL STUDY OF CORUNDUM
VARIETY OF RUBY AND SAPPHIRE FROM GREECE

MASTER THESIS

*POSTGRADUATE STUDIES PROGRAMME 'APPLIED AND ENVIRONMENTAL GEOLOGY',
DIRECTION: 'MINERAL RESOURCES-ENVIRONMENT'*



THESSALONIKI
2018





VILELMINI D. KARANTONI
Geologist
ΒΙΛΕΛΜΙΝΗ Δ. ΚΑΡΑΝΤΩΝΗ
Γεωλόγος

GEMOLOGICAL STUDY OF CORUNDUM,
VARIETY OF RUBY AND SAPPHIRE FROM GREECE
ΓΕΜΟΛΟΓΙΚΗ ΜΕΛΕΤΗ ΕΛΛΗΝΙΚΩΝ ΚΟΡΟΥΝΔΙΩΝ,
ΠΟΙΚΙΛΙΑΣ ΡΟΥΜΠΙΝΙΩΝ ΚΑΙ ΖΑΦΕΙΡΙΩΝ

Submitted to the School of Geology A.U.Th. in the program
'Applied and Environmental Geology', direction 'Mineral Resources-Environment'
Υποβλήθηκε στο Τμήμα Γεωλογίας Α.Π.Θ. στα πλαίσια
του Προγράμματος Μεταπτυχιακών Σπουδών 'Εφαρμοσμένη και Περιβαλλοντική Γεωλογία',
Κατεύθυνση 'Ορυκτοί Πόροι - Περιβάλλον'

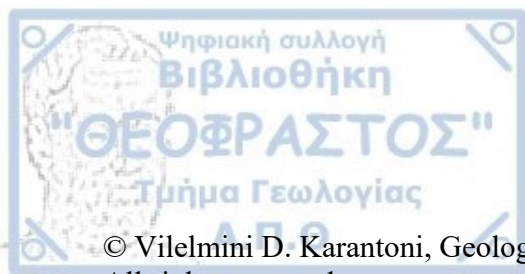
Oral Examination Date: 19/01/2018
Ημερομηνία Προφορικής Εξέτασης: 19/01/2018

Three-member Examining Board

Assistant Professor Vasilis Melfos
Supervisor (Aristotle University of Thessaloniki)
Assistant Professor Lambrini Papadopoulou
Member (Aristotle University of Thessaloniki)
Associate Professor Panagiotis Voudouris
Member (National and Kapodistrian University of Athens)

Τριμελής Εξεταστική Επιτροπή

Επίκουρος Καθηγητής Βασίλειος Μέλφος
Επιβλέπων (Αριστοτέλειο Πανεπιστήμιο Θεσσαλονίκης)
Επίκουρη Καθηγήτρια Λαμπρινή Παπαδοπούλου
Μέλος Τριμελούς Συμβουλευτικής Επιτροπής (Αριστοτέλειο Πανεπιστήμιο Θεσσαλονίκης)
Αναπληρωτής Καθηγητής Παναγιώτης Βουδούρης
Μέλος Τριμελούς Συμβουλευτικής Επιτροπής (Εθνικό και Καποδιστριακό Πανεπιστήμιο Αθηνών)



© Vilelmini D. Karantoni, Geologist, 2018

All rights reserved.

GEMOLOGICAL STUDY OF CORUNDUM, VARIETY OF RUBY AND SAPPHIRE FROM GREECE – *Master Thesis*

© Βιλελμίνη Δ. Καραντώνη, Γεωλόγος, 2018

Με επιφύλαξη παντός δικαιώματος.

ΓΕΜΟΛΟΓΙΚΗ ΜΕΛΕΤΗ ΕΛΛΗΝΙΚΩΝ ΚΟΡΟΥΝΔΙΩΝ, ΠΟΙΚΙΛΙΑΣ ΡΟΥΜΠΙΝΙΩΝ ΚΑΙ ΖΑΦΕΙΡΙΩΝ – *Μεταπτυχιακή Διπλωματική Εργασία*

Citation:

Karantoni, V.D., 2018. – Gemological Study of Corundum, Variety of Ruby and Sapphire from Greece. Master Thesis, School of Geology, Aristotle University of Thessaloniki, 142 pp.

Καραντώνη, Β.Δ., 2018. – Γεμολογική Μελέτη Ελληνικών Κορουνδίων, Ποικιλίας Ρουμπινιών και Ζαφειριών. Μεταπτυχιακή Διπλωματική Εργασία, Τμήμα Γεωλογίας Α.Π.Θ., 142 σελ.

It is forbidden to copy, store and distribute this work, in whole or in part, for commercial purposes. Reproduction, storage and distribution are permitted for non-profit, educational or research purposes, provided the source of origin is indicated. Questions concerning the use of work for profit-making purposes should be addressed to the author.

The views and conclusions contained in this document express the author and should not be interpreted as expressing the official positions of the Aristotle University of Thessaloniki.

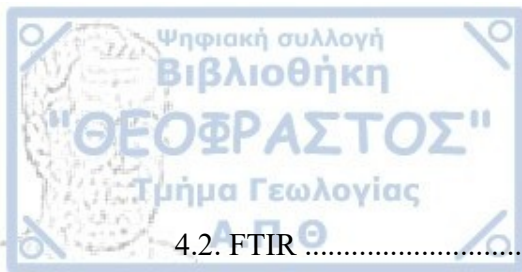
Cover Figure: Vilelmini Karantoni, present work







CHAPTER 1. INTRODUCTION	1
1.1. HISTORICAL ASPECTS	1
1.2. MINERALOGY, PHYSICAL PROPERTIES AND GEOCHEMISTRY	3
1.3. GEMOLOGICAL ASPECTS OF CORUNDUM	7
1.4. GEOLOGY OF CORUNDUM WORLDWIDE	9
1.5. TYPES OF CORUNDUM DEPOSITS AND WORLD OCCURRENCES	10
1.6. GREEK CORUNDUM OCCURRENCES	18
1.6.1. Rhodope Massif	18
1.6.2. Attico-Cycladic Massif	28
CHAPTER 2. MATERIAL AND METHODS	38
2.1. SAMPLE CATEGORIZATION	38
2.2. SAMPLES PREPARATION	44
2.3. ANALYTICAL TECHNIQUES	44
2.3.1. Petrology	45
2.3.2. IR Spectroscopy with Fourier Transform (FTIR)	45
2.3.3. UV-Vis-NIR spectroscopy	53
2.3.4. Energy Dispersive X-ray Fluorescence (EDXRF)	59
2.3.5. Fluid Inclusions	63
CHAPTER 3. RESULTS	65
3.1. PETROLOGY	65
3.2. IR SPECTROSCOPY	77
3.3. UV-Vis-NIR Spectroscopy	82
3.4. EDXRF	87
3.5. FLUID INCLUSIONS	89
CHAPTER 4. DISCUSSION AND CONCLUSIONS	95
4.1. PETROLOGY	95



4.2. FTIR	97
4.3. UV-Vis-NIR	100
4.4. EDXRF	103
4.5. FLUID INCLUSIONS	109
4.6. CLASSIFICATION OF STUDIED SAMPLES	111
4.7. CONCLUSIONS	113
 ABSTRACT	 115
REFERENCES	118



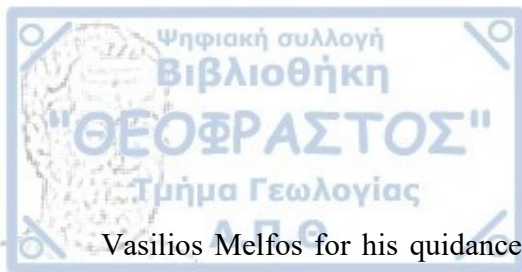
«Από τη γη προέρχονται οι πέτρες που ανάμεσά τους περιλαμβάνονται και οι πιο πολύτιμες...» Theophrastus “On stones (Περί Λίθων)”.

Rubies and sapphires have always been some of the most popular and expensive gemstones. From ancient times, they have been a subject of desire because of their unique appearance and variety of colors and have been used extensively in jewellery. In recent times, fine quality rubies and sapphires can reach prices that exceed the ones of comparably sized diamonds. Many papers have been published presenting the most important gem corundum occurrences around the world and examining their geology. However, fewer papers have been published on the gemology of ruby and sapphire deposits.

Though Burma, Kashmir and Sri Lanka are the kings of fine quality ruby and sapphire, these minerals can be found in many places around the world. In Greece, they are detected in the regions of Drama, Xanthi, Naxos and Ikaria. The geology of these occurrences has been studied to some extent by different authors. The initial aim of the current thesis was to focus on the gemology of the Greek occurrences. However, the geochemical results taken from the analytical methods that took place raised an interest on the geochemistry of these deposits. The final product is a combination of gemological and geochemical research on the Greek rubies and sapphires, resulting in a discrimination of the four occurrences and a presentation of their characteristic features.

The introduction includes a brief report of the history of rubies and sapphires, their geochemistry, physical properties and gemology, together with the geology of corundum deposits and their categorization. The chapter ends with an extensive reference in the Greek occurrences and their geology. The second chapter presents all the analytical techniques taken place for the examination of this thesis' samples, while in the third chapter the results given from each and every technique are presented and analyzed thoroughly. A general and broad discussion on the results is made in the fourth chapter, together with the presentation of the final conclusions.

This thesis is a result of personal effort and sacrifice, but also of unwavering help and support from a group of people. Countless thanks to: Dr. Stefanos Karampelas, Research Director of Bahrain Institute for Pearls and Gemstones (DANAT) for his guidance throughout the research process, as well as, the completion of the analytical measurements, Assistant Professor Dr.



Vasilios Melfos for his guidance, advising and supervision, Associate Professor Dr. Panagiotis Voudouris for the grant of the examined samples and his supervision, Assistant Professor Dr. Lambrini Papadopoulou for her supervision, Associate Professor Dr. Triantafyllos Soldatos for his counseling and assistance, Dr. Triantafyllia Zorba for her assistance in the completion of FTIR analysis of the samples and Aris Stamatiadis and Nikos Kipouros for their cooperation in the sample preparation process. Also, special thanks to the Department of Mineralogy-Petrology-Economic Geology and the Department of Physics of Aristotle University of Thessaloniki, as well as, the DANAT Laboratory in Bahrain, the GGTL Laboratory of Liechtenstein and the Gubelin Gem Lab in Lucerne for the provision of their facilities and analytical instruments. Finally, endless thanks and gratitude to my family for their support and understanding. And thank you, fellow reader for taking the time to read this thesis.



CHAPTER 1. INTRODUCTION

1.1. HISTORICAL ASPECTS

Along with diamonds and emeralds, rubies and sapphires have always been the most popular gemstones used in jewellery. Ruby and sapphire are two different varieties of the mineral corundum. There are two possible origins of the word corundum: the Sanskrit word “kurunvinda”, which means “hard stone” and the Tamil word “kurmidam” (Anthony et al., 1997; Giuliani et al., 2007). In 1782, Romé de L’Isle approached ruby and sapphire as the same mineral, and soon after Brisson’s publishing in 1787 of the two stones’ specific weight, René-Just Haüy suggested in 1805 that they are two varieties of the same mineral (Giuliani et al., 2007).

In the ancient book of Theophrastus “On Stones (Περὶ λίθων)” (4th century BC) the term adamas seems to have been used for several unusually hard minerals. According to Pliny (23-79 AD) this term applies to corundum, particularly the rock known as emery. At the time of Theophrastus (371-287 BC), the term “anthrax (άνθραξ)” was used to describe transparent precious stones of a deep red color, probably referring to ruby, red spinel, or red garnet. It is certain that the stone “σάπφειρος” as referred by Theophrastus or “sapphirus” as referred by Pliny, was not the same stone as the transparent blue gem now called sapphire. This stone can only apply to dark-blue lapis lazuli containing disseminated specks of pyrites confirmed also by Dionysius Periegetes (~117-138 AD).

The name ruby comes from the Latin word “ruber”, which means “red”. Ruby has been considered the most precious of the 12 stones created by God and was believed to hold the power of life. In Sanskrit, an ancient language spoken in India, ruby was called ratnaraj, which means

“king of precious stones” and was the symbol of permanent internal fire. References of rubies exist in Bible and in Roman scholar Pliny’s Natural History where he describes its hardness and density. Ancient Hindus used to believe that those who offered fine rubies to the god Krishna were granted rebirth as emperors, while those in possession of a fine ruby were perfectly safe. Warriors in Burma, used to possess rubies in order to gain invincibility in battles (Gia.edu).

The name sapphire probably comes from the word “sauriratna” in Sanskrit. Sapphire has always been connected with the color blue. In ancient Greece and Rome, it was believed to protect its owners from envy and harm, while in Middle Ages it symbolized loyalty, trust and Heaven for the clergy. The stone was also a symbol of chastity and was considered to bring peace between enemies and reveal the secrets of oracles. The term “hyacinthe” was used by Marbode (c. 1040-1123 AD) to describe all colored sapphires (Giuliani et al., 2007). The name “padpadradscha” which is used to describe an orange-pink sapphire, means “lotus flower” in Sinhalese, a language spoken in Sri Lanka, where these stones were first discovered (Gia.edu). Nowadays, every corundum with a color other than red is called sapphire.

Figures 1.1.1 and 1.1.2 illustrate the global production by volume of rubies and sapphires in 2005 according to Yager et al. (2008). However, the most productive and researched countries for rubies of gemological value today are Burma, Thailand, Madagascar and Mozambique. Burma's rubies are the most expensive in gem trade, while Mozambique's ones are the biggest in size. Accordingly, Kashmir, Burma, Sri Lanka and Madagascar have the largest production of blue sapphires of gemological value.

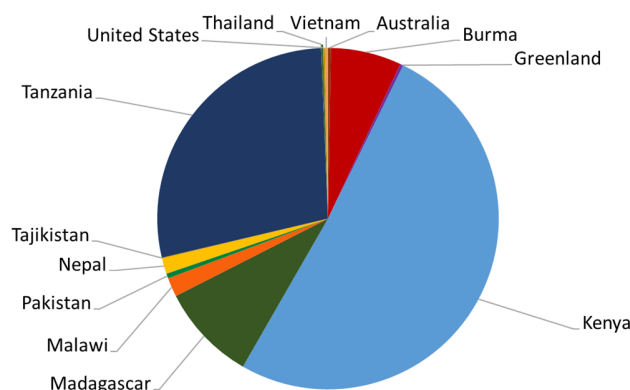


Fig.1.1.1. Global production by volume of rubies in 2005 (modified after Yager et al., 2008).

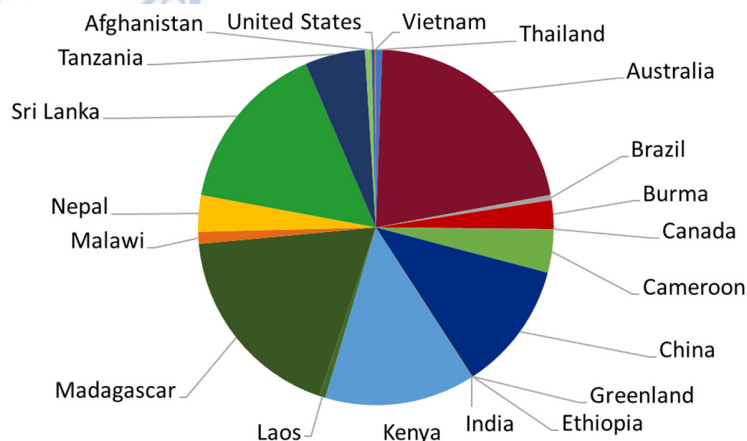


Fig.1.1.2. Global production by volume of sapphires in 2005 (modified after Yager et al., 2008).

1.2. MINERALOGY, PHYSICAL PROPERTIES AND GEOCHEMISTRY

Chemistry

Corundum is an aluminum oxide with chemical formula Al_2O_3 . The exact composition of corundum is 52.93 wt% Al and 47.07 wt% O. There are 12 Al atoms and 18 O atoms per unit cell ($Z=6$). Each Al^{3+} ion is bonded to 6 oxygen ions in an octahedron $[\text{AlO}_6]^{-9}$. Thus, only 2/3 of the octahedra are filled by Al cations (Fig. 1.2.1).

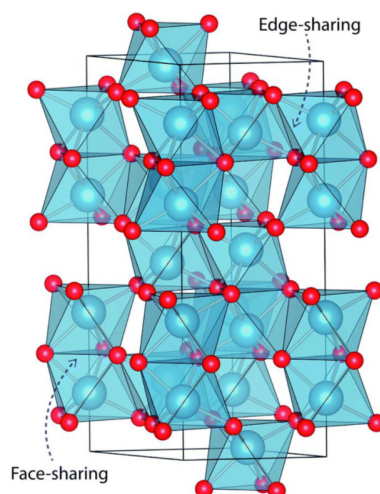


Fig.1.2.1. Crystal structure of corundum crystal. The red balls represent the O atoms and the blue balls the Al atoms, forming repeating units of the octahedron $[\text{AlO}_6]^{-9}$ (Phan, 2015).

Corundum crystallizes in the trigonal system (hexagonal scalenohedral class, $\bar{3}2/m$). The crystals can present different faces that correspond to the following crystalline forms: pinacoid $\{0001\}$, first-order hexagonal prism $\{10\bar{1}0\}$, second-order hexagonal prism $\{11\bar{2}0\}$, hexagonal dipyramid $\{hh\bar{2}hl\}$, ditrigonal scalenohedron $\{hk\bar{2}hl\}$ and rhombohedron $\{h0\bar{h}l\}$. It commonly occurs as tabular on $\{0001\}$ (Fig. 1.2.2e) or prismatic crystals (Fig. 1.2.2d). Often, it forms tapering hexagonal pyramids rounded into barrel shapes with deep horizontal striations (Fig. 1.2.2a, b). It can also crystallize with a particular texture called “trapiche”, formed by six skeletal arms which separate six sectors of growth (Fig. 1.2.2f) (Garnier et al., 2002).

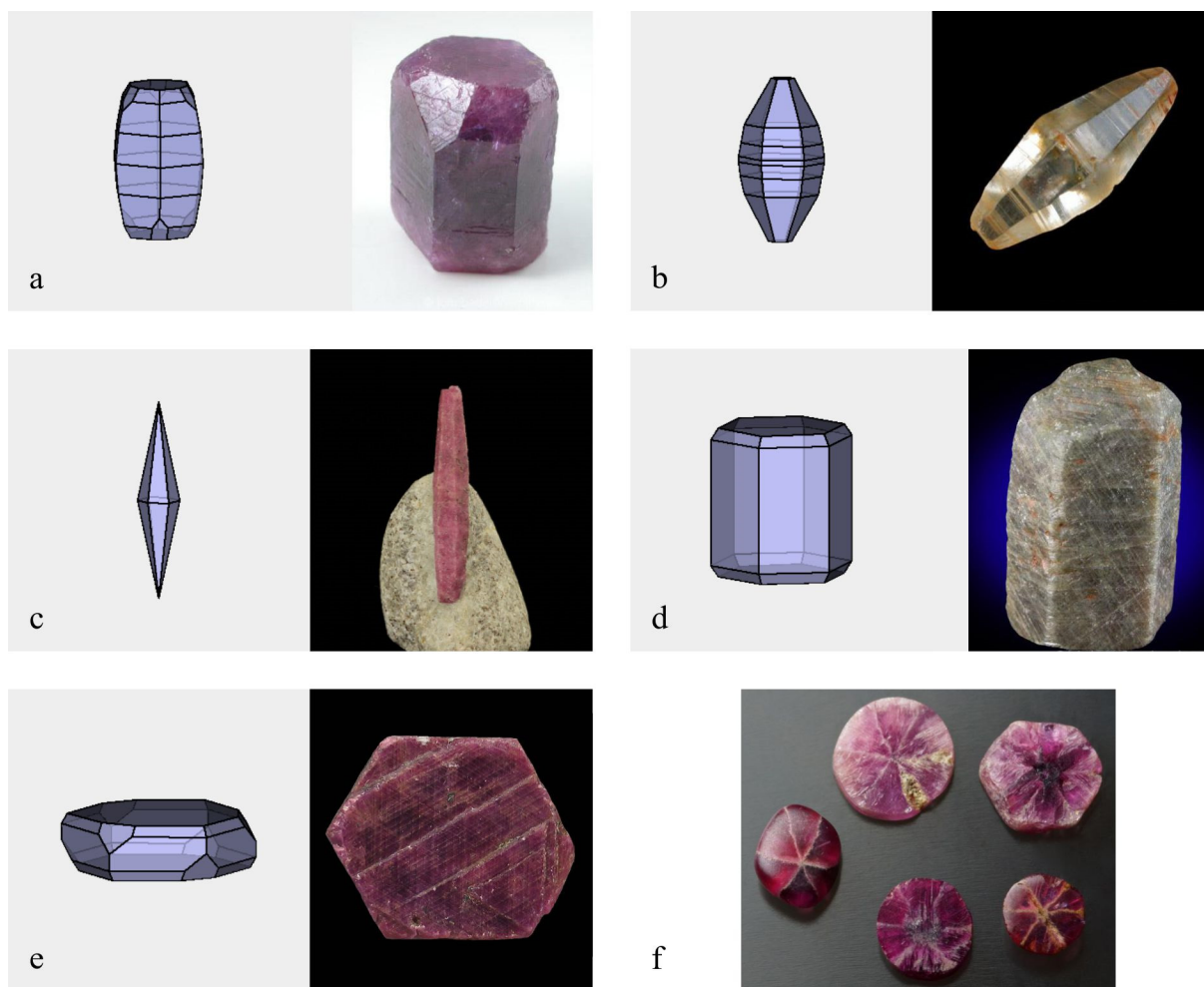


Fig. 1.2.2. a) hexagonal dipyramid (barrel-shapes), b) hexagonal dipyramid (tapering), c) hexagonal dipyramid, d) hexagonal prism, e) tabular hexagonal, f) trapiche rubies (photo: Minerals.net, Mindat.org, FMF Minerals forum).

On Mohs scale, corundum is defined to have 9.0 hardness, being the second hardest natural mineral after diamond. Because of its great hardness, the presence of cleavage in corundum is not common, though it can be present in colorless corundum along the rhombohedron $\{10\bar{1}1\}$ and prismatic $\{11\bar{2}0\}$ faces. Corundum crystals present a basal parting on $\{0001\}$ and a rhombohedral parting on $\{10\bar{1}1\}$, as well as a specific kind of parting due to exsolution of boehmite. The fracture is uneven to conchoidal. The crystals can also be granular and massive. Twinning on $\{10\bar{1}1\}$ is common, though this can be an exsolution phenomenon. Rarely, they can present contact or penetration twins on $\{0001\}$ or $\{10\bar{1}1\}$. Their tenacity can be characterized as brittle.

Corundum is an anisotropic mineral. It has an unusual specific gravity of 4.00 (± 0.02), depending on impurities, which is very high for a transparent mineral composed of low-atomic mass elements such as Al and O. Its melting point ranges between 2030 and 2050°C and its boiling point is at 3500°C. Colorless sapphire crystals are very good electric insulators (Hughes, 1997; Phan, 2015).

Optical properties

Corundum can be characterized as a transparent to translucent mineral. Under the polarizing microscope, basal sections present uniaxial character (-) with low first-order colors and in some cases, anomalous biaxial (possibly because of twinning). It presents weak pleochroism, being stronger when it is colored; $O > E$; relatively pure corundum has indices $n_{\omega}=1.767-1.772$, $n_e=1.759-1.763$; when biaxial $2V_x \leq 58^\circ$ (Anthony et al., 1997).

Color

Minerals can be idiochromatic or allochromatic. They are called idiochromatic when the color is a fundamental property directly related to one of each major constituent elements and is therefore constant and characteristic. Minerals that show a variation in color are called allochromatic. Corundum is an allochromatic mineral. In its purest form, is colorless. However, in nature, absolutely colorless corundum - in the true sense of the word - rarely exists. The

variety of color is wide: grey, brown, pink to pigeon-blood-red, orange, yellow, green, blue to cornflower blue, violet etc.

In allochromatic minerals, such as corundum, the array of colors is due to minor impurities, or trace elements, and other point defects in the crystal lattice that have been incorporated in the crystal during growth, or by diffusion processes in the laboratory. The trace elements can be the direct cause of colors (i.e. they are chromophores), or they can chemically interact with one another to create a new chromophore, or they can modify the strength of another chromophore (Emmet et al., 2017).

The main chromophore trace elements in corundum are: Cr, Fe, Ti and V. Cr^{3+} produces pink and red, while Fe^{2+} - Ti^{4+} pairs produce blue. The causes of color in corundum are presented in table 1.2.1 (Emmet et al., 2017 and references therein).

Table 1.2.1. Causes of color in corundum (modified after Emmet et al., 2017).

Apparent color / Chemistry

Pink to Red¹

Absorption spectrum of Cr^{3+} ions in octahedral symmetry in Al_2O_3 , replacing Al^{3+} in the lattice.

Blue²

Absorption spectrum of Fe^{2+} - Ti^{4+} ion pairs on nearest neighbor sites, replacing two Al^{3+} ions.

Yellow³

Individual Fe^{3+} ions and Fe^{3+} - Fe^{3+} ion pairs replacing Al^{3+} ions in the corundum lattice.

Orangish yellow⁴

Trapped hole- Cr^{3+} pair. Similar to the trapped hole- Fe^{3+} chromophore above.

Orange⁵

Combination of red color (Cr^{3+}) and one or more of the yellow causes above.

Violet/Purple⁶

A combination of red from Cr^{3+} and blue from Fe^{2+} - Ti^{4+} ion pairs.

Green⁷

Individual Fe^{3+} ions and Fe^{3+} - Fe^{3+} ion pairs plus the Fe^{2+} - Ti^{4+} ion pairs as described above.

Color-change⁸

Primarily the result from high concentrations of V^{3+} replacing Al^{3+} in the corundum lattice. Because of balanced transmission in both the green-blue and yellow-red, the gem shifts color depending on the spectral composition of the light source. Another possibility is in stones that have mixtures of blue (Fe^{2+} - Ti^{4+} ion pairs) and red (Cr^{3+}).

Dark Brown⁹

Mechanical coloration due to dark brown color of exsolved Fe-rich ilmenite plates (mainly black star and golden sheen sapphire).

1. McClure (1962), Fritsch and Rossman (1987), Powell (1966)
2. Townsend (1968), Fritsch and Rossman (1988), Moon and Phillips (1994)
3. Ferguson and Fielding (1971), Ferguson and Fielding (1972), Krebs and Maisch (1971)
4. Emmett et al. (2003)

5. Emmett et al. (2003)
6. Fritsch and Rossman (1988)
7. Emmett and Douthit (1993)
8. Schmetzer and Bank (1980)
9. Weibel and Wessicken (1981), Moon and Phillips (1991a)

1.3. GEMOLOGICAL ASPECTS OF CORUNDUM

Treatment

Ruby and sapphire are the two gem qualities of the mineral corundum. Natural rubies and sapphires are characterized by the presence of inclusions, cracks, and even irregular color distribution. For a potential gem corundum that is destined for the market, all these characteristics constitute flaws. Thus, different treatments are applied in the crystals in order to enhance their appearance. Less than 1% of all rubies and sapphires that are recovered from mines, actually end up to the market without any treatment. The most common treatments for rubies are: heat-treatment, dyeing, beryllium diffusion, flux healing and glass filling, while for sapphires are: simple and multiple heat treatment, thermal diffusion, beryllium treatment, surface diffusion, filled cavities or fissures and irradiation.

Synthetic corundum

The first attempt to create a synthetic ruby was made by Gaudin in 1837, by fusing $KAl(SO_4)_2$ at a high temperature with a small amount of Cr_2O_3 . In 1847, Ebelmen managed to create white sapphire by fusing Al_2O_3 in H_3BO_3 . In 1877, Frenic and Freil manufactured synthetic corundum, while later Frimy and Verneuil made artificial ruby by fusing BaF_2 and Al_2O_3 with a little Cr_2O_3 at "red heat". It wasn't until 1903 that Verneuil technique or flame fusion process was established as the first technique able to produce high quality gemstones for jewellery use. This technique, first developed for the synthesis of rubies, includes the heating of $(NH_4)Al(SO_4)_2 \cdot 12H_2O$ (ammonium alum) and $KCr(SO_4)_2 \cdot 12(H_2O)$ (chromium alum) in a furnace to 1000-1200°C. Al_2O_3 and Cr_2O_3 are released, forming powders which are mixed together, and then melted to yield a ruby boule (boule = term used to describe a synthetic gemstone crystal). Because of the high internal strain, the boule can be easily separated into two halves, each one providing several faceted rubies of 1-2 carats.

The Verneuil process followed for the synthesis of sapphires is the same, with the exception of the use of titanium and iron instead of chromium. Around 1950, another technique, the flux-growth process, made its appearance. In this process, rubies or sapphires are heated at 1300°C, in a platinum crucible in presence of a flux composed of litharge (a PbO mineral) and B_2O_3 (boron oxide), in order to dissolve into their ingredients. The mixture is cooled at 2°C per hour for 8

days. After this period, having reached a temperature of 915°C, the still molten flux can be poured off, creating ruby crystals with the use of dilute nitric acid, if needed. Because of the high cost of production and the long period of construction, the majority of synthetic rubies and sapphires are made by the Verneuil technique, even though flux-grown rubies and sapphires are of much higher quality than the Verneuil ones. In 1970, a technique including the heating of geuda, was developed. Geuda is a milky-white form of corundum, containing rutile, which under heating at 1500°C, is dissolved releasing titanium into the lattice of corundum, thus giving a blue coloration to the crystal. Further techniques used are the Czochralski pulling process and the hydrothermal process (University of Bristol, Gemdat.org).

Imitations

The most common natural imitations of ruby are red spinel, red garnet (pyrope) and red tourmaline (rubellite). All resemble ruby in appearance, though ruby is much harder in the Mohs scale. Many old famous red gemstones thought to be rubies, have proved to actually be red spinels, including the Black Prince's Ruby, once thought to be the largest ruby ever cut, which eventually has been confirmed to be a spinel. Colored glass has also been used as a ruby simulant. Especially during the 17th century, techniques such as the coloration of foil into red and its placing under the stone, were widely used.

Blue tourmaline, blue zircon and iolite (gem variety of cordierite) are the most common natural substitutes for blue sapphire, though their hardness in Mohs scale is lower compared to corundum. Other simulants are made from doublets-blue cobalt glass (the doublets can also be made from two small natural sapphires) with a crown of garnet or green sapphire and a pavillion of synthetic blue sapphire (Schumann, 2001).

1.4. GEOLOGY OF CORUNDUM WORLDWIDE

The genesis of the corundum deposits is linked to 3 main periods of formation associated with collision, rift and subduction geodynamics:

The Pan-African orogeny (750-450 Ma): Primary corundum deposits of magmatic and metamorphic type are linked to the Mozambique Belt. The Mozambique Belt, extending from East Antarctica through East Africa up to the Arabian-Nubian Shield, was the result of a late Neoproterozoic continental collision of the Himalayan type between Eastern and Western Gondwanaland, following the closure of the Mozambique Ocean (500-600 Ma). According to Giuliani et al. (2007), the metamorphic ruby and sapphire deposits from southern Madagascar have numerous geological similarities with those from East Africa (Mercier et al., 1999a, b), South India (Santosh and Collins, 2003) and Sri Lanka (Rupasinghe and Dissanayake, 1985).

The Himalayan orogeny (45-5 Ma): The Himalayan orogeny is a part of the major Alpine Orogeny that took place during the Late Mesozoic and the Cenozoic. The Tertiary collision of the Indian plate northward onto the Eurasian plate, resulted in the formation of the ruby deposits hosted in marbles, that are located in the Himalayan Mountain Belt. These marble-hosted ruby deposits represent the most important source of colored gemstones from Central and Southeast Asia (Garnier et al., 2006a, b).

The Cenozoic alkali basalt extrusions (65-1 Ma): The continental alkali basalt extrusions carried xenocrysts of Blue-Green-Yellow (BGY) sapphires and/or ruby up to the surface. Alkali basalt magmas are typically related to continental rifting over upwelling mantle related to hot spot activity (Graham et al., 2008). Such sapphire deposits occur in Nigeria, Cameroon, Air and Hoggar in Central Sahara (Wright et al., 1985), French Massif Central in the Limagne rift (Merle et al., 1998), and northern and central Madagascar (Rakotosamizany, 2003; Giuliani et al., 2007).

Gem quality rubies and sapphires originate both from primary (magmatic and metamorphic) and secondary (sedimentary) deposits (see tables 1.5.1, 1.5.2). Gem rubies come 50% from primary and 50% from secondary deposits, while 90% of gem sapphires come from secondary deposits.

1.5. TYPES OF CORUNDUM DEPOSITS AND WORLD OCCURRENCES

The classification of corundum deposits is a debated subject in the geological society. Several papers have been published proposing different classification schemes according to different features.

Some of these classifications are based on: the morphology of corundum (Ozerov, 1945), the geological context of the deposits (Hughes, 1990, 1997), the petrology of host rocks (Schwarz, 1998), the genetic processes that led to the formation of the corundum (Simonet, 2000), the genetic type of the deposits (Kievlenko, 2003), the type of deposit and the nature of the corundum host-rock (Garnier et al., 2004; Walton, 2004), the oxygen isotopic composition of the corundum (Giuliani et al. 2005).

Muhlmeister et al. (1998) suggested a classification for ruby deposits according to the chemical composition of ruby. Based on the concentrations of V, Fe, Ga and Ti in ruby, they categorized the deposits to a) basaltic when ruby is Fe-rich and V- and Ga-poor (Thailand, Cambodia), b) marble when ruby is V-rich and Ga- and Fe-poor (Afghanistan, Myanmar, Nepal, China) and c) metasomatic (Umba, Tanzania and Kenya). The concentrations of trace element and the lithology of host rock in the last category vary greatly (Giuliani et al., 2007).

The classification of gem corundum deposits is presented in the two following comprehensive tables compiled for the purpose of the current paper, respectively table 1.5.1 according to Giuliani et al. (2007) and Giuliani et al. (2012) and table 1.5.2 according to Simonet et al. (2008). The deposits in which ruby and sapphire appear as xenocrysts in the alkali basalt are classified as primary deposits by Giuliani et al. (2007) and as secondary deposits by Simonet et al. (2008). This is based on the magmatic or metamorphic-metasomatic origin of the corundum xenocrysts (Simonet et al., 2008).

Table 1.5.1. Classification of gem corundum deposits after Giuliani et al. (2007, 2012).

a) PRIMARY

(corundum crystallized in host-rock or transferred to the Earth's surface as xenolith)

MAGMATIC

(corundum originated by direct crystallization from magmatic melt)

Lithology	Occurrence
Magmatic (sensu stricto)	
Ruby and sapphire xenocrysts in intra-plate alkali basalts	<i>Africa:</i> SW Rwanda ³⁷ , Democratic Republic of Congo ⁶ , Kenya ⁷ , Nigeria ⁸ , Cameroon ⁹ , Algerian Sahara ¹⁰ , Madagascar ¹¹ , Niger ⁶² <i>America:</i> Colombia ¹⁶ <i>Asia:</i> China ² , Vietnam ³ , Cambodia ⁴ , Thailand ⁵ <i>Australia:</i> Queensland, Tasmania (E. Australia) ¹ <i>Europe:</i> France ¹² , Germany ¹³ , Czech Republic, Poland ¹⁴ , Loch Roag (Scotland) ¹⁵
Sapphire-bearing syenite as xenoliths in alkali basalts	
Ruby-bearing Grt-pyroxenite as xenoliths in alkali basalt	<i>Asia:</i> E. Thailand
Ruby and sapphire as xenocrysts in syenite pegmatites	<i>Africa:</i> Garba Tula (Kenya) ⁴² <i>America:</i> Ontario (Canada) ⁴³ <i>Europe:</i> Western Pyrenees of France ⁴⁴ , Norway, Russia <i>Asia:</i> India
Sapphire as xenocrysts in lamprophyres	<i>America:</i> Montana (USA) ⁴⁸ , Loch Roag (Scotland), Australia, Thailand, N. Britain, Ireland
Sapphire as xenocrysts in porphyry copper deposits	<i>America:</i> British Columbia (Canada) ⁶¹ , El Salvador (Chile) <i>Australia:</i> Tasmania ⁶⁰
Magmatic (metasomatic)	
Ruby-bearing pegmatites in mafics, ultramafics, black shales, schists or marbles	

Table 1.5.1. (Continued)

METAMORPHIC

(corundum formed by isochemical metamorphic reactions of Si-poor/Al-rich rocks and hydrothermal interaction or contact metasomatism)

Lithology	Occurrence
Metamorphic (sensu stricto)	
Ruby & sapphire-bearing meta-limestones	<p><i>America:</i> Sussex (USA)¹⁹ <i>Asia:</i> Azad Kashmir^{17,18}, Afghanistan¹⁸, Pakistan¹⁸, Tajikistan¹⁸, Nepal¹⁸, Myanmar¹⁸, N. Vietnam¹⁸, S. China¹⁸ <i>Africa:</i> Morogoro (Tanzania)²⁴ <i>Europe:</i> Ariege (France)²⁰, Xanthi (Greece)²¹, Campolungo (Switzerland)²², Urals (Russia)²³, Macedonia⁶³</p>
Ruby & sapphire-bearing gneisses (of granulite facies)	<p><i>Africa:</i> E. Africa²⁸, Madagascar^{29,31}, Mozambique³⁵ <i>America:</i> Brazil³² <i>Asia:</i> Sri Lanka, India^{30,31}, Japan³¹, E. Siberia³³, <i>Europe:</i> Russia³¹, Norway³¹</p>
Corundum in migmatites (anatexites)	<p><i>Africa:</i> Morogoro (Tanzania)⁴⁵</p>
Ruby-bearing amphibolites	<p><i>Africa:</i> Kenya⁵⁴, Mozambique⁵⁵, Madagascar⁵⁶, Longido (Tanzania)⁴⁹ <i>America:</i> N. Carolina (USA) <i>Asia:</i> India⁵², Pakistan⁵⁸, Japan⁵⁹ <i>Australia:</i> Australia⁵⁷ <i>Europe:</i> Kittila (Finland)⁵⁰, Greenland⁵¹, France⁵³</p>
Ruby in ultramafic rocks	<p><i>Africa:</i> S. Africa⁶⁴, Zimbabwe⁶⁵ <i>Australia:</i> N. Zealand⁶⁶</p>
Metamorphic (metasomatic)	
Ruby & sapphire-bearing desilicated pegmatites in skarns	<p><i>Africa:</i> Andranondambo (Madagascar)²⁷ <i>Asia:</i> Mogok (Myanmar)²⁵, Bakahuma (Sri Lanka)²⁶</p>

Table 1.5.1. (Continued)

Sapphire in plumasites	<i>Africa:</i> Kenya ³⁵ <i>America:</i> California (USA) ³⁴ <i>Europe:</i> France ³⁶
Ruby & sapphire-bearing desilicated pegmatites in mafic-ultramafic rocks	<i>Africa:</i> Mangari (S. Kenya) ⁴⁰ , Umba (Tanzania) ³⁷ , Kalalani (Tanzania) ³⁸ <i>Asia:</i> Kashmir (India) ³⁹ <i>Europe:</i> Urals (Russia) ⁴¹
Sapphire-bearing Bt-schist in feldspathic gneisses, ruby- & polychromesapphire-bearing cordieritite in charnockites	<i>Africa:</i> Sahambano (Madagascar) ⁴⁶ , Zazafotsy (Madagascar) ⁴⁶ , Ambatomena (Madagascar) ⁴⁷ , Iankaroka (Madagascar) ⁴⁷

b) SECONDARY

(corundum of detrital origin in primary deposits and found in sedimentary placer basins)

SEDIMENTARY

(corundum transported and concentrated in hydrographic traps through chemical weathering - eluvial - and erosion of primary deposits)

Lithology	Occurrence
Ruby- & sapphire-bearing placers in lamprophyre, alkali basalt, limestone fields	<i>Africa:</i> Ilakaka, Ambondromifehy, Vatomandry (Madagascar) <i>America:</i> Montana (USA) <i>Asia:</i> Mogok, Mong Hsu (Myanmar), Luc Yen, Yen Bai, Dak Nong (Vietnam), Ratnapura, Elahera (Sri Lanka) <i>Australia:</i> Queensland & New South Wales (Australia), Tunduru, Songea, Umba (Tanzania)



Table 1.5.1. References (Included in Giuliani et al. 2007, 2012)

1. Oakes et al. 1996, Sutherland 1996, Sutherland and Coenraads 1996
2. Keller and Keller 1986, Guo et al. 1992, Furui 1988
3. Smith et al. 1995, Poirot 1997, Garnier et al. 2005
4. Lacombe 1970, Jobbins and Berrangé 1981
5. Limkatrun et al. 2001
6. Frazier and Frazier 1990
7. Barot et al. 1989, Keller 1992
8. Irving and Price 1981, Kiefert and Schmetzer 1987
9. Lettermann and Schubnel 1970
10. Conquéré and Girod 1968
11. Lacroix 1922, Schwarz et al. 2000, Racotosamizanany 2003
12. Carbonel et al. 1973, Forestier 1993
13. Hochleitner 1998
14. Malíková 1999
15. Upton et al. 1983, Jackson, 1984
16. Keller et al. 1985
17. Malik 1994, Pecher et al. 2002
18. Hughes 1997
19. Dunn and Frondel 1990
20. Lacroix 1890
21. Hunstiger 1990
22. Hochleitner 1998
23. Kissin 1994
24. Hanni and Schmetzer 1991
25. Garnier et al. 2006b, Iyer 1953, Harlow 2001, Harlow et al. 2006
26. Silva and Siriwardena 1988
27. Hibon 1952, Kiefert et al. 1996, Milisenda and Henn 1996, Rakotondrazafy et al. 1996, Gubelin and Perett
28. Mercier et al. 1999b, Simonet 2000
29. Lacroix 1922, Rakotondrazafy et al. 1996
30. Santosh and Collins 2003
31. Schwarz 1998
32. Epstein et al., 1994
33. Grew et al., 1989
34. Lawson, 1903
35. Simonet, 2000
36. Forestier and Lasnier, 1969
37. Solesbury, 1967
38. Seifert and Hyrsl, 1999,
39. La Touche 1890, Atkinson and Kothavala 1983
40. Key and Ochieng 1991, Mercier et al. 1999a
41. Spiridonov 1998, Kievlenko 2003
42. Simonet et al., 2004
43. Field 1951, Kievlenko 2003,
44. Monchoux et al., 2006
45. Altherr et al., 1982
46. Giuliani et al. 2007b, Ralantoarison et al. 2006, Pezzotta 2005
47. Windley et al. 1994, Salerno 1992, Koivula et al. 1992
48. Voynic 1985, Hughes 1997, Brownlow and Komorowski 1988, Mayer and Mitchell 1988, Cade and Groat 2006, Mychaluk 1995, Gubelin and Koivola 1986
49. Dirlam et al. 1992
50. Haapala et al. 1971
51. Herd et al. 1969, Rohtert and Ritchie 2006
52. Janardharan and Leake 1974
53. Forestier and Lasnier 1969
54. Barot and Harding 1994
55. Andreoli 1984
56. Nicollet 1986
57. McColl and Warren 1980
58. Aboosally 1999
59. Morishita and Kodera 1998
60. Botrill, 1998
61. Simandle et al., 1997
62. Carbonel and Robin, 1972
63. Hunstiger, 1990
64. Hall 1923, Anhaesseeur 1978
65. Morrison 1972, Schreyer et al. 1981
66. Grapes and Palmer 1996

Table 1.5.2. Classification of gem corundum deposits after Simonet et al. (2008).

a) PRIMARY

IGNEOUS

Lithology	Occurrence
Sapphire- bearing Bt-Hb-gneisses	<i>Africa:</i> Garba Tula (Kenya) ¹
Sapphire-bearing anorthoclase xenoliths in trachytes, basalts, alkali basalts	<i>Australia:</i> Queensland (Australia) ¹² <i>Europe:</i> Cantal (French Central Massif), Scotland ¹³

METAMORPHIC

Lithology	Occurrence
Metamorphic (sensu stricto)	
Sapphire-bearing aluminous gneisses and granulites	<i>Africa:</i> S. Kenya ³ , Ilakaka (Madagascar) ⁵ , Tunduru-Songea (S. Tanzania) ⁴ <i>Asia:</i> Sri Lanka ²
Ruby & sapphire-bearing meta-limestones	<i>Asia:</i> Myanmar ¹⁴ , Afghanistan ¹⁵ , Pakistan ¹⁶ , Tajikistan ¹⁷ , Nepal ¹⁸ , Vietnam ²¹ , Kashmir ²² <i>Africa:</i> Morogoro (Tanzania) ²⁰ <i>Europe:</i> Urals ¹⁹
Ruby-bearing mafic granulites	<i>Africa:</i> Chimwadzulu Hills (Malawi) ²⁸ , Longido (Tanzania) ²⁵ , Losongonoi (Tanzania) ³ <i>America:</i> N. Carolina (USA) ²⁶ <i>Asia:</i> Karnataka (India) <i>Europe:</i> Chantel (France) ²⁷
Metasomatic	
Sapphire-bearing desilicated pegmatites (plumasites)	<i>Africa:</i> Kinyikim (Kenya) ⁶ , Mangare (Kenya) ⁷ , Umba (Tanzania) ⁹ <i>Asia:</i> Kashmir ⁸



Table 1.5.2. (Continued)

Ruby & sapphire-bearing desilicated gneisses in contact with ultramafics	<i>Africa:</i> S. Kenya ³ <i>Australia:</i> New Zealand ²⁴ <i>Europe:</i> Kangerdluarssul (Greenland) ²³
Sapphire-bearing skarns	<i>Africa:</i> E. Africa ³ , SE Madagascar ³⁰ <i>Asia:</i> Sri Lanka ²⁹
Anatectic	
Corundum-bearing anatexites	<i>Africa:</i> Morogoro (Tanzania) ¹⁰ <i>Europe:</i> N. Scotland ¹¹
SECONDARY	
IGNEOUS	
Lithology	Occurrence
Ruby & sapphire xenocrysts in alkali basalts: a) BGY sapphire suite, b) metamorphic suite	<i>Africa:</i> Africa ³⁴ <i>Asia:</i> China ³² , SE Asia ³³ <i>Australia:</i> ³¹ <i>Europe:</i> Czech Republic ³⁵
Sapphire-bearing ultramafic lamprophyre in limestone	<i>America:</i> Montana (USA) ⁴⁰

Table 1.5.2. (Continued)

SEDIMENTARY

Lithology	Occurrence
Ruby & sapphire as clasts in elluvial, alluvial and marine placers	<i>Africa:</i> E. Africa ³⁸ , Madagascar ³⁹ <i>Asia:</i> Sri Lanka ³⁶ <i>Australia:</i> E. Australia ³⁷

Table 1.5.2. References (Included in Simonet et al. 2008)

1. Simonet et al. 2004
2. Katz 1972, Dahanayake & Ranasinghe 1985, Mendis et al. 1993, Dissanayake and Rupasinghe 1993, De Maesschalk and Oen 1989, Dissanayake and Chandrajith 1999, Kröner 1991
3. Simonet 2000
4. Henn and Milisenda 1997
5. Schmetzer 1999, Milisenda et al. 2001
6. Parkinson 1974, Simonet 2000
7. Mercier et al. 1999, Simonet 2000
8. Peretti et al. 1990
9. Solesbury 1967, Seifert and Hyrs 1999
10. Altherr et al. 1982
11. Cartwright and Barnicoat 1986
12. Robertson and Sutherland 1992
13. Upton et al. 1999
14. Kane and Kammerling 1992, Peretti et al. 1996
15. Hughes 1994
16. Kazmi and O'Donoghue 1990
17. Smith 1998
18. Smith et al. 1997
19. Kissin 1994
20. Hanni and Schmetzer 1991, Muhongo and Errera 1993
21. Kane et al. 1991, Hauzenberger et al. 2003
22. Koltsov 2001
23. Garde and Marker 1988
24. Grapes and Palmer 1996
25. Game 1955, Simonet 2000
26. Ranson et al. 1992
27. Forestier and Lasnier 1969, Lasnier 1977
28. Andreoli 1984, Boehm 2004
29. Wells 1956, Silva and Siriwardena 1988
30. Schwarz et al. 1996, Kiefert et al. 1996, Gubelin and Peretti 1997
31. Coenraads 1992, Sutherland 1996
32. Keller and Keller 1986
33. Guo et al. 1996
34. Kiefert and Schmetzer 1987, Krzemnicki et al. 1996, Schwarz et al. 2000
35. Malkova 1999
36. Dahanayake 1980
37. Coenraads 1990
38. Henn and Milisenda 1997, Blauwet and Laurs 2005
39. Laurs 2000
40. Mychaluk 1995, Berg and Dahy 2002

1.6. GREEK CORUNDUM OCCURRENCES

The Hellenides constitute an integral part of the Alpine-Himalayan mountain chain, resulting from the convergence between the stable south European margin to the north and the north Gondwana passive margin to the south (Kydonakis et al., 2014). Geotectonically, the Hellenide orogen links the southern part of Balcan Peninsula (e.g. the Dinarides/Albanides) and Turkey (e.g. Pontides, Anatolides) (Melfos and Voudouris, 2017). The geodynamic evolution of Hellenides has been discussed to a great extend in literature (e.g. van Hinsbergen et al., 2005; Jolivet and Brun, 2010; Ring et al., 2010; Royden and Papanikolaou, 2011; Papanikolaou, 2013) and can be summarized into: a crustal thickening phase taking place during Mesozoic, followed by a continuous southward retreat of the subducting Hellenic slab, started back at the Eocene and still ongoing, that triggered large-scale extension concomitant with thrusting at the southern part of the Hellenic domain (Kydonakis et al., 2015c). The gem corundum deposits in Greece are spotted in two tectono-metamorphic units of the greater Hellenides Orogen: the Rhodope Massif and the Attico-Cycladic Massif (Voudouris et al., 2010; Graham et al., 2012; Wang et al., 2017).

1.6.1. Rhodope Massif

The Rhodope Massif is part of the Rhodope Metamorphic Province, which constitutes the hinterland of the Hellenic Subduction System (northeast Greece to southwest Bulgaria) (Kydonakis et al., 2014). Recently, it has been established as an ultra-high pressure metamorphic province (Mposkos and Kostopoulos, 2001; Perraki et al., 2006; Schmidt et al., 2010; Burg, 2012). The Rhodope metamorphic core complex (Fig. 1.6.1) represents a metamorphic dome, which has been affected and extruded by a wider extension, taken place at the northern part of the Aegean Sea from the Middle Eocene to Middle Miocene (Brun and Sokoutis, 2007). The complex has almost the shape of a triangle and it is bordered to the SW by the Jurassic and Cretaceous Chalkidiki Peninsula's metamorphosed rocks of the Serbo-Macedonian Massif and to the North by the eclogitic gneisses of Sidironero unit. Based on calculated P-T conditions for the metamorphic events and exhumation ages for different types of metamorphosed rocks, Mposkos and Krohe (2000) and Mposkos and Krohe (2001) divided the Rhodope Massif into: a) the upper tectonic and first exhumed (65-48 Ma) unit of Kimi, consisting of HP-HT sequences of migmatitic gneisses, intercalated layers of marbles, eclogitic amphibolites and meta-peridotites,

b) the subjacent units of Sidironero (central Rhodope) and Kehros (east Rhodope) with an exhumation age of 42-30 Ma, composed of para-gneisses, ortho-gneisses (often migmatitic), marbles, amphibolites, eclogites and ultramafics of various metamorphic grade, and c) the Pangeon unit (western Rhodope) (26-8 Ma), which constitutes the metamorphic core of Rhodope consisting mainly of marbles, ortho-gneisses, schists and amphibolites. Turpaud (2006) subdivided the central part of Rhodope Massif into the lower block of Thrace (Thracia Terrane), composed of Permo-Carboniferous orthogneisses and Triassic marbles, and the upper block of Rhodope (Rhodope Terrane), consisting of Early Jurassic ortho-gneisses. The two terranes are separated by the Nestos Suture Zone (or Nestos Shear Zone), an UHP sheared zone of 120 km length, which is extended to the north of the Nestos thrust fault with a vergence towards SW (Papanikolaou and Panagopoulos, 1981; Barr et al., 1999).

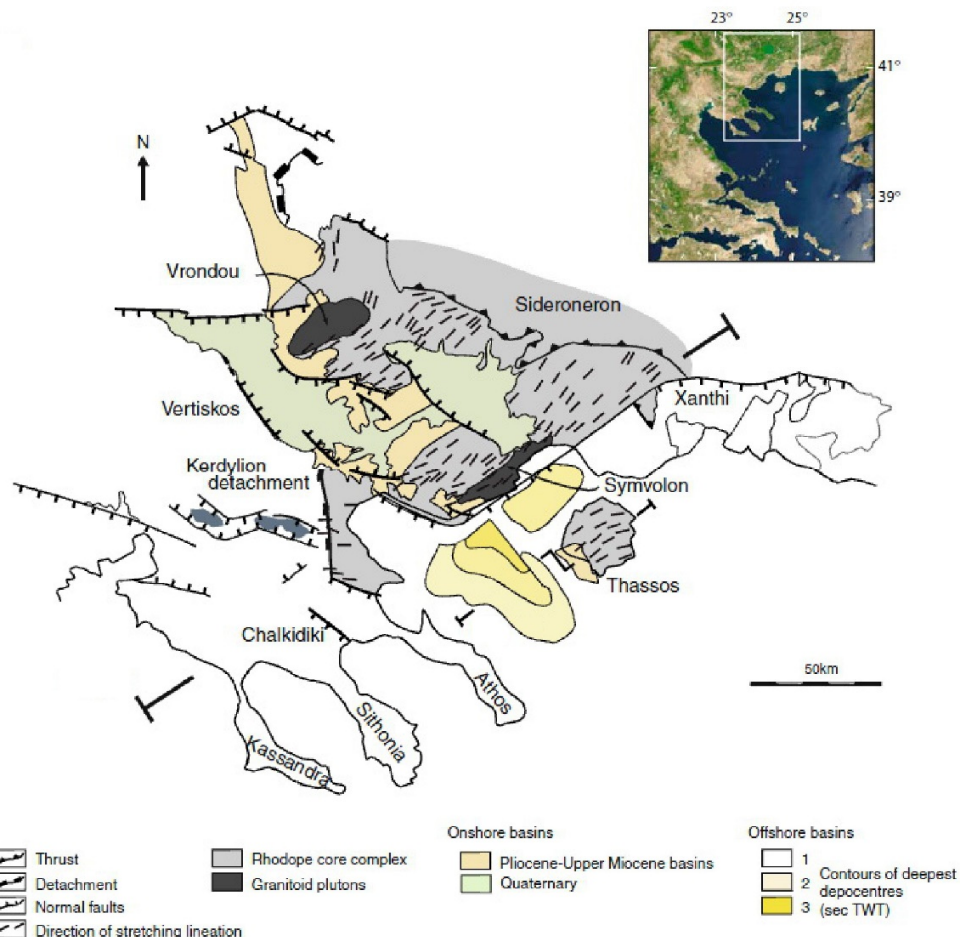


Fig. 1.6.1. Simplified map of Rhodope metamorphic core complex (after Brun and Sokoutis, 2007).

An additional division is the one proposed by Kydonakis et al. (2015a, b) and used by Melfos and Voudouris (2017), in which the Rhodope Massif is divided in three sub-domains: a) the Northern Rhodope Domain, b) the Southern Rhodope Core Complex and c) the Chalkidiki block. The latter, apart from the Kerdyllion Unit which belongs to the Southern Rhodope Core Complex, coincides with the Serbo-Makedonian Massif.

Rhodope Massif in its whole has undergone four main metamorphic episodes: a) a first general metamorphism of amphibolitic phase during Paleozoic, b) an UHP eclogitic metamorphism, c) a retrograde metamorphic path starting from an HP granulite-facies event during Jurassic (171 Ma), following an amphibolite-facies event during Cretaceous (79 Ma) (Bauer et al., 2007; Proyer et al., 2008), and one during Eocene (42 ± 2 Ma) (Moulas et al., 2013) and finally, d) a final greenschist metamorphic episode during Oligocene. Liati (2005) reported four high pressure (HPM) to ultra high pressure metamorphic (UHPM) events dated at: a) 149 Ma (U)HPM, b) 73 Ma (U)HPM, c) 51 Ma HPM and d) 42 Ma HPM. Large Tertiary plutonic blocks of felsic to intermediate composition intrude mainly the Sidironero unit, which, together with volcanic blocks of the same age of basaltic to rhyolitic composition, cause different phenomena of contact metamorphism. A more scrutinized description of the metamorphic and magmatic evolution of Rhodope Massif can be found extensively in literature e.g., Kolocotroni and Dixon, (1991); Jones et al., (1992); Liati and Seidel, (1996); Peytcheva et al., (1998); Barr et al., (1999); Mposkos and Kostopoulos, (2001); Soldatos et al., (2001, 2008); Reischmann and Kostopoulos, (2002); Ovtcharova et al., (2003); Marchev et al., (2004, 2013); Marchev et al., (2006, 2010); Mposkos et al., (2006); Perraki et al., (2006); Bauer et al., (2007); Brun and Sokoutis, (2007); Proyer et al., (2008); Jahn-Awe et al., (2010); Filipov and Marchev, (2011); Kydonakis et al., (2014, 2015a, b, c) etc.

In Rhodope Massif gem corundum deposits are located in two different regions along Nestos Suture Zone (Fig. 1.6.4): Gorgona-Stirigma (Xanthi area) and Paranesti (Drama area). They are associated with kyanite-bearing eclogites, which occur as lenses within Qz-Fds-gneisses and are characterized by the presence of omphacite, garnet, kyanite, phengite, rutile, apatite and zircon (Moulas et al., 2010). The presence of symplectites of corundum-plagioclase and spinel-plagioclase indicate conditions of decompression at pressures under 8 kbar and microscale metasomatism resulting from diffusion. The Paranesti occurrence refers to red corundum crystals

(rubies), while in Gorgona area corundum occurs in a wide range of colors, such as blue, pink, purple and orange (sapphires).

Voudouris et al. (2010) classified both occurrences as metamorphic deposits related to meta-limestones (Xanthi deposit) and mafic granulites (Paranesti deposit), according to Simonet et al. (2008), and supported the theory of their formation during the high temperature-medium pressure retrograde metamorphic episode of carbonates and eclogitic amphibolites during the Cenozoic collision and the creation of Nestos Suture Zone.

Gorgona-Stirigma (Xanthi)

In Xanthi area, Nestos Suture Zone (Fig. 1.6.2) is composed from the bottom to the top of the following lithological types: a) a lower 1 km-thick highly sheared “mélange” zone, consisting of amphibolites, Grt-Ky-schists, migmatites, orthogneisses and marbles, b) an 1 km-thick sequence of augen-gneisses, c) two layers of marbles intercalated with amphibolites and mylonitic amphibolites, d) a layer of ortho-gneisses, characterized by Bt-gneisses with highly migmatized base (Sidironero), which is penetrated by Skaloti’s granite and pegmatitic veins. Near the Greece-Bulgaria borders, in the area of Thermes, a Ky-eclogite outcrops near the contact between Bt-gneisses and Arda unit, indicating maximum pressures of 19 kbar (Liaty and Seidel, 1996).

Krenn et al. (2010) divide Nestos Suture Zone into an upper and a lower unit, based on the different tectonic and P-T-d paths that they followed. They suggest that the lower unit came from the Apulia Plate during Paleocene, while the upper unit is characterized by calc-alkaline magmatism, taken place during the first stages of Nestos Suture Zone’s exhumation. The central parts of this zone have undergone UHP conditions, before the initiation of exhumation process. Gautier et al. (2010) suggest a continuous thrusting tectonism along Nestos Suture Zone until 33 Ma ago, and a meta-orogenic extensional process starting after the 27 Ma. Nagel et al. (2010) indicate that Nestos Suture Zone constitutes the base of an Eocene thrusting wedge, that includes the higher tectonic units of Rhodope Massif and Internal Hellenides. The UHP units are not associated with the tectonic processes in the inner part of Nestos Suture Zone, and they probably represent tectonic wedges from an upper tectonic unit, which were merged with Nestos Zone during the thrusting event (Nagel et al., 2010). More thorough research on Nestos Suture Zone can be found in Liaty and Seidel (1996), Barr et al. (1999), Mposkos and Kostopoulos (2001), Perraki et al. (2006), Gautier et al. (2010), Krenn et al. (2010), Nagel et al. (2010) and Turpaud and Reischmann (2010).

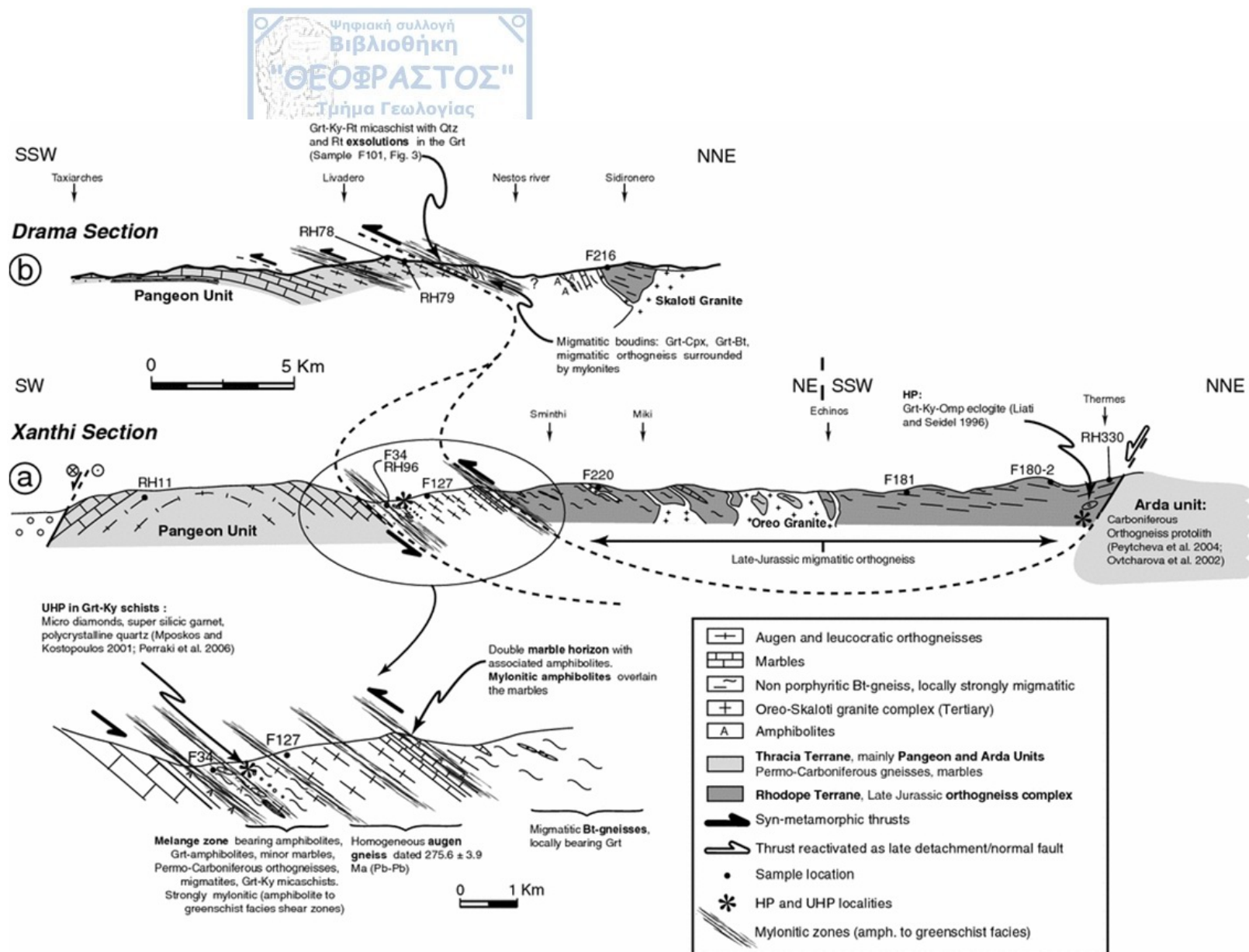


Fig.1.6.2. Simplified geological section of Nestos Suture Zone in the regions of Xanthi (a) and Drama (b). Section (a) depicts the exact tectonic spot of corundum-bearing layers of marbles in the upper units of Nestos Suture Zone (Turpaud and Reischmann, 2010).

The Gorgona-Stirigma corundum occurrence is stratiform and distributed in marble layers, reaching up to 50 m width, alternating with eclogitic amphibolites and gneisses (Liati 1986, 1988). The chemical composition of the marbles presents a wide variety, though their main lithological type is dolomite, with a mineral assemblage of calcite, dolomite, spinel, margarite, amphibole, chlorite, forsterite and Ni-tourmaline (Liati, 1988; Voudouris et al., 2010). Liati (1986, 1988) indicates also the assemblage of corundum, spinel, Al-pargasite, zoisite, margarite, chlorite, olivine and anorthite. Spinel occurs as a rim around corundum crystals. The color of spinel ranges from blue to green and brown. Its formation was based on the chemical reaction:



Zoisite is in equilibrium with anorthite and calcite indicating isobaric conditions for the chemical reaction:



Dehydration reactions of metapelites during the amphibolite-facies metamorphism produced the water, that took part in the aforementioned reactions, which during the shear deformational event moved to fill cracks of the rocks. According to Liati (1988), the conditions of burial metamorphism in the wider Xanthi area were 550-650°C and 7-9 kbar.

Ky-bearing pegmatitic veins crystallized under pressures of < 6 kbar, penetrate the marbles (Krenn et al., 2008). Re-crystallized lenses of plagioclase and white mica are also present in the Ky-pegmatites, together with corundum surrounded by plagioclase mantles, found along the cracks of kyanite crystals. During the last stages of the shear deformational event, the formation of corundum within kyanite crystals took place, in an environment of CO₂-rich fluids and pressures of 3-4 kbar (Krenn et al., 2008).

In some cases, corundum crystals occur within micro-shear zones along marble layers mainly in places rich in phyllosilicate minerals. They occur together a) with margarite (a Ca-rich mica member), b) with amesite (an Al-rich serpentine member); amesite forms euhedral crystals that intergrow with sapphire crystals or c) as single crystals in carbonate minerals, such as calcite and dolomite.

Sapphire is of pink, orange to blue color, usually of tabular or barrel-shaped euhedral form and reaches sizes of up to 4 cm (Fig. 1.6.3). In some cases, blue corundum alters to green spinel. Different contents of trace elements create the phenomenon of zoning or irregular color distribution in the sapphires. Red corundum occurrences have also been reported in this area.



Fig. 1.6.3. Pink (a) and blue (b) sapphire crystals hosted in marbles along Nestos Suture Zone at Gorgona-Stirigma area. Panagiotis Voudouris.

Paranesti (Drama)

At Paranesti, in situ corundum occurrences are located within Nestos Suture Zone (Fig. 1.6.4) (Wang et al., 2017). Paranesti area is located in the NE part of Macedonia region and in the western part of Rhodope Massif, approximately at the border between Sidironero and Pangeon units. At least two metamorphic episodes have left their imprint in the Drama area: one of high pressure ($P=11-12$ kbar) and one of Barrow type low pressure retrograde greenschist-amphibolite metamorphic episode ($T=520-580^{\circ}\text{C}$). The lithology of this area can be characterized by an upper unit of amphibolites, kyanite eclogites, garnet-kyanite gneisses, migmatites, metapelites, marbles, calcium-silica and ultramafic rocks and a lower unit of interchanging garnet-kyanite-mica schists and marble blocks, quartz-feldspar gneisses and rare amphibolites. Most rocks show signs of a boudinage structure. Pegmatitic veins intrude the upper layers, sometimes presenting the same folding with their adjacent rocks. Baziotis et al. (2007) documented an age of 65-63 Ma for the pegmatitic veins, while Liati et al. (2002) calculated a Rb-Sr isochron age of 65.4 ± 0.7 Ma. A K-Ar Eocene age of a hornblende from amphibolites in Central Rhodope is interpreted as the age of the Barrow type metamorphic episode (Liati, 1986). The corundum genesis is related to the amphibolitic-face metamorphic episode, thus bearing no relationship to the pegmatitic intrusions (Wang et al., 2017).

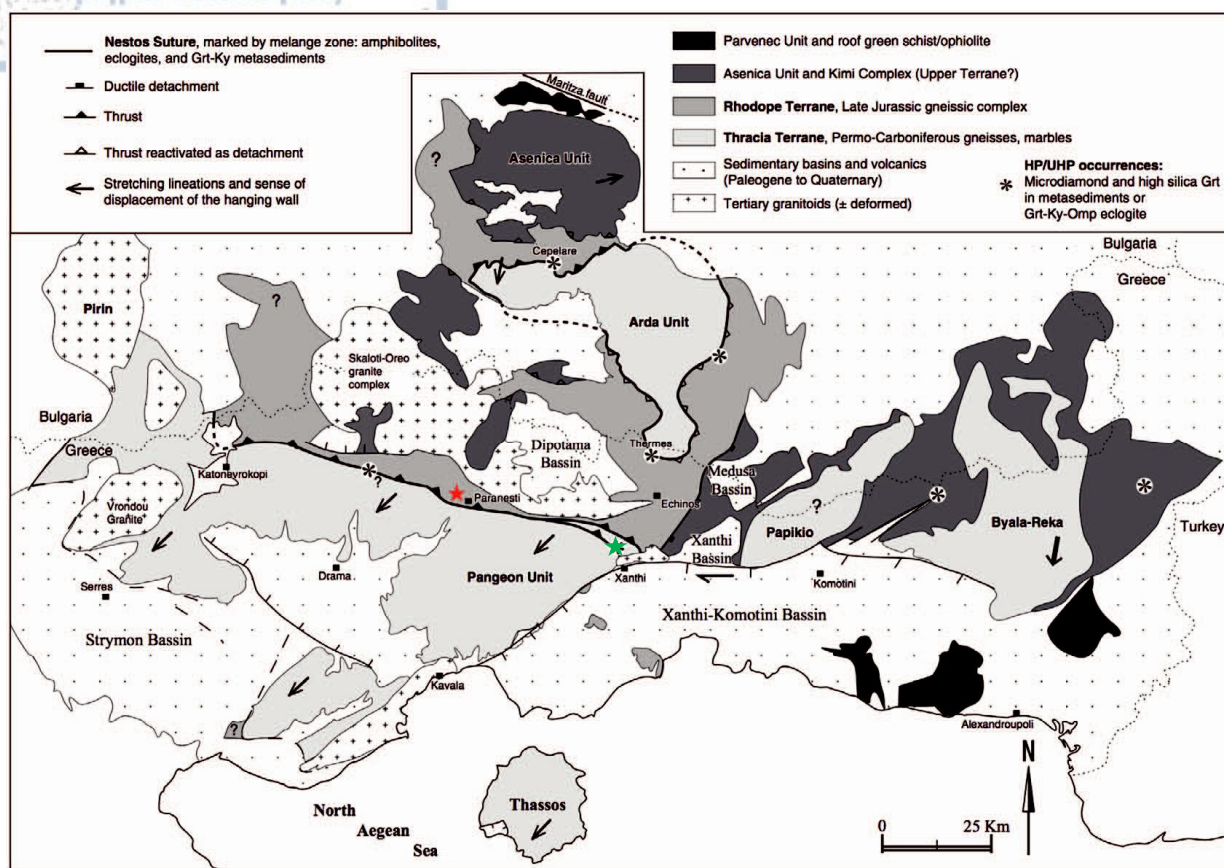


Fig.1.6.4. Geological map of the Rhodope Mountain Complex, with Paranesti (red star) and Xanthi (green star) occurrences located within the Nestos Suture Zone (adapted from Turpaud and Reischmann 2010) (Wang et al., 2017).

The data mentioned below are collected by research taken place in this area and presented in previous studies (Wang et al., 2017; Voudouris et al., 2010, etc.). The Paranesti corundum occurrence is stratiform (orientation parallel to the main regional foliation) and distributed mainly in ovoid-shaped boudin-like lenses of amphibole schist. The outcrops on the surface are spotted west of Perivlepto village at one hillside and one roadside location (Wang et. al., 2017). However, most of these occurrences are not of gem quality. In only two sites, the corundum crystals are actual rubies. In the first site, the corundum-bearing amphibole schist lenses are surrounded by a narrow clinoclone schist zone and occur together with boudins of corundum-kyanite-amphibole schists. The schists are intruded by white-colored quartz-feldspar-mica-garnet pegmatitic veins, which do not present characteristics of desilication. In the second site, the lenses are hosted by amphibolites, intercalated with kyanite-bearing quartz-plagioclase-amphibolite gneisses (formed in UHP conditions within Nestos Suture Zone, Mposkos and Kostopoulos 2001) and kyanite-amphibole-chlorite schists. Again, the transition from

amphibolitic lithology towards corundum mineralization is made through a clinocllore-rich schist zone of considerable width. Based on petrographical and chemical analysis, Wang et al. (2017) concluded that Paranesti rubies have formed within an ultramafic precursor, most possibly an aluminous clinopyroxenite, during amphibolite facies metamorphism. The estimated P-T conditions for their formation are $4 \text{ kbar} < P < 7 \text{ kbar}$ and $580^\circ\text{C} < T < 750^\circ\text{C}$ and with subsequent retrogression. The Paranesti ruby occurrence enhances the suggestion that rubies of metamorphic origin hosted in mafic-ultramafic rocks are associated with continental collision zones and can be used as plate tectonic suture zone indicators (Stern et al., 2013; Wang et al., 2017).

Ruby crystals, ranging in size from $<1 \text{ mm}$ to 50 mm size (average size $5\text{-}10 \text{ mm}$, with the exception of some crystals reaching sizes up to 3 cm) and of pale pink to deep red color (Wang et al., 2017), are detected in the center-core of these amphibole schist lenses (Fig. 1.6.5). In some crystals, the color presents an orange hue. Their morphology is mainly flat tabular with their basal planes paralleling the orientation of the main regional foliation (Wang et al. 2017), and less commonly prismatic and barrel-shaped. Most of them are heavily fractured or brecciated. They occur together with pargasite, which is the main amphibole of the assemblage, forming a similar image with Tanzania's rubies which are surrounded by zoisite. Most of them are surrounded by a margarite rim. Spinel appears as the main component of primary inclusions in the rubies. Kyanite grains occur close to the corundum grains. The association of ruby in this deposit is pargasite, chlorite (mainly clinocllore and rarely nimite), margarite, tremolite and/or monazite, while for the host rocks the assemblage is pargasite, anorthite, clinozoisite, chlorite and monazite.



Fig.1.6.5. Rubies (up to 3 cm) hosted in amphibole schist lenses of Paranesti area. Panagiotis Voudouris, Vasilios Melfos.

1.6.2. Attico-Cycladic Massif

The Attico-Cycladic Massif (Fig. 1.6.6) is a part of the Alpine Orogenic Belt of Internal Hellenides and consists of a complex pile of high pressure nappes/units. Images of a complete orogenic circle, including continental collision resulting in crust thickening and meta-horogenic collapse, can be detected in this massif (Dürr et al., 1978). On top of this complex of nappes overlays, with a tectonic contact, the Pelagonian zone, a unit of imbricated pre-Alpine crystalline rocks and Mesozoic marbles, also a part of the Internal Hellenides (Mountrakis, 1986; Doutsos et al., 1993; Anders et al., 2007).

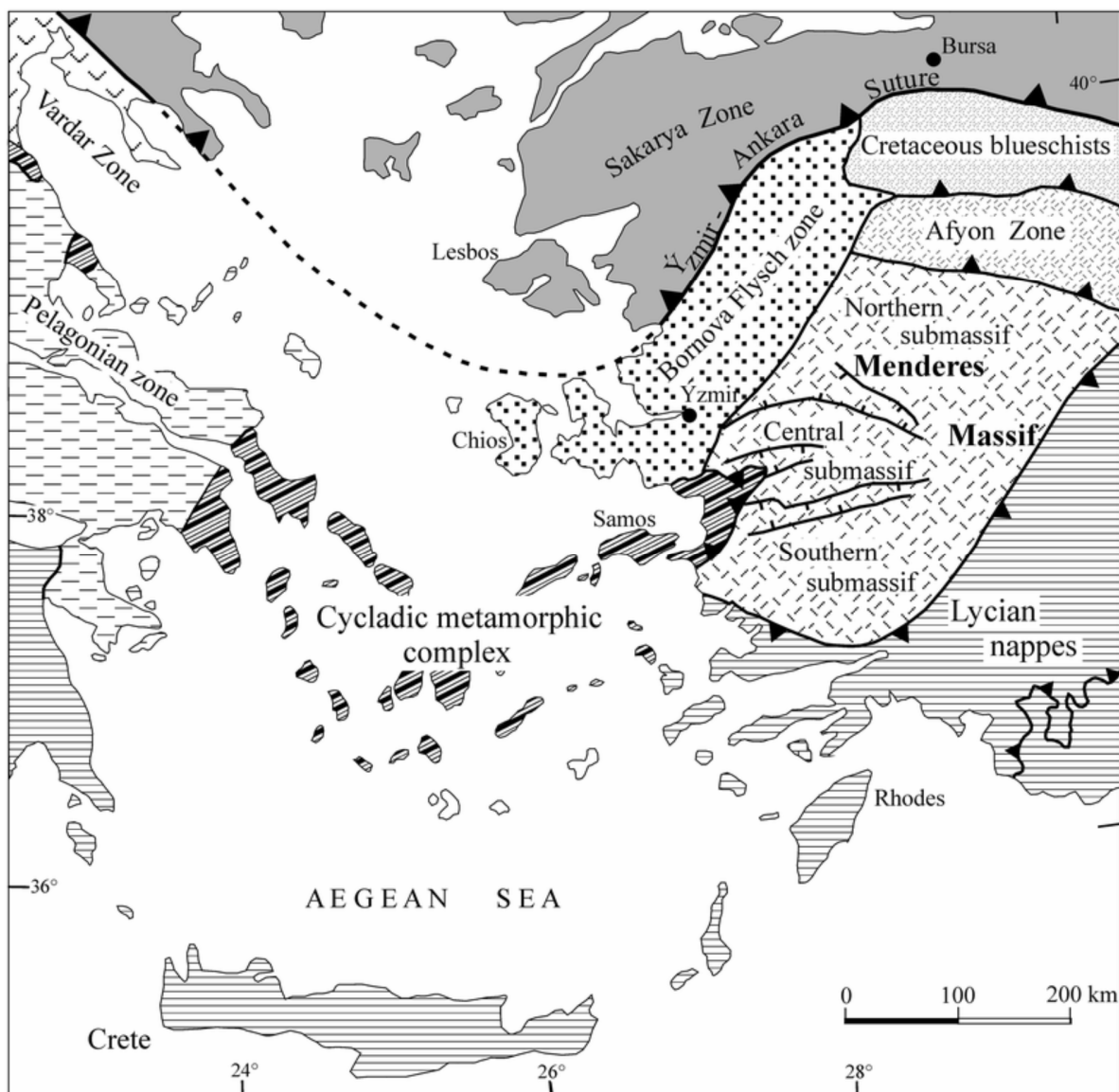


Fig. 1.6.6. Geological and tectonic map of the Attico-Cycladic Massif (modified after Okay, 2001).

According to Papanikolaou (1986, 1987), the Attico-Cycladic Massif can be subdivided into 4 main tectono-metamorphic units: a) the upper unmetamorphosed Cycladic unit, mainly detected at the islands of Paros, Naxos, Mykonos and Little Cyclades, containing Mesozoic carboniferous rocks superimposed by Paleocene flysch, b) the Eocene shield, consisting of low grade metamorphosed ophiolites and a lower tectonic mélange subunit, containing Permo-Triassic sediments, Early Cretaceous metamorphites penetrated by granitoid bodies and greenschists of unknown age, c) the Blueschist or “glauconitic” unit, divided into North and South Cyclades, containing Mesozoic passive margin sediments, submerged and metamorphosed during the Paleocene-Eocene in HP/LT conditions (Bröcker and Franz, 1998) following a retrograde Miocene Barrow type metamorphic episode (Keay et al., 2001) and d) the subjacent deep unit of gneisses, granites, amphibolites and other continental crust medium to high metamorphosed rocks, which represents the pre-Alpine Hercynian bedrock and is found under the South Cyclades unit in the islands of Ios, Paros, Naxos, Mykonos, Sikinos, Serifos and Andros forming metamorphic core complexes.

In the central Aegean, the Cycladic Blueschist unit is the most prominent tectonic unit and the most deeply exhumed unit in the region. It consists of 3 complex nappes, which from the upper to the lower are: a) an ophiolitic mélange, b) a Permo-Carboniferous to latest Cretaceous passive-margin sequence, and c) a Carboniferous basement, traces of which are found within the upper passive-margin sequence (Ring, 2007). In many areas, the Basal unit - a para-autochthonous unit consisting of thick blocks of Mesozoic marbles and schists hosting minor lenses of mafic and ultramafic rocks and overlain by a metapelitic or metaflysch sequence (Spanos et al., 2010) - occurs below the Cycladic blueschist unit forming tectonic windows (Godfriaux, 1968; Avigad and Garfunkel, 1989). The Cycladic blueschist unit has experienced two metamorphic facies: a) an Early Tertiary high-pressure metamorphism ($P \sim 15-20$ kbar and $T \sim 500 \pm 50^\circ\text{C}$) at approximately 55-45 Ma (Altherr et al., 1982) and b) one or more subsequent greenschist to low amphibolite-facies metamorphic events, associated with extension-decompression-uplift ($P \sim 4-7$ kbar and $T \sim 400 \pm 50^\circ\text{C}$) at 25-30 Ma (Altherr et al., 1982; Wijbrans et al., 1990; Ring and Lister, 2003; Tomaschek et al., 2003). Foster and Lister (2005), based on Ar-Ar dating, suggested for the area of Cyclades an eclogitic metamorphic event at 53-49 Ma, a blueschist event at 44-38 Ma, another transitional blueschist event at 35-30 Ma and finally a greenschist event at 22-19 Ma.

Arc-related volcanic rocks dated at approximately 11-6 Ma (Fytikas et al., 1984; Weidmann et al., 1984) and granitic bodies of I and S type ranging from 14-10 Ma (Altherr et al., 1982; Keay, 1998) and causing contact metamorphic phenomena, occur in the wider Cycladic region (Altherr et al., 1982, 1988; Mezger and Ockrusch, 1985; Henjes-Kunst et al., 1988; Avigad and Garfunkel, 1989; Faure et al., 1991; Lee and Lister, 1992; Skarpeis et al., 1992; Gautier et al., 1993; Boronkay and Doutsos, 1994; Gautier and Brun, 1994; Pe-Piper et al., 1997; Melfos and Voudouris, 2017), evidencing the Middle to Late Miocene merging of Cyclades into the magmatic arc of the SW retreating Hellenic subduction zone (Ring, 2007). According to Altherr et al. (1982), this magmatic activity, together with Barrow type metamorphic phenomena are related to the NE submerging of the Africa plate under the Apulia plate during the Early Tertiary.

In the Attico-Cycladic Massif, gem corundum deposits are detected in the islands of Naxos and Ikaria.

Naxos

Naxos metamorphic core complex is divided into four units: a) an alpine metamorphic unit containing alternating layers of marbles, schists and gneisses, b) a migmatitic dome, c) a granodioritic body and d) the upper unmetamorphosed tectonic unit. This metamorphic complex represents a thermal and tectonic dome which is elongated with an orientation of N-S (Fig.1.6.7). It consists of meta-carbonates, pelites, amphibolites, quartzites, meta-volcanic and meta-granitic rocks. Karstic bauxites and ultramafic rocks outcrop to a lesser extent. The imprinting of the second metamorphic event is increasing from the SE of the island, where low-T rocks still carry the relics of the first HP/LT metamorphic event, to the leucogneissic core of the dome where amphibolite-facies rocks, showing no signs of the prior event, are dominant. Blueschist relics at the SE rocks indicate temperatures ranging between 400 and 460°C at minimum pressures of 7-9 kbar (Feenstra, 1985) for the first Eocene event, while for the second high-T event taking place between 20-16 Ma, the temperatures range from 700°C at 6-8 kbar in migmatites and sillimanitic schists occurring in the core to 400°C at 6 kbar in marbles, schists, gneisses and amphibolites at the SE of the island (Jansen and Schuiling, 1976; Feenstra 1985; Wybrans and McDougall, 1988; Buick and Holland, 1989; Andriessen, 1991; Baker and Matthews, 1995; Lewis et al., 1998).

The migmatitic dome-like core is enveloped by peridotitic lenses in the adjacent gneisses and penetrated by pegmatitic veins. Petrographic research indicates that the peridotites were initially crystallized in the deeper mantle, from which they were transferred directly and assimilated from

the country rocks in great depths, during the Alpine orogeny and metamorphism of high-P (first metamorphic event). In this environment, they were stabilized in the spinel-hercynite field, undergone cooling under amphibolite-facies conditions ($T \sim 600^\circ\text{C}$) and finally re-heated and metamorphosed together with the country rocks during the second metamorphic event.

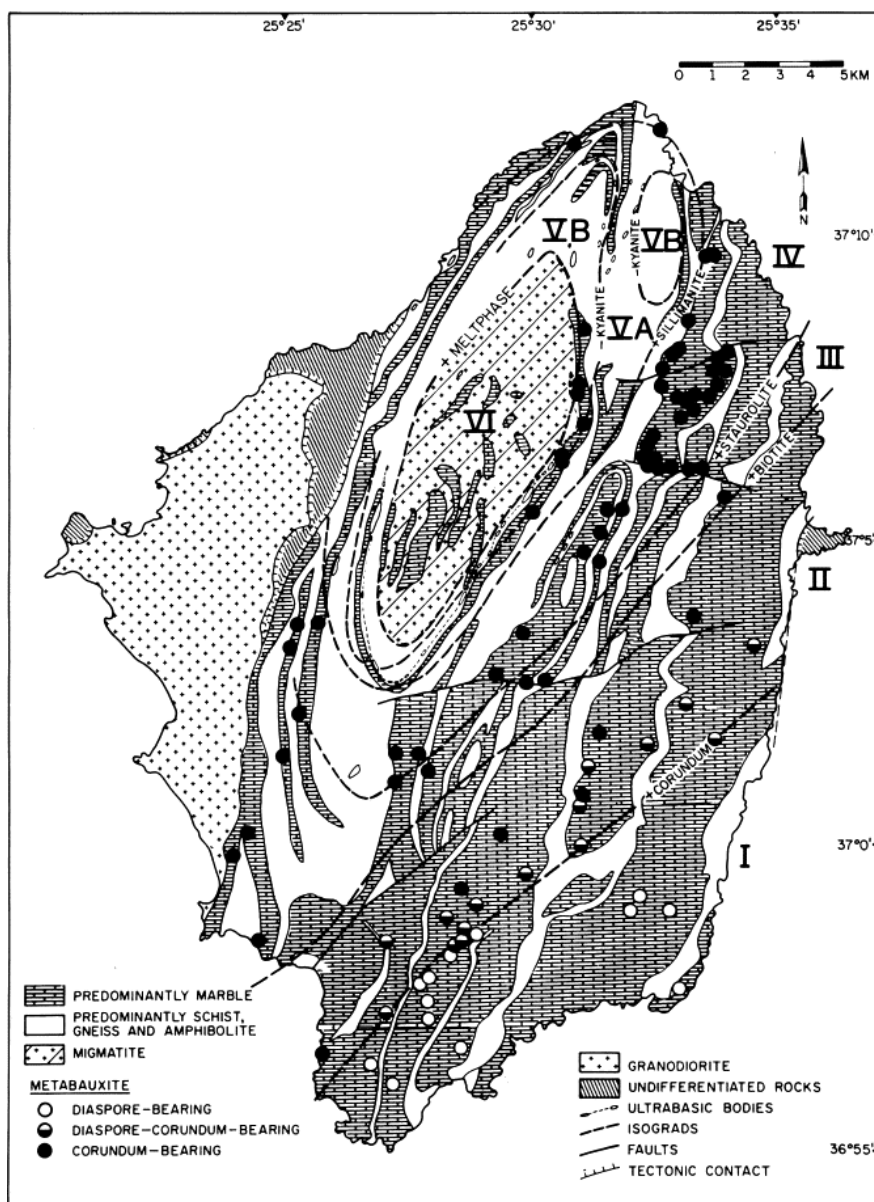


Fig.1.6.7. Naxos geological map depicting the main petrological types, isograds, metamorphic zones (I-VI) and metabauxitic occurrences (after Feenstra, 1985). The following isograds were recorded based on the increasing metamorphical grade of the second event: corundum occurrence ($\sim 420^\circ\text{C}$, in metabauxites), biotite occurrence ($\sim 500^\circ\text{C}$, in metapelites), Fe-staurolite occurrence ($\sim 540^\circ\text{C}$, in metabauxites and metapelites), sillimanite occurrence ($\sim 620^\circ\text{C}$, in metapelites), disappearance of kyanite ($\sim 650^\circ\text{C}$, in metapelites), liquid occurrence ($\sim 670^\circ\text{C}$, in metapelites).

According to Andriessen et al. (1991), aplites and pegmatites are of Early Miocene age (19-20 Ma), while Urai et al. (1990) indicate that they originated from the leucogneissic core and penetrated the lower units of the rocks affected by the second metamorphic event. Andriessen et al. (1991) also suggest that the aplites and pegmatites formed as a result of the crystallization of an in situ anatectic liquid, that was produced during the second metamorphic event. Naxos is the only island in Cyclades that the sub-continental mantle was part of the orogenic process. Thus, Naxos migmatitic core probably represents the deepest unit of Cyclades, having undergone the highest pressures during the collision and metamorphism of the first metamorphic event ($T=600^{\circ}\text{C}$, $P=14$ kbar).

In Naxos island corundum occurs in three different geological environments represented by different petrographic types.

a) Corundum formed by the dissociation of former diasporites, in meta-carstic bauxites during prograde general metamorphism (Feenstra and Wunder, 2002).

Naxos metamorphic zones were created during the second metamorphic event. The first corundum occurrence in metabauxites has been recorded as corundum-in isograd ($T\sim 420-450^{\circ}\text{C}$ and $P\sim 6-7$ kbar, Feenstra and Wunder 2002), which separates diasporites with the assemblage diaspore-chloritoid-muscovite-paragonite-calcite-hematite-rutile from emery characterized by the assemblage corundum-chloritoid-muscovite-paragonite-margarite-(Ti)-hematite-rutile. The thermic dissociation of diaspore and the formation of corundum ($\alpha\text{-AlOOH} \leftrightarrow \text{Al}_2\text{O}_3 + \text{H}_2\text{O}$), is the main reason for the dehydration of metabauxites (Feenstra and Wunder, 2002). The emery deposits in the metamorphic zones II and III are characterized by the assemblage corundum-chloritoid-hematite-rutile, while zone IV by the corundum-staurolite-biotite-kyanite-magnetite-ilmenite assemblage. In zone VB the emery deposits are penetrated by a grid of veins filled with retrograde minerals such as coarse-grained margarite, Fe-chlorite and clinozoisite. The corundum crystals are mainly blue sapphires (similar to Ikaria's blue sapphires). Their size increases along with the increase of the metamorphic grade of the second high-T event, reaching sizes of 1 cm in the VB zone close to the migmatite (Urai and Feenstra, 2001). Corundum-chloritoid intergrowths occur as a mantle in metabauxites, while the corundum crystals occur mainly in the contact between marbles and metabauxites.

b) Corundum in spinel-bearing dolomites, similar to the Xanthi deposits.

Jansen (1978) noticed the presence of Mg-poor calcite+spinel as a reaction-mantle between Mg-rich calcite and residual corundum, indicating formation of spinel in place of

corundum+dolomite. Naxos migmatitic core is rich in spinel-bearing dolomites, in which spinel crystals are separated from the calcite of the host rock by corundum+dolomite mantles, and they are often surrounded by Mg-chlorite+pargasite (Buick and Holland, 1991). Analytical data show a synchronous formation of Mg-chlorite+pargasite in place of spinel+calcite. The whole process is characterized by the reaction:



indicating conditions of cooling under low X_{CO_2} or isothermal CO_2 entrance in the system. All the aforementioned imply partial dissociation of Mg-spinel+calcite into corundum+dolomite during the retrograde metamorphism of spinel-bearing dolomites.

c) Corundum-albite rich bodies in plumasites formed by the interaction between pegmatites and ultramafic rocks (Voudouris et al., 2010; Graham et al., 2012).

Naxos migmatitic core is surrounded by a discontinuous block of ultramafic lenses, representing a thrust zone along which the metamorphic complex lies on top of pre-alpine bedrock (Van der Maar and Jansen, 1983; Andriessen et al., 1987). This plastic shear zone resulted in extension and partial exhumation of the migmatitic complex (Keay et al., 2001). According to Jansen and Schuiling (1976), the pegmatites penetrating the ultramafic bodies in the sillimanite stability zone, are desilicated and composed of phlogopite, anorthite, corundum (blue, transparent, pink, green), chlorite, zoisite, tourmaline and beryl. Anorthite crystals are composed almost entirely of anorthite (98% An), while margarite can be found in places.

The meta-peridotites occur as lenses of 1-10 m size and are surrounded by blackwalls (monomineralic metasomatic zones of considerable width that are intensely foliated) which formed at the contact between the meta-peridotites and the surrounding sillimanitic gneisses (Katzir et al., 2002). The metasomatic zoning, from the gneisses to the meta-peridotites, consists of phlogopite-actinolite-anthophyllite. In places, the metasomatic processes have wiped out the peridotites, leaving the blackwalls as the only remnant of a pre-existent ultramafic protolith. According to Katzir et al. (2002), in Korono, a zone of blackwalls consisted of phlogopite of a few cm, covers the boundaries of aplitic rocks. Korono blackwall is a result of a sequence of metasomatic events, starting from the highest metasomatism during the second metamorphic event and continuing till the aplitic intrusion. The anthophyllitic blackwalls probably formed during the maximum conditions of the second metamorphic event and recrystallized during the retrograde fluid intrusion. The aplitic-pegmatitic veins represent a system that channeled fluids through the leucogneissic core to the lower metamorphic unit (Katzir et al., 2002). These

retrograde silicic fluids resulted in the metasomatization of peridotites and in situ recrystallization of the peridotitic blackwalls (Katzir et al., 2002).



Fig.1.6.8. Corundum-bearing plumasite, containing sapphire mega-crystals within a white plagioclase matrix of the main rock. Tourmaline and biotite (black spots) complete the mineral assemblage. Panagiotis Voudouris.

Blue sapphire crystals are hosted within the contact between the pegmatites and the meta-peridotite (blackwalls), where they are enveloped by the assemblage oligoclase/labradorite-orthoclase-muscovite and also by phlogopite and chlorite. The plumasites are also the hosts of blue sapphire (sapphire, albite and zircon are surrounded by margarite, muscovite, tourmaline, illite and chlorite). The sapphire crystals reach sizes up to 3 cm (Voudouris et al., 2010) (Fig. 1.6.8).

Ikaria

Ikaria is an island at the eastern part of the Aegean Sea (Fig. 1.6.9) and according to Papanikolaou (1978) and Iliopoulos (2005), three main tectonic units can be distinguished: a) the upper Kefala unit, composed mainly of carbonates, b) the middle Messaria unit, consisting of the Petropoulos marbles and phyllites and the Pounta dolomite and c) the lower Ikaria unit, comprised of the upper Pounta marble, the Plagia gneisses and the lower Nikari marble. Ring (2007) introduces also the non-metamorphosed Fanari nappe, as the upper tectonic unit in Ikaria island and refers to Kefala formation as a subunit included in the bigger Messaria unit. The tectonic structure of the island is characterized by a 300-500 m thick ductile extensional shear zone, the Messaria shear zone, and two associated brittle detachment faults, the Messaria and the

Fanari faults (Ring, 2007). According to Dürr et al. (1978), the Fanari nappe belongs to the Upper unit of the Cycladic zone and consists of Pliocene conglomerates containing pebbles of metamorphic rocks, which are not exposed on Ikaria island. Altherr et al. (1982) report metabauxite-bearing marbles with small serpentinite lenses, graphite-rich calcite-mica schists, chloritoid-kyanite-bearing phyllites, quartzites and greenschists as the main rock types occurring in the Messaria nappe. The Kefala unit consists mainly of marbles bearing Early Triassic fossils and occurs as a small outcrop in the central part of Ikaria (Ring, 2007). The Ikaria nappe, a more than 1000 m thick unit, is comprised of a big sequence of metapelites, small layers of marbles, calc-silicate rocks, amphibolites, quartzites and metapegmatites. Two synkinematic granitic bodies intrude this unit: a) an I-type Bt-granite (Raches granite) in the western part of the island, with K-Ar ages of 22.7 Ma (Altherr et al., 1982) and b) a S-type Bt-Ms-granite (Xilosirtis granite) in the southern part of the island, with Rb-Sr ages of 18.1 Ma (Altherr et al., 1982, Boronkay and Doutsos, 1994).

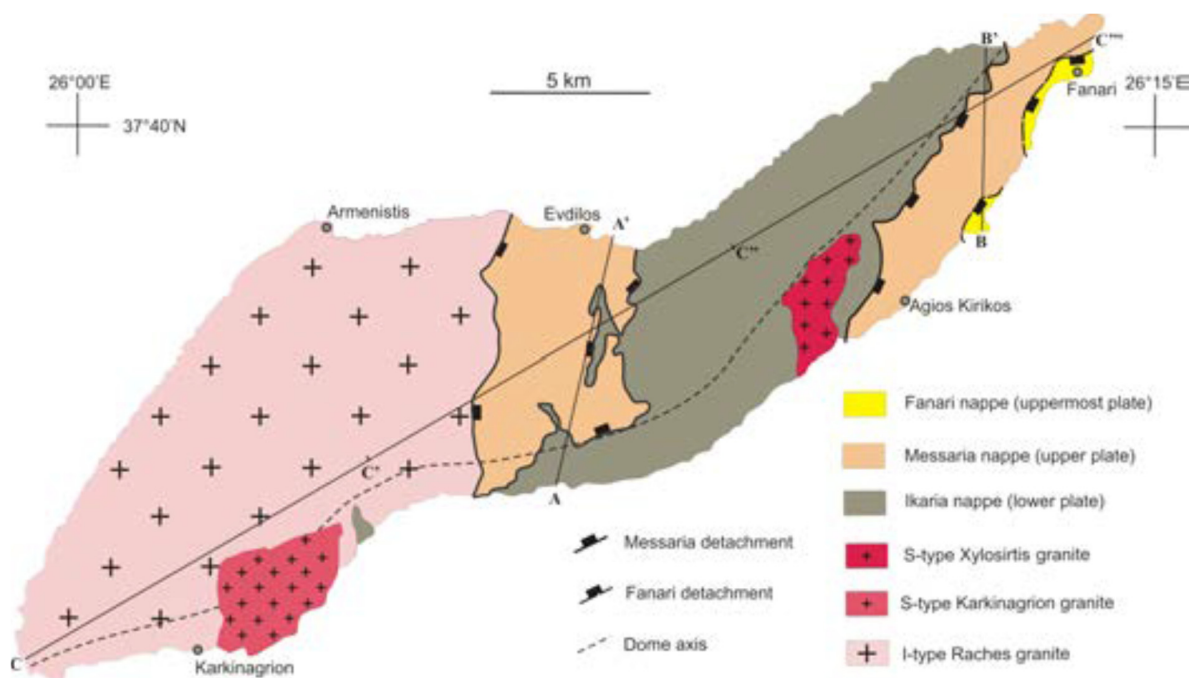


Fig. 1.6.9. Simplified geological map of Ikaria Island, depicting tectonic units, granitic intrusions and Messaria and Fanari extensional detachments (Ring, 2007).

According to Altherr et al. (1994), who applied K-Ar dating on amphiboles from amphibolites and diorites of the Kefala unit, this unit belongs to a wider LP/HT zone of Cretaceous age, not affected from the metamorphic and deformational events this region

underwent during Tertiary. Based on the mineral assemblages, Altherr et al. (1982), concluded low amphibolite-facies conditions for the Ikaria unit and greenschist-facies conditions for the Messaria unit. Hezel et al. (2011) and Steppan et al. (2002) focused on the enrichment of the Ikaria unit metamorphosed rocks in tourmaline and the consequent presence of boron-rich fluids, associated with the second Miocene metamorphic event. For the latter, a maximum metamorphic temperature ranging from $540\pm 24^{\circ}\text{C}$ to $567\pm 40^{\circ}\text{C}$ was estimated, based on the Grt-Bt geothermometer, and pressures of 7.8-9.9 kbar. Ktenas (1969), Ockenga (2000), Liati and Skarpeilis (2004), Iliopoulos and Katagas (2004) and Iliopoulos (2005) studied the Ikaria metabauxitic rocks and recorded a Jurassic age for the formation of bauxitic deposits, and upper greenschist to lower amphibolite-facies conditions for their metamorphism during the second metamorphic event.

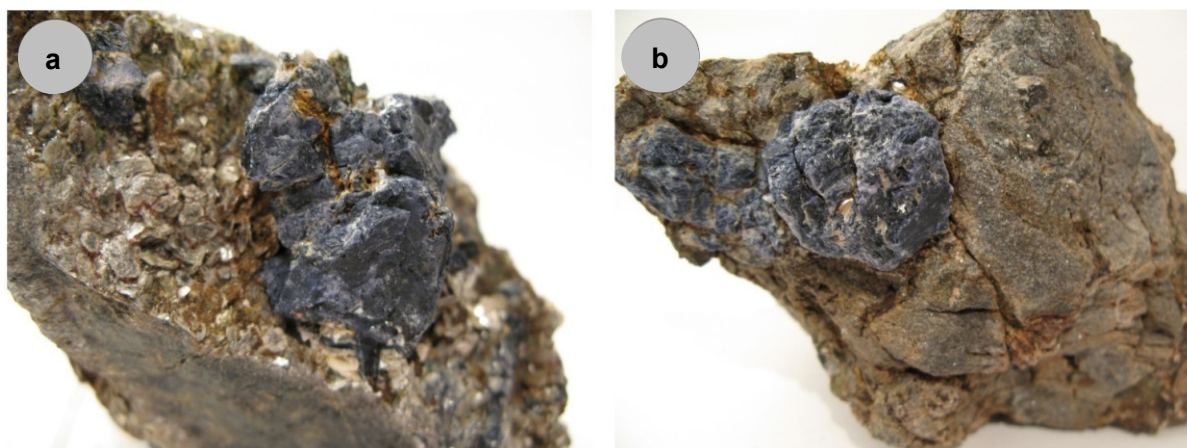
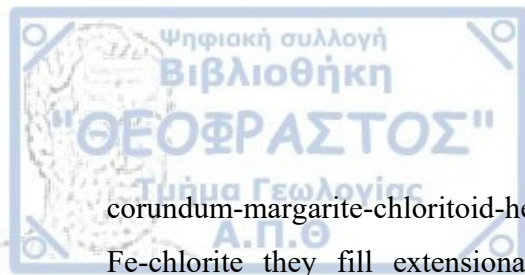


Fig.1.6.10. (a) Euhedral sapphire crystals intergrowing with margarite along Pounta metabauxitic cracks. (b) Euhedral sapphire crystals altering to diasporite in places (white spots) within Pounta metabauxites (Voudouris, 2010).

The corundum occurrence is detected in Atsides area on mountain Atheras (Ktenas, 1969; Iliopoulos, 2005). According to Iliopoulos (2005), in this area, the upper Pounta marble, composed of grey calcic overlain by white-yellow to sub-yellow dolomitic layers, lies conformably on top of the Plagia gneiss complex. The metabauxitic lenses that host sub-gem blue sapphires (Fig. 1.6.10) are located within the calcic marble layers and near the contact with the upper gneiss complex (Ktenas, 1969). Because of the high concentration of corundum, these rocks are characterized as emery deposits (Iliopoulos, 2005). In the sapphire-bearing area, four main blocks of metabauxites, of up to 1 m width, were detected (Voudouris et al., 2010). The sapphires occur in sizes that reach sizes up to 4-5 cm and are accompanied by the assemblage



corundum-margarite-chloritoid-hematite/ilmenite-rutile and together with coarse margarite and Fe-chlorite they fill extensional fissures and networks of veins within the metabauxites (Voudouris et al., 2010). The presence of diaspore replacing corundum indicates the continuation of the retrogression to low temperatures (Voudouris et al., 2010).



CHAPTER 2. MATERIAL AND METHODS

2.1. SAMPLE CATEGORIZATION

For the aims of this study, two pieces of 8 different samples were chosen, for a total of 15 studied pieces. They can be grouped in four different clusters depending on the place of origin:

- Naxos samples: NX1a, NX1b, NX2a, NX2b, NX4a, NX4b
- Ikaria samples: IK1a, IK1b
- Xanthi samples: GORa, GORb, GO5a, GO5b
- Drama samples: DR1, PARa, PARb

The first capital letters in the name of each sample derive from the place of its origin: NX stands for Naxos island, DR for Drama region, IK for Ikaria island, PAR for Paranesti deposit in Drama region and finally GO and GOR for “Gorgona” deposit in Xanthi region. The number is used only for the corundums that have more than one sample from the same region. The letter: “a” or “b” at the end of the name refers to the first and second patch of samples that were prepared and examined.

Naxos Samples: All Naxos samples originate from the plumasites penetrating the meta-peridotites. The crystals have dimensions with a range of 4 to 10 mm length, 1.5 to 8 mm width and 0.2 to 0.5 mm thickness and are found within a white plagioclase matrix. Some of them are connected in small assemblages. They present strong pleochroism; the color is ranging from dark blue to colorless. In some samples, whitish spots are obvious in a blue mass. They are transparent with smaller or bigger inner fractures.

Ikaria Samples: The corundum crystals are found like small assemblages within metabauxitic lenses hosted within Pounta’s Ca-rich marbles, together with margarite. They have



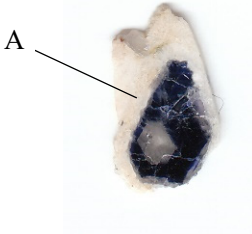

dimensions of 2 to 3 mm length, 3 to 7 mm width and 0.090 to 0.188 mm thickness. While transparent, their blue color is quite dark with few whitish spots appearing all over their surface.

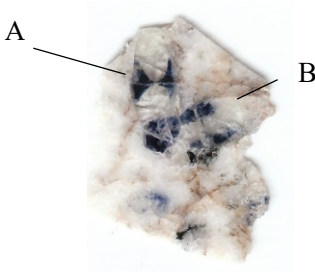


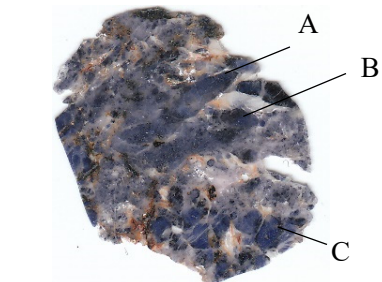
Xanthi Samples: The samples originate from the Gorgona-Stirigma area in Xanthi. They are found along micro-shear zones hosted in dolomitic marbles alternating with eclogitic amphibolites and gneisses. Their dimensions range between 7 and 11 mm length, 6 and 8 mm width and 0.155 and 0.553 mm thickness. In samples GO5a and GO5b corundum is colorless to light pink and is found with traces of the host marble. In samples GORa and GORb the corundum crystals are blue and occur together with the host marble and traces of an opaque mineral. The corundum crystals in all Xanthi's samples are quite transparent with very clear parting and fine cracks.




Drama samples: The corundum crystals are found within amphibole schist lenses in the Paranesti area. Each crystal is found as a single mineral and not in contact with others. They reach sizes up to 10 mm length, 9 mm width and approximately 0.5 mm thickness. The color can be characterized as light pink with some purplish spots. Their texture is quite transparent and the parting quite clear. Fine shallow cracks are also present.


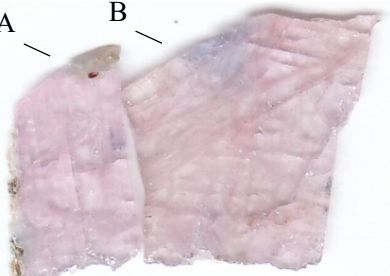

The table 2.1.1 below presents each sample's dimensions, color and transparency, macroscopic photo and analytical methods used. The dimensions (length x width) were calculated approximately with the use of a paper microscale under the spectrometer. Because some samples are single crystals while others consist of more than one corundum crystals, the dimensions presented in table 2.1.1 refer either to the whole sample or to the largest crystals. The thickness of each sample was measured with the use of a calliper. The macroscopic photos were taken with a CanoScan LIDE 90 scanner in a resolution of 300 dpi.

Table 2.1.1. Studied corundum samples.

Sample	Variety	Color	Host rock	Occurrence	Dimensions mm (length x width x thickness)	Photo	Analytical Methods
NX1a	Sapphire	blue to colorless, translucent to transparent	Plumasite	Single crystal	9.5x8x0.472		FTIR UV-Vis-NIR XRF Fluid inclusions
NX1b	Sapphire	blue to colorless, translucent to transparent	Plumasite	Single crystal	9x7x0.26		XRF Fluid inclusions
NX2a	Sapphire	blue, translucent to transparent	Plumasite	Crystal in host rock	A: 7.5x4x0.566		FTIR UV-Vis-NIR XRF Fluid inclusions
NX2b	Sapphire	blue to colorless, translucent to transparent	Plumasite	Crystal in host rock	A: 8x3x0.261 B: 4x4x0.261		XRF Fluid inclusions

NX4a	Sapphire	blue to colorless, translucent to transparent	Plumasite	Crystal in host rock	A: 10x4x0.503 B: 10x4x0.503		FTIR UV-Vis-NIR XRF
NX4b	Sapphire	blue to colorless, translucent to transparent	Plumasite	Crystal in host rock	A: 5x1.5x0.232		XRF Fluid inclusions
IK1a	Sapphire	blue to colorless, translucent to transparent	Meta-bauxite	Crystal in host rock	3x3x0.090 (sample cracked into two pieces after examination)		FTIR UV-Vis-NIR XRF Fluid inclusions
IK1b	Sapphire	blue to colorless, translucent to transparent	Meta-bauxite	Crystal in host rock	A: 2x7x0.188 B: 2x5x0.188 C: 2.5x4x0.188		XRF Fluid inclusions

GORa	Sapphire	blue, translucent to transparent	Marble	Crystal in host rock	11x8x0.435		FTIR UV-Vis-NIR XRF Fluid inclusions
GORb	Sapphire	blue, translucent to transparent	Marble	Crystal in host rock	7x6x0.155		XRF Fluid inclusions
GO5a	Sapphire	light pink to colorless, translucent to transparent	Marble	Crystal in host rock	10x7.5x0.553		FTIR UV-Vis-NIR XRF Fluid inclusions
GO5b	Sapphire	light pink to colorless, translucent to transparent	Marble	Single crystal	7x7x0.277		XRF Fluid inclusions

DR1a	Ruby	light pink, translucent to transparent	Amphibole schist	Single crystal	8x7x0.557		FTIR UV-Vis-NIR XRF Fluid inclusions
PARa	Ruby	light pink, translucent to transparent	Amphibole schist	Single crystal	A:8x4x0.45 B:10x8x0.45		FTIR UV-Vis-NIR XRF Fluid inclusions
PARb	Ruby	light pink, translucent to transparent	Amphibole schist	Single crystal	8x9x0.432 (sample cracked into two pieces after examination)		XRF Fluid inclusions

2.2. SAMPLES PREPARATION

The method followed for the preparation of samples was the same for preparing double polished thin sections suitable for examination of fluid inclusions. While following the process the aim was to create two surfaces parallel to each other with no specific attention to being parallel to the samples' parting. Though the common case for this process is to prepare sections with specific thickness, in the current process the criteria for the thickness of the section was for the sample to be transparent. In order to achieve these features the lapping and polishing process was conducted first for the one side of the section and afterwards for the other.

In the beginning of the process the samples were cut and ground using the diamond cutting wheel of Discoplan-TS of Struers. Attempts were made to use an approximate orientation that contained the c-axis, but this was only partly accomplished. They were then lapped using the diamond cup wheel of the same machine with a 300-grit silicon carbide powder, following the lapping on hand using 400, 600, 800, 1000 and 1200-grit silicon carbide powder. The next step was polishing, using a moving lap wheel mounted with a lap cloth along with a diamond paste of 3, 1 and 0.25 μ m. After finishing the one side of the section, the samples were attached to glass slides, with the use of the Lakeslide Thermoplastic Quartz Cement, the polished side being in contact to the glass. The slides were placed to the diamond cutting wheel again to achieve a ground surface parallel to the first. The thickness of each sample was determined by its transparency: the grinding would stop when the sample was transparent enough for the light to pass through. The same lapping and polishing steps were followed to complete the sections. Finally, the samples were detached from the glassy slides and cleaned with ethanol, in which they stayed for 5 days.

2.3 ANALYTICAL TECHNIQUES

Petrology, FTIR spectroscopy, UV-Vis-NIR spectroscopy, EDXRF analysis and fluid inclusions are the analytical techniques used for the identification of corundum in the framework of this specific paper.

2.3.1. Petrology

Petrographic and mineralogical observations were made using a Carl Zeiss Axioscop 40 microscope at a magnification range of 5x, 10x and 20x. The observation of thin-sections was performed under parallel nicols (uncross polarized light) and crossed nicols (cross polarized light). Figure 2.3.1.1 illustrates an overall view of a Carl Zeiss Axioscop 40 microscope.

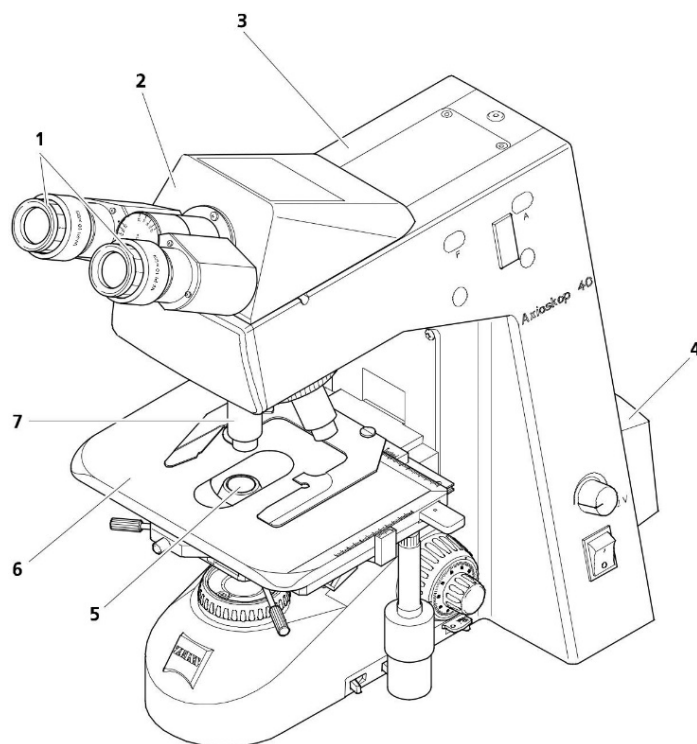


Fig. 2.3.1.1. The Carl Zeiss Axioscop 40 microscope: 1) eyepieces, 2) binocular tube, 3) stand, 4) transmitted-light illuminator, 5) condenser 0.9/1.25 H, 6) mechanical stage, 7) objective (Microscopy News).

2.3.2. IR Spectroscopy with Fourier Transform (FTIR)

The interaction of light with matter is defined as spectroscopy. Infrared spectroscopy is the spectroscopy that has to do with the infrared region of the electromagnetic spectrum. The IR spectral region covers radiation with wavenumbers from 14000 to 10 cm^{-1} (750 to 1000000 nm approximately, near-IR radiation covering the region between 750 to 3000 nm, mid-IR 3000 to 50000 nm and far-IR 50000 to 1000000 nm). Most analytical applications are conducted in the mid-IR region.

IR radiation does not have enough energy to affect the electrons within the atom. However, it has an impact on the energy transitions having to do with translation, rotation and vibration. Absorption of IR radiation in this region of the electromagnetic spectrum, causes changes in the vibrational energy of molecules. Because every structure is unique and dependent of its molecule's movements, this absorption can be characterized as a resonant frequency, in the sense that the frequency of the absorbed radiation matches the transition energy of the bond or group that vibrates. This is why IR is such an important tool for the characterization of a compound.

Only the absorptions that are active in the IR region - absorptions which are produced by a first-order or fundamental vibration and they are the strongest energy absorptions - will be seen as an absorption band in the IR spectrum. In order for an IR absorption to be active, the dipole moment of the molecule must be changed by the vibration. This is the primary selection rule for a vibration to be seen in the spectrum. In a heteronuclear molecule, a vibrating dipole moment creates a dipolar electric field that in turn absorbs a discrete unit of energy unique to that transition. These vibrations are seen in the IR spectrum, in opposition to the vibrations in a homonuclear diatomic molecule, which do not affect the dipole moment.

A functional group within a molecule is responsible for IR absorptions at or near the same frequency. Hooke's law - a mathematical equation for the vibrational frequency of a two-body system - is used in order to predict the absorption band position for simple molecules. Each particular functional group has vibrational frequencies which are characteristic of that group. When IR radiation hits the molecules of the sample, we have two types of interaction - absorption and transmission. These two interactions are related through the equation:

$$A = \log 1/T$$

where A = Absorbance and T = Transmittance (%T/100), for a given wavelength or frequency of IR (Derrick et. al, 1999).

In order to measure infrared spectra a Fourier transform spectrometer is used, that is a Michelson interferometer with one mirror movable (Fig. 2.3.1.3). Light is emitted from a broadband light source, which contains the full spectrum of wavelengths of IR, then divided by a beam splitter into two beams. The one beam is reflected to the fixed mirror while the other is transmitted to the movable mirror. This motion of the movable mirror at a constant velocity over a fixed distance, creates a change in path difference. During this motion, each wavelength of the collected radiation is modulated at a unique frequency that is a function of the wavelength of the radiation and the velocity of the moving mirror. The two beams go back to the beam splitter

where they interfere. Each beam has an intensity dependent on the difference of path lengths in the two arms of the interferometer. When the fixed and movable mirrors have the same distance from the beam splitter, the beams are in phase and constructive interference happens. In this case, all the light from the source reaches the detector. If the movable mirror is displaced by $\lambda/4$, then the total (roundtrip) retardation or path difference of the two beams is $\lambda/2$. On recombination at the beamsplitter, the beams are 180° out of phase, thus interfering destructively. A further movement of the mirror by another $\lambda/4$ creates a path difference of λ and constructive interference happens again. This ongoing process results in a plot or a graph presenting this variation in the intensity of the beams, called interferogram.

The Fourier Transform provides the decoding of the interferometer and presents the spectrum of the target radiation (Block Engineering).

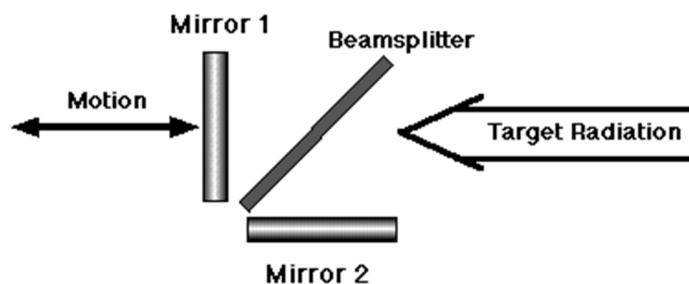


Fig. 2.3.2.1. The Michelson interferometer (Block Engineering).

FTIR on corundum

FTIR has been one of the most important analytical methods for geologists as well as gemologists. It provides the possibility of successful identification of a gem, the identification of its mineral inclusions thus helping the establishment of its geology, the differentiation between natural and synthetic gemstones and the examination of its quality by recognizing the different treatments.

The region that is of the most interest for gemologists is the region between 400 and 6000 cm^{-1} (Karampelas, 2008), as this is the region where the bands related with hydroxyl vibrations are typically located (Smith, 1995). Being part of a corundum lattice or part of a hydrous mineral inclusion, OH plays a significant role in the IR spectra of corundum crystals. The observation of OH bands in the infrared spectra of corundum can assist in the configuration of its structure and the identification of its origin. Several papers report the presence of OH in synthetic corundum - either as a component of inclusions or as a trace component of corundum itself (Eigenmann and

Günthard, 1971, 1972; Eigenmann et al., 1972; Volynets et al., 1969, 1972; Moon and Philips, 1991, 1994; Beran, 1991; Belt, 1967; Peretti and Smith 1993), and a large number of studies report the presence of OH in natural corundum (Fredericksonm, 1954; Ferguson and Fielding, 1971; Farmer, 1974; Smith, 1995; Häger and Greiff, 1994; Häger, 1996; Smith et al., 1995; Emmett et al., 2003; Beran and Rossman, 2006; Garnier et al., 2005, 2006; Schwarz et al., 2008; Cartier, 2009).

The presence of OH absorption bands in the spectra of natural rubies can be related either to inclusions and naturally included mineral contaminants or to the structurally bonded OH in corundum. The most commonly observed FTIR mineral contaminant spectra in corundum are those for boehmite, diaspore, gibbsite, kaolinite, goethite, mica, apatite and calcite. The observation of the sequence of peaks appearing in the spectra leads to the identification of the mineral inclusion. Emmett et al. (2017) summarize the peaks of the most common mineral inclusions in rubies and sapphires (in cm^{-1}):

- Diaspore: 2040, 2140, 2900, 3020
- Boehmite: 1975 or 1985, 2106, 3089, 3296 or 3313
- Goethite: 3145, 3372
- Kaolinite: 3621, 3685 or 3699
- Calcite: 1790, 2505, 2575 or 2600, 2850, 2920
- Gibbsite: 3381, 3442, 3523, 3622

Structurally bonded (with e.g., titanium, vanadium, magnesium, or iron) OH in corundum is commonly revealed through a series of peaks variously known:

- The 3309 series (3365, 3309, 3295, 3232, 3186)
- The 3160 series (3355, 3242, 3160, 3075)
- The 4230 series (4230, 2980–3200)
- The 3394 series (3394, 3378, 3367)
- The 3064 series (3191, 3064, 2626, and 2490) - also known as the Punsiri series

The number of absorption peaks is dependent on the concentration of OH bonding. The maximum absorptions of OH bands are observed when the vibration of the polarized radiation is vertical to the c-axis (Beran and Rossman, 2006). Beran (1991) created a model where a OH dipole with orientation vertical to the c-axis is coordinated with two Al atoms forming face-sharing $\text{Al}_2(\text{OH})\text{O}_8$ -double octahedra. Prerequisite for this model is the existence of Al vacancies

in corundum lattice. These vacancies are the reason for the splitting of the triplet band with maxima at 3310, 3230 and 3185 cm^{-1} (Beran and Rossman, 2006).

The diagram in figure 2.3.2.2 presents the OH absorption bands of non-heat-treated rubies from Mong Hsu. The OH band is the result of the presence of diasporite (αAlOOH). Mong Hsu rubies present the typical corundum absorption peaks associated with Al-O stretch frequencies and lattice absorptions in the region between 300 and 1000 cm^{-1} , as well as absorption bands in the region between 1900 and 4000 cm^{-1} associated with OH bending and stretching frequencies. (Smith, 1995).

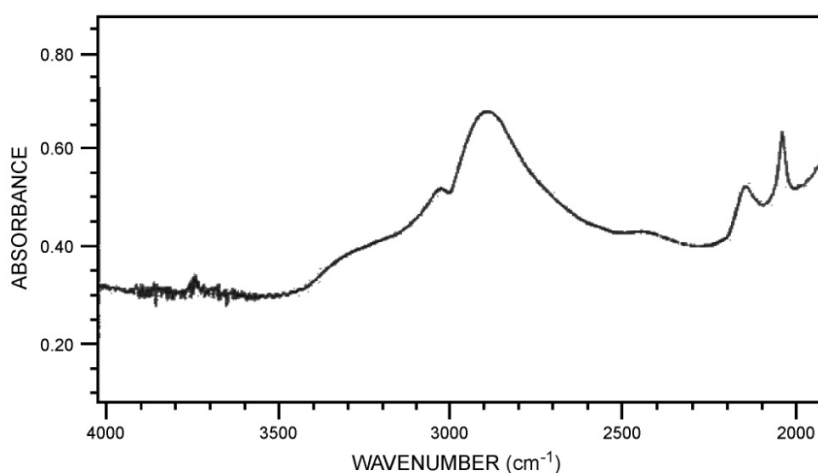


Fig. 2.3.2.2. IR spectra of natural ruby samples from Mong Hsu, Myanmar. The absorption peaks of OH in the region between 1900 and 3400 cm^{-1} are assigned to the presence of diasporite (αAlOOH) (modified after Smith, 1995).

The diagram of figure 2.3.2.3 presents the peaks observed within the OH fundamental region in an unpolarized spectra taken through turbid crystal parts. Spectrum (a) is representative of goethite $\text{FeO}(\text{OH})$ mineral inclusions in yellow corundums from Sri Lanka. Spectrum (b) is typical of inclusions of the chlorite group in sapphires from Montana and Tanzania. Spectrum (c) is the most usual spectra taken through turbid parts of corundum and is typical of kaolinite $\text{Al}_2\text{Si}_2\text{O}_5(\text{OH})_4$ group phases. Spectrum (d) is the result of the presence of diasporite $\alpha\text{AlO}(\text{OH})$ in the Tanzanian rubies (the peak is standardized at around 2900 cm^{-1}) (Beran and Rossman, 2006).

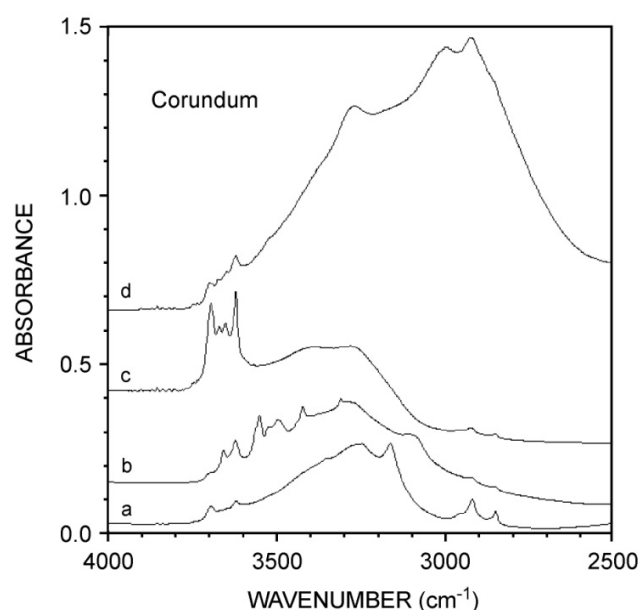


Fig. 2.3.2.3. Unpolarized spectra in the OH stretching vibrational range of corundum, taken through turbid crystal parts: (a) OH absorption features of goethite (Sri Lanka), (b) chlorite group minerals (Umba River Valley, Tanzania), (c) kaolinite group minerals (Dry Cottonwood Gulch, Silver Bow Co., Montana) and (d) diaspore (Tanzania) (modified after Beran and Rossman, 2006).

Figure 2.3.2.4 presents the structural OH absorption bands, which are associated with metal ions (mainly Ti, V or Fe) bonds. These bands are observed both in natural and synthetic corundums. In natural corundums, they are present more often in non-heat-treated blue sapphires from basaltic sources rather than non-heat-treated rubies and sapphires from other types of sources (i.e. metamorphic). In synthetic corundums, they are observed more often in Verneuil (flame-fusion)-grown or hydrothermally-grown corundums rather than corundums grown by other methods. Figure 2.3.2.3 shows that natural ruby from Myanmar (B) has no peak at all, in opposition to natural blue sapphire from Thailand (D) which presents a strong peak at approximately 3310 cm^{-1} . Hydrothermally-grown synthetic ruby (E) has the strongest peak, while flux-grown (A) and flame-fusion (C) synthetic rubies present no peak and a very weak one respectively (Smith, 1995).

The appearance of the 3309 or 3310 OH related absorption bands series is also an indicator of heat treatment. Figure 2.3.2.5 presents the difference in the spectra of a synthetic, a heat-treated and a non-heat-treated natural ruby. Though both the synthetic and the heat-treated samples present the 3309 OH series, in the case of the synthetic ruby the main peak is situated at 3230 cm^{-1} , while in the case of the heat-treated at 3310 cm^{-1} .

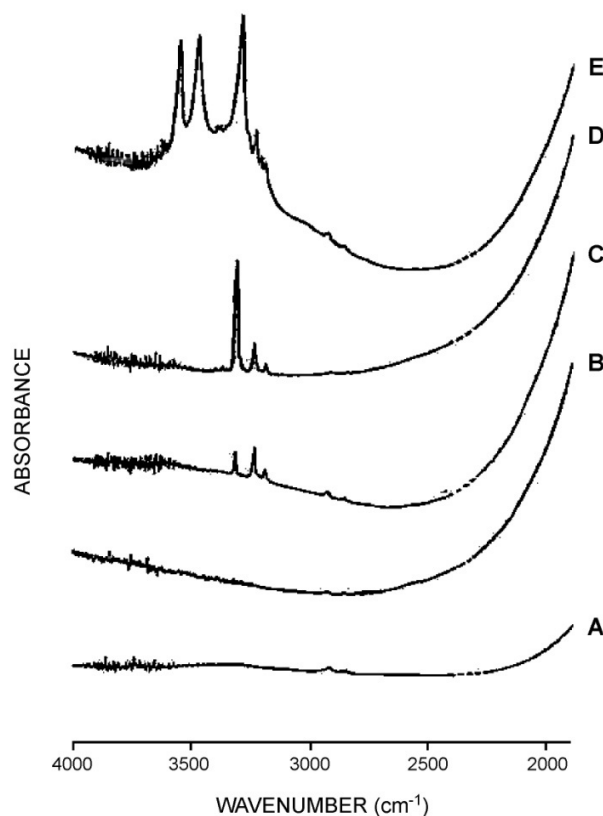


Fig. 2.3.2.4. OH absorption peaks of (A) flux-grown synthetic ruby, (B) natural ruby from the Mogok stone-tract, Burma (Myanmar), (C) flame-fusion synthetic ruby, (D) natural basaltic blue sapphire from Thailand, (E) hydrothermally-grown synthetic ruby (modified after Smith, 1995).

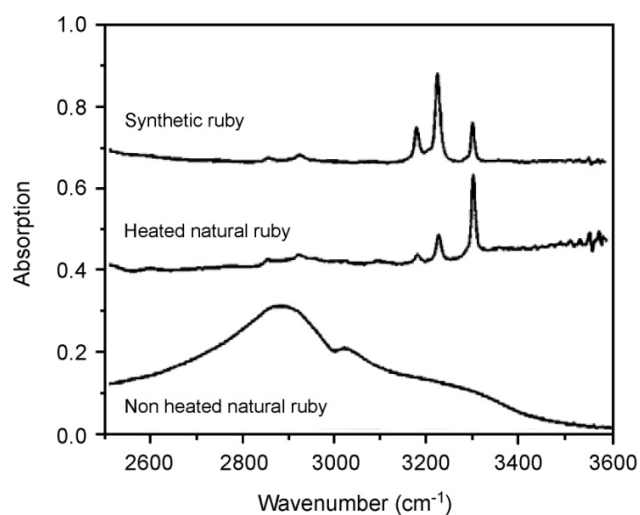


Fig. 2.3.2.5. OH absorption peaks of a synthetic Verneuil ruby (upper spectrum), a heat-treated Mong Hsu ruby (middle spectrum) and a non-heat-treated natural Mong Hsu ruby (bottom spectrum) (modified after Karampelas and Kiefert, 2012).

A dashed line in the region between 3500 and 4000 cm^{-1} represents either the CO_2 from the atmosphere (Smith, 1995) or the water from the instrument. A doublet at approximately 2400 cm^{-1} (2361 to 2342 cm^{-1}) is also assigned to atmospheric CO_2 or CO_2 gas in negative crystals (Phan, 2015). The difference between the two is spotted in the bandwidth: atmospheric CO_2 is presented with narrow peaks while inclusion-related CO_2 with broader and more clear peaks (Fig. 2.3.2.6). For a more thorough discrimination, the same spectra can be taken with higher resolution and if there is a difference in the width of the peaks (greater than the one in lower resolution), then the interpretation is in favor of atmospheric CO_2 . The region between 1500 and 3000 cm^{-1} is where the organic group vibrations are found (Skoog et. al, 2000; Brown and Poon, 2005; Karampelas, pers. comm., 2012). The finger grease from the manipulation of the sample is usually detected between 2850 and 2960 cm^{-1} .

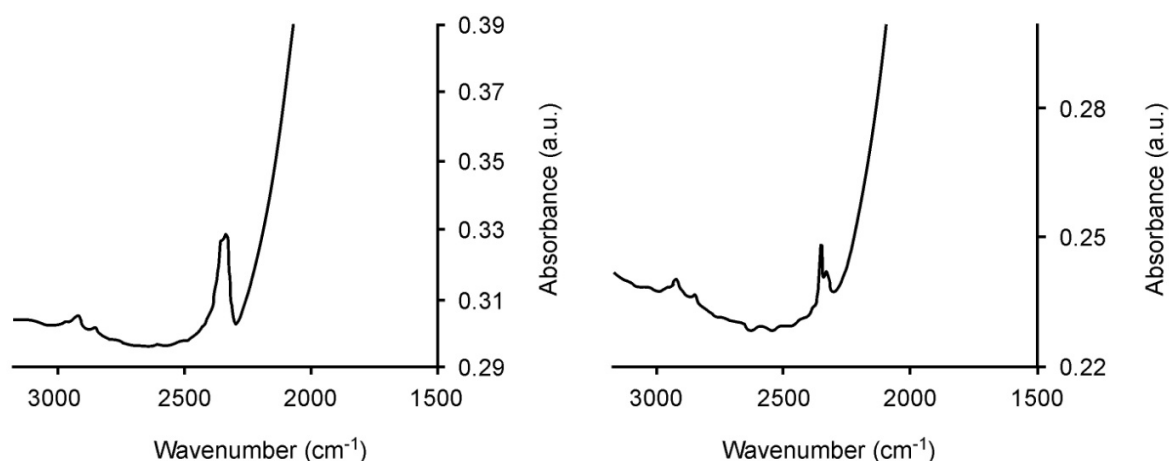


Fig. 2.3.2.6. Absorption spectra showing the difference between a CO_2 as an inclusion related band (left) and an atmospheric CO_2 band (right) (modified after Elmaleh, 2014).

All the organic compounds present strong absorptions in the infrared region so the thorough cleaning of the samples after their preparation and before the initiation of the measurements, as well as the use of gloves and tweezers for their carrying are deemed necessary.

Measurements were conducted in the GGTL of Lichtenstein. Unpolarized infrared spectra of the background and the samples were recorded at room temperature in transmission by using a Perkin Elmer Spectrum 100S FTIR spectrometer equipped with a thermoelectrically cooled DTGS detector. The spectra were taken in the range of 400-8500 cm^{-1} . Each measurement was performed within 64 scans and with a spectral resolution of 4 cm^{-1} . The background was

measured before every session. The spectrometer is attached with a hemispheric mirror which acted both as a beam condenser to illuminate the sample and as a collector for the diffused light. An air-cooled source is included for delivering optimum power to the sample.

2.3.3. UV-Vis-NIR spectroscopy

Ultraviolet-visible-near-infrared spectroscopy refers to the absorption, or reflectance spectroscopy for opaque gems, that has to do with the ultraviolet-visible-near-infrared region of the electromagnetic spectrum. More specifically, this spectroscopy covers the region with wavelengths from 250 to 380 nm (ultraviolet), 380 to 750 nm (visible) and 750 to 3000 nm (near-infrared). UV-Vis-NIR spectroscopy facilitates the measuring of different percentages of light reflected, transmitted or absorbed by the sample, whilst taking into account the various phenomena capable of producing misleading measurements (diffusion, refraction, polarization).

In the region between 200 and 3000 nm, the irradiation of energy on the molecules promotes changes in their electronic nature, i.e. changes between ground state and excited states of electrons within the system, as it forces bonding and non-bonding electrons to higher, less stable antibonding (or excited) orbitals. An optical spectrometer records the loss of energy of the molecule caused due to rotation and vibrational relaxation by calculating the wavelengths at which absorption occurs, together with the degree of absorption at each wavelength. The resulting spectrum is presented as a graph of absorbance (A) versus wavelength.

A typical spectrometer is shown in figure 2.3.3.1. A beam of light from a visible and/or UV light source (red) is separated into its component wavelengths by a prism or diffraction grating. Each monochromatic (single wavelength) beam in turn is split into two equal intensity beams by a half-mirrored device. The sample beam (magenta color), passes through a small transparent container (cuvette) containing a solution of the analysed compound in a transparent solvent. The other beam, the reference (blue), passes through an identical cuvette containing only the solvent. The intensities of these light beams are then measured by electronic detectors and compared. The intensity of the reference beam, which should have suffered little or no light absorption, is defined as I_0 . The intensity of the sample beam is defined as I . Over a short period of time, the spectrometer automatically scans all the component wavelengths in the manner described (MSU Chemistry).

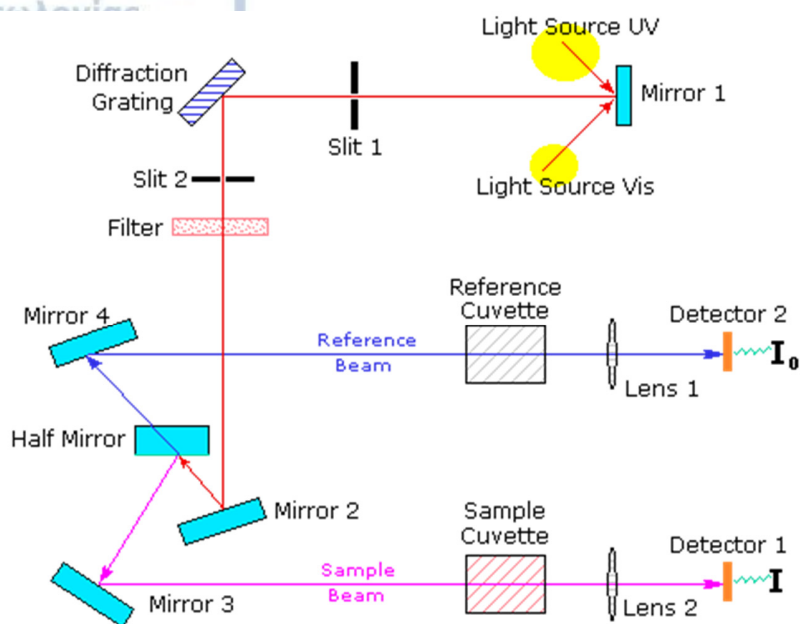


Fig. 2.3.3.1. Schematic presentation of UV-Vis-NIR spectrometer (MSU Chemistry).

In the UV-VIS range materials can be analyzed in transmission (transparent/translucent samples) or in reflection (opaque sample). The data can be presented as transmittance, absorbance or reflectance.

In the case of transparent/translucent samples, if no light is absorbed from the sample, then $I = I_0$. If any portion of light is absorbed, then $I < I_0$ and this difference is plotted on a graph versus wavelength. Absorption is presented as:

- Transmittance, where $T = I/I_0$ or $T\% = 100 \cdot T = 100 \cdot I/I_0$, or
- Absorbance, where $A = \log I_0/I$ or $A = -\log(T)$

For no absorption, $T=1$ and $A=0$. Absorbance is displayed on the vertical axis with a range from 0 (100% transmittance) to 2 (1% transmittance).

An important factor that must be taken into account when measuring transmittance, is that the transmitted beam may deviate in relation to the incident beam. This can happen due to refraction or uneven surface of the sample. In case of considerable deviation of the transmitted beam, the likelihood of it not been fully picked up by the detectors is increased, thus deteriorating the quality and quantity of the signal. Another reason of deviation is the diffusion of the beam in all directions by the sample. In this case, in order to measure the total transmittance - that is the direct transmittance plus the diffuse transmittance (including the

deviation of the beam) - the use of an integrating sphere is required. Otherwise, the measurements of direct and diffuse transmittance can take place separately.

In the case of opaque samples, the analysis in reflection is more suitable, since light cannot penetrate the surface of these materials. Different phenomena take place when a sample is analyzed in reflection, such as specular reflection, when the incident light is reflected symmetrically with respect to the normal line (typical for smooth surfaces), and diffuse reflection, when incident light is scattered in different directions (typical for rough surfaces). Most samples produce a combination of specular and diffuse reflectance. With the use of proper equipment, it is possible to measure either the total reflectance or the specular and the diffuse reflectance separately. Reflectance is presented as

- $R = I_R/I'$, where I_R is the reflected light and I' is the incident light reflected by an ideal reflector.

Diffuse reflectance is used for near-infrared measurements of solid samples. The instruments can be easily configured for such measurements, and all the requirements for optimum spectra include small sample size (mean particle size is preferably less than 50 μm in diameter) and an infinite path length (generally 5-10 mm).

UV-Vis-NIR spectroscopy on corundum

UV-VIS spectroscopy has been one of the first “advanced methods” applied on gems and minerals. When the absorption of light irradiation happens in the visible region of the electromagnetic spectrum, that is between 380 to 750 nm (approximately 25000-13400 cm^{-1}), then this phenomenon is responsible for each material’s color (Fritsch and Rossman, 1987).

As cited in chapter 1, corundum appears colored due to replacement of Al^{3+} from traces of transition metals (Cr, Fe, Ti, V and Mn) in the corundum structure. Depending on the trace elements taking the place of Al^{3+} , different peaks are depicted in the UV-Vis-NIR absorption spectra of each sample. A brief table with the identified absorption peaks and the corresponding elements according to literature is given below (Table 2.3.3.1).

Emmett et al. (2017) proposed the absolute absorption cross section spectra for all chromophores that color corundum. According to these spectra the main absorption peaks for each chromophore are: a) for Cr^{3+} two main peaks at 560 and 400 nm, a weak peak at 694.3 nm and two weak peaks at 470 nm, b) for Fe^{2+} - Ti^{4+} a broad band at 580 nm, for V^{3+} two peaks at 400

and between 570 and 580 nm, d) for Fe^{3+} - Fe^{3+} two narrow peaks at 377 and 450 nm and a weak band at 540 nm, e) for Fe^{3+} a narrow peak at 388 nm (additional peaks at 700, 1050 and 1085 nm are also recorded at high Fe concentrations) and f) for Fe^{2+} - Fe^{3+} a main peak at 880 nm. The 377, 388 and 450 peaks are visible in the spectra of most corundums with a Fe concentration of 150 ppm and higher, while the 880 peak is mostly observed in basaltic sapphires of deep blue color.

Table 2.3.3.1. UV-Vis-NIR absorption peaks due to trace elements.

Color	Chemistry	Absorption bands (nm) according to literature	Absorption bands (nm) according to Emmett et. al (2017)
Red	Cr^{3+}	405, 560, 694 ¹	400, 560, 694.3
		468, 475-477 ²	470
Blue	Fe^{2+} - Ti^{4+}	570, 700 ³	580
	Fe^{2+} - Fe^{3+}	880	880
Yellow	Fe^{3+}	377, 388, 450 ⁴	388, (700, 1050, 1085)
	Fe^{3+} - Fe^{3+}	330, 420, 540 ⁵	377, 450, 540
	Color centers	465 ⁶	-
Grayish blue to green	V^{3+}	400, 570-780 ⁷	400, 570-580

- Schwarz et al. (2008)
- Duroc-Danner (2002)
- Schmetzer (1987), Fritsch and Rossman (1987, 1988), Ferguson and Fielding (1971, 1972), Moon and Phillips (1991, 1994), Smith et al. (1995), Schwarz et al. (2000)
- Ferguson and Fielding (1971, 1972), Smith et al. (1995), Schwarz et al. (2000), Hager (2001), Schwarz et al. (2008)
- Ferguson and Fielding (1971, 1972)
- Schmetzer et al. (1982, 1983), Emmett and Douthit (1993), Hager (1993)
- Emmett et al. (2017)

The observation of the UV-Vis-NIR spectra of a corundum can give valuable information about the origin of the crystal. A first discrimination can be made between magmatic/basaltic and metamorphic deposits. The corundum is basalt related when it presents an iron related absorption with a maximum above 700 nm (from the red to the near infrared region) (Fig. 2.3.3.2).

Another discrimination can be made between magmatic/basaltic and metasomatic deposits. If the spectra of the corundum presents a shoulder at around 300 nm, the sample is of metamorphic origin ("Burma-type"), while if no shoulder appears at this wavelength then it is metasomatic related ("Kashmir-type") (Fig. 2.3.3.3). Burma-type sapphires usually present a "cut-off" in their spectra at/below 320 nm, while for the Kashmir-type sapphires the "cut-off" is located above 340 nm.

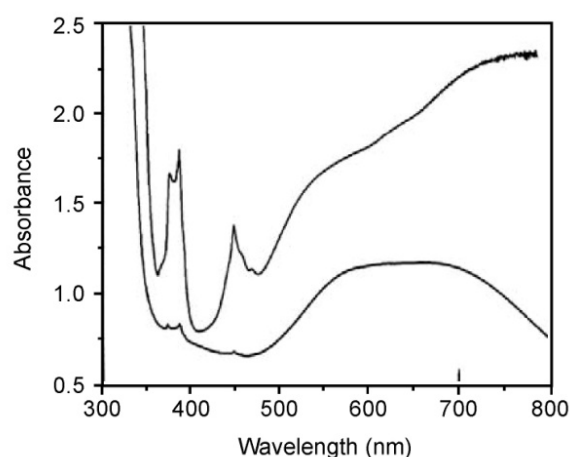


Fig. 2.3.3.2. UV-Vis-NIR absorption spectra of two faceted natural blue sapphires from basaltic related (upper spectrum) and metamorphic (bottom spectrum) environment (modified after Karampelas and Kiefert, 2012).

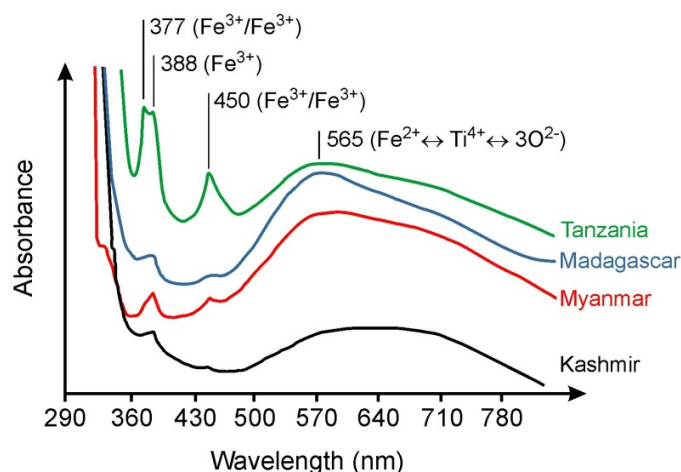


Fig. 2.3.3.3. UV-Vis-NIR absorption spectra of four sapphires from different deposits. The shoulder at 300 nm of the Myanmar sapphire is visible, indicating the metasomatic origin of the sapphire. The Kashmir sapphire presents no shoulder (modified after Giuliani et al., 2014).

Figure 2.3.3.4 presents three different spectra of metamorphic, metamorphic-magmatic (metasomatic) and magmatic related sapphires. The metamorphic origin is characterized by an intervalence charge transfer between iron and titanium ($\text{Fe}^{2+}\text{-Ti}^{4+}$) with weaker Fe^{3+} absorption. The metamorphic-magmatic (metasomatic) type is characterized by a strong absorption related to Fe^{3+} , in addition to the intervalence charge transfer between iron and titanium ($\text{Fe}^{2+}\text{-Ti}^{4+}$). Both the metamorphic and the metasomatic spectra present an absence of the $\text{Fe}^{2+}/\text{Fe}^{3+}$ intervalence charge transfer absorption. On the contrary, a strong $\text{Fe}^{2+}/\text{Fe}^{3+}$ intervalence charge transfer absorption indicates a magmatic origin (Smith, 2010).

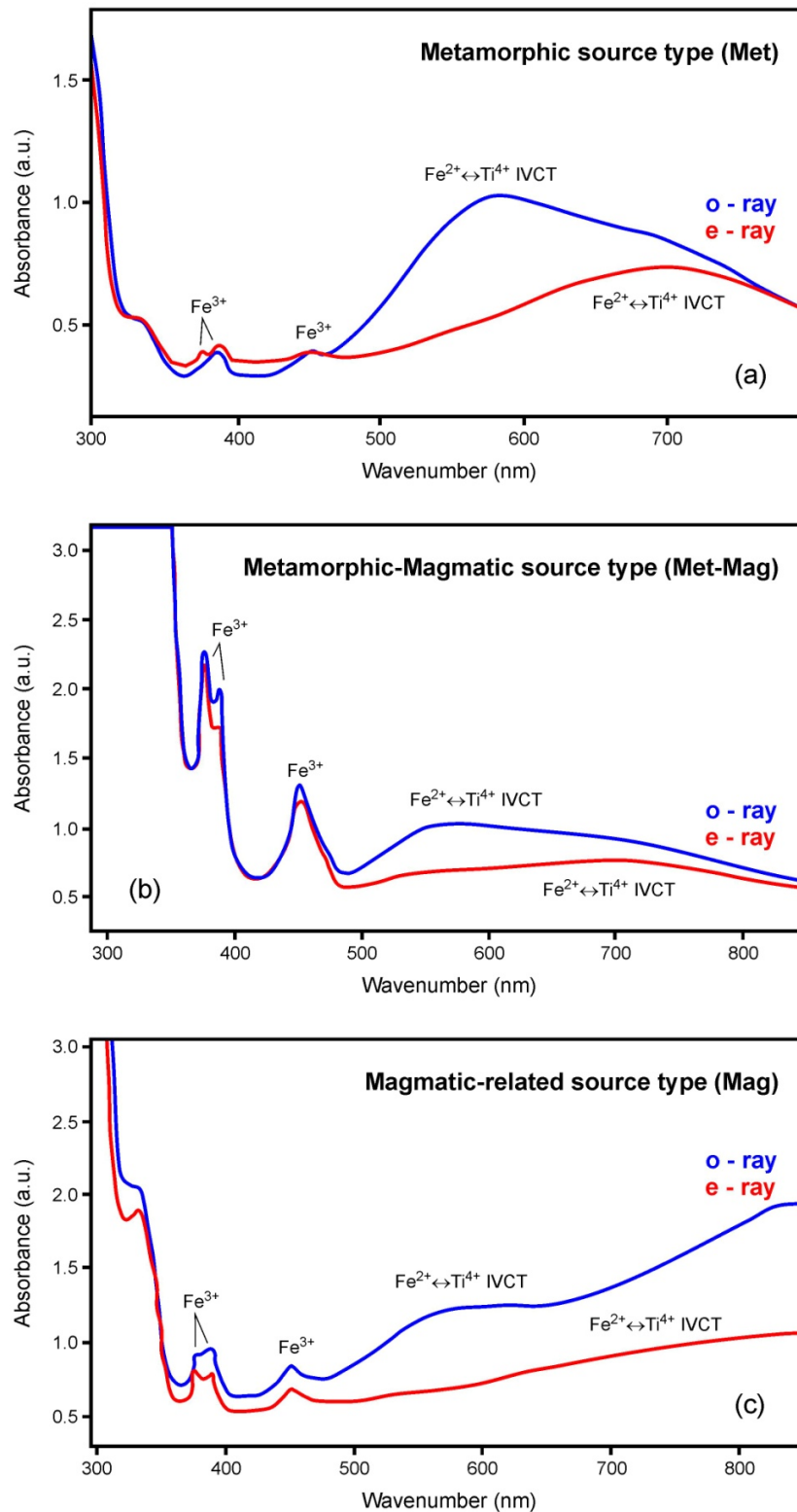


Fig. 2.3.3.4. UV-Vis-NIR absorption spectra of three different geological environments: a) metamorphic, b) metamorphic-magmatic (metasomatic) and c) magmatic related source type sapphires (modified after Smith, 2010).

UV-Vis-NIR measurements were conducted in DANAT (Manama, Bahrain). A Cary 5000 Ultra-Violet-Visible-Near Infrared (UV-Vis-NIR) spectrometer recorded the absorption spectra in the region between 250 and 880 nm in transmission mode. The data sampling interval (DI) and spectral bandwidth (SBW) of each measurement were 0.7 nm; the scan rate was 210 nm/min.

2.3.4. Energy Dispersive X-ray Fluorescence (EDXRF)

Energy Dispersive X-ray Fluorescence is a type of X-ray Fluorescence technique used for elemental analysis applications. The emission of secondary or fluorescent X-rays, when a sample is bombarded with high-energy photons in the X-ray region, is called X-ray fluorescence.

When the atom is exposed to radiation with an energy greater than its ionization energy (i.e. with X-rays), then one or more electrons from the inner orbitals of the atom are expelled (Fig. 2.3.4.1). The emission of an electron renders the electronic structure of the atom unstable, since it is going to a higher energy state. Electrons from higher orbitals fall down towards the lower in order to fill the “gap”. The energy released during the “fall” is in the form of a photon and equals to the energy difference between the two orbitals. The transition takes place between adjacent orbits/levels and the emitted photons carry information about their spacing, according to Planck’s law $\Delta E = h \cdot \nu$, in the range, again, of X-rays (Sackler, 2003).

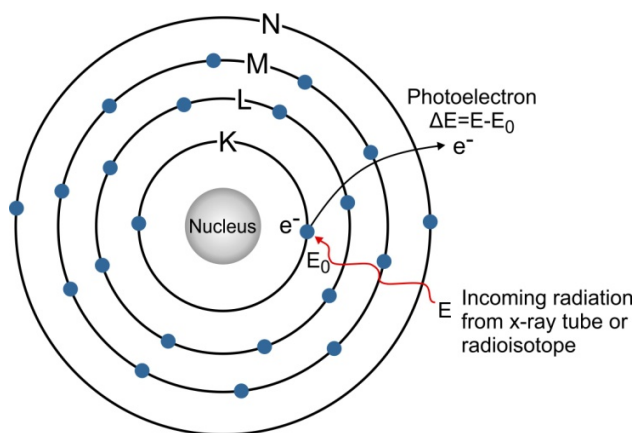


Fig. 2.3.4.1. Expulsion of a photoelectron by ionization of the atom when absorbing incoming energy and the creation of a gap in the inner line.

The set of ΔE are typical for each atomic species, and the names of the line record the shell where the vacancy was produced and the shell of origin of the replacing electron: the capital

letter indicates the shell in which the vacancy was created (K, L, M...), the Greek letter α means that the electron which filled the vacancy originated in the adjacent shell, while β denotes a two-shell jump, as in (Fig. 2.3.4.2). The separation among the X rays produced in the process, that is the X ray fluorescence spectrum of a substance, can be performed on the basis of the energy (EDXRF) or of the wavelength (WDXRF).

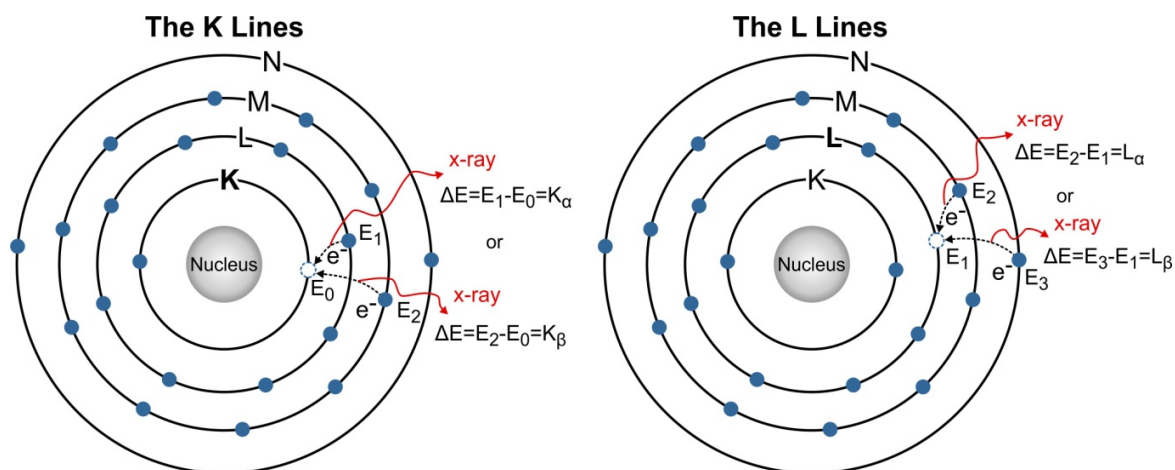


Fig. 2.3.4.2. The K and L lines fluorescence emission.

In EDXRF spectrometers, all of the elements in the sample are excited simultaneously, and an energy dispersive detector in combination with a multi-channel analyser is used to simultaneously collect the fluorescence radiation emitted from the sample and then separate the different energies of the characteristic radiation from each of the different sample elements.

This technique cannot discriminate between different charge ions, since the information comes from the internal shells not involved in bond formation. For instance, when it comes to chemical elements such as iron, the site occupancy cannot be resolved with this technique. In addition, oxygen and hydroxyl are not taken into account, since light atoms cannot be detected. These factors render the determination of the chemical formula of minerals difficult, especially for minerals such as amphiboles and micas, including both OH and chemical elements with various charge ions.

With EDXRF analysis most elements with an atomic number higher than Na ($Z=11$), as well as trace elements in the order of hundred ppm, can be detected. Elements lighter than Na cannot be detected in most cases. According to the response of each element, which is dependent on the element's atomic number (Z), X ray absorption coefficient (A) and secondary fluorescence emission (F), the instrument is calibrated for a reliable esteem of its amount. The percentages of

the elements are expressed as oxides with the use of ZAF algorithm. The chemical formula is calculated by these oxides in terms of atoms per formula unit (Coccato, 2011).

During the XRF measurement, it is important to pay attention to artefacts such as diffraction peaks. In order to avoid these artefacts, different measurements of the same sample should be taken (Edwards and Vandenabeele, 2016).

EDXRF on corundum

Well-calibrated EDXRF was firstly used at the beginning of the 1980's, for the chemical analysis of gems. With this technique, natural and synthetic rubies - mainly the ones presenting no inclusions, growth structures or questionable features - can be separated and treatment techniques such as lead-glass filling and coatings can be detected. Tungsten, molybdenum and bismuth are some of the elements that when detected by EDXRF, are the proof of a flux synthetic origin. Some synthetic rubies may contain elements that are characteristic of a treatment or synthesis technique, but not in detectable by EDXRF amounts. In this case, the concentration of other elements such as iron, titanium, vanadium and gallium, must be taken into account. The concentration of these elements is higher in natural rubies than in synthetic ones, or in some cases the elements may be completely absent indicating the nature of a sample. For instance, the presence of gallium in a corundum shows its natural character, while the absence of gallium its synthetic nature. For a clear identification it is always necessary to take into consideration at least two element plots. The same elements can be strong indicators of the geological environment of a natural ruby - marble hosted rubies are characterized by low concentration of iron and medium to high concentration of vanadium, while basalt-related rubies by medium to high iron and low vanadium.

Schwarz et al. (2000) examined sapphire samples from Ambondromifehy and Andranondambo mines in Northern Madagascar and proposed a discrimination between sapphires of a basalt-related origin (Ambondromifehy) from sapphires hosted in skarn-related deposits (Andranondambo) based on $\text{TiO}_2/\text{Ga}_2\text{O}_3$ versus $\text{Fe}_2\text{O}_3/\text{Cr}_2\text{O}_3$ and $\text{Cr}_2\text{O}_3/\text{Ga}_2\text{O}_3$ versus $\text{Fe}_2\text{O}_3/\text{TiO}_2$ plots (Fig. 2.3.4.3).

Wang et al. (2017) used a $\text{Fe-Cr} \cdot 10\text{-Ga} \cdot 100$ diagram, initially proposed by Sutherland et al. (2009), to illustrate the metamorphic origin of Paranesti pargasite-hosted ruby deposits (Fig. 2.3.4.4). Apart from one sample falling in the magmatic field, all samples are scattered in the metamorphic field, when plotted in a Cr/Ga versus Fe/Ti diagram (Fig 2.3.4.5). Corundum

chemistry is frequently done today with LA-ICP-MS. This instrument has a better detection limit for all the elements (e.g., V in corundum should be taken in consideration even in small amounts) as it can also detect light elements (e.g., Mg in corundum), not detectable with EDXRF.

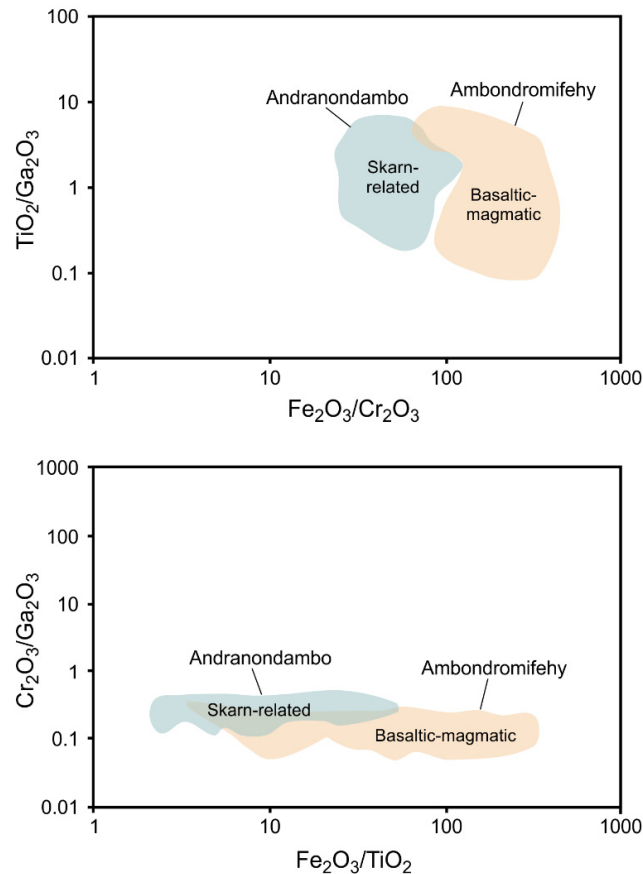


Fig. 2.3.4.3. Trace element correlation diagrams demonstrating the population field of the skarn-related sapphires of Andranondambo slightly overlapping with that of the magmatic samples form Ambondromifehy (modified after Schwarz et al. 2000).

Energy-dispersive X-ray fluorescence (EDXRF) was carried out at DANAT (Manama, Bahrain) with an ARL Quant'X from Thermo Scientific, using a special set of parameters optimized for the analysis of corundum with various conditions of voltage (six steps from 5-30 kV), lifetime (200–300 seconds), and filter type (no filter, cellulose, aluminum, palladium).

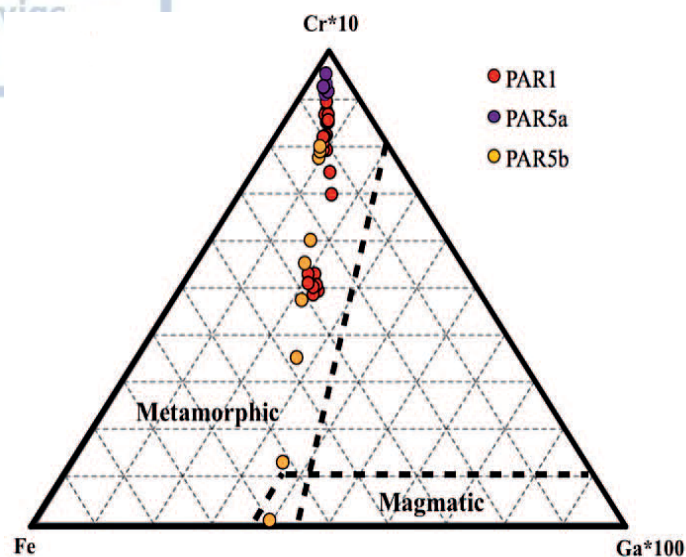


Fig. 2.3.4.4. Trace element discrimination diagram showing the fields for magmatic and metamorphic corundums. PAR1, PAR5a and PAR5b illustrate the plots for Paranesti rubies (Sutherland et al., 2009; modified after Wang et al., 2017).

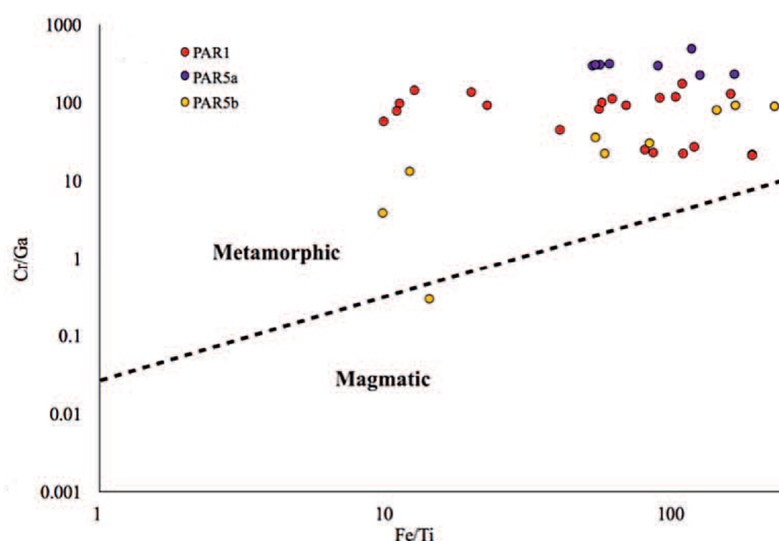


Fig. 2.3.4.5. Trace element discrimination diagrams showing the fields for magmatic and metamorphic corundums and plotting the values of Paranesti rubies (Sutherland et al., 2009; modified after Wang et al., 2017).

2.3.5. Fluid Inclusions

Fluid inclusions shapes and sizes, spatial relationships among inclusions and minerals and phases within inclusions were microscopically observed in a total of 15 double polished thin sections prepared at the Department of Mineralogy, Petrology and Economic Geology of the Aristotle University of Thessaloniki. Microthermometric data in fluid inclusions were obtained

from 15 samples that were suitable for observation during phase transformations. Routine heating and freezing runs were performed at a LINKAM THM-600/TMS 90 heating-freezing stage coupled to a Leitz SM-LUX-POL microscope. Calibration of the stage was achieved using organic standards with known melting points and ice (H₂O), and the precision of the measurements was $\pm 1^{\circ}\text{C}$ during heating and $\pm 0.2^{\circ}\text{C}$ during freezing. The SoWat program (Driesner and Heinrich, 2007) was used to process fluid inclusion data. Phase diagrams were constructed using the methods of Garrels and Christ (1965) and Henley et al. (1984).

CHAPTER 3. RESULTS

3.1. PETROLOGY

Naxos samples: NX1a and NX1b thin-sections illustrate a colorless corundum crystal associated with biotite (or phlogopite?) (Fig. 3.1.1). Under parallel nicols corundum presents blue-hued spots showing no pleochroism. Small zircon crystals are enclosed (Fig. 3.1.2). Fluid inclusions are dispersed all over the corundum crystals, having a linear orientation and usually filling cracks (Fig. 3.1.3, 3.1.4). Under crossed nicols polysynthetic twinning is observed.

Hexagonal euhedral corundum crystals are found in thin-sections NX2a and NX2b, some of them exhibiting blue color zoning and enclosing needle-like mineral inclusions (Fig. 3.1.5). The blue color of corundum is observed either as a blue core surrounded by a white rim or as a blue-zoned outer rim surrounding a colorless core (Fig. 3.1.6). Interference figure taken in the colorless inner part of a blue-rimmed corundum is uniaxial with a small separation of the isogyres indicating strain. Polysynthetic twinning is observed along the colorless parts of the crystals.

Barrel-shaped corundum crystals exhibiting parallel extinction were observed in samples NX4a and NX4b (Fig. 3.1.7). Polysynthetic twinning is observed along the colorless parts of the crystals (Fig. 3.1.8). A colorless micaceous chlorite-like mineral exhibiting anomalous interference colors was found adjacent to corundum (Fig. 3.1.9). Figure 3.1.10 illustrates a corundum crystal exhibiting rhombohedral polysynthetic twinning.

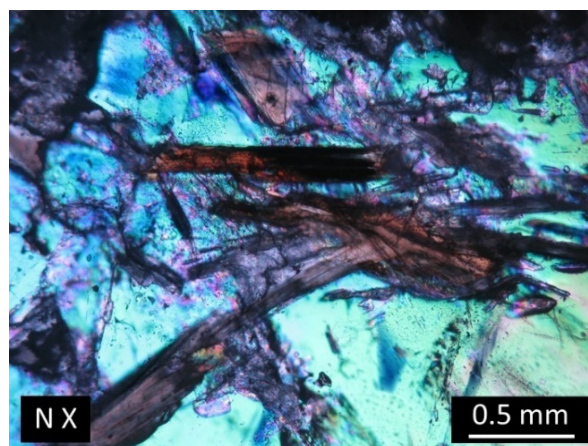
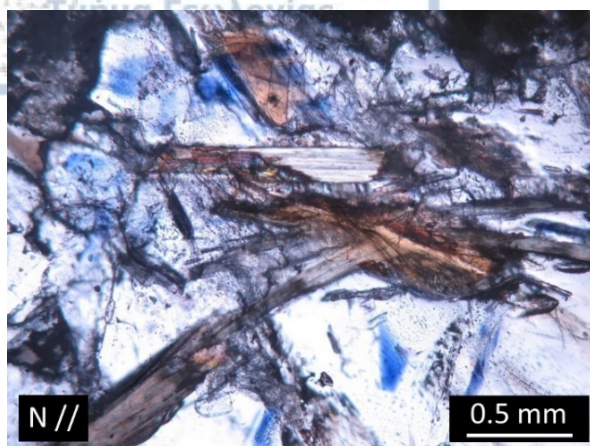


Fig. 3.1.1. Biotite (or phlogopite?) inclusions in a colorless corundum crystal with blue-hued spots exhibiting no pleochroism (thin-section NX1b).

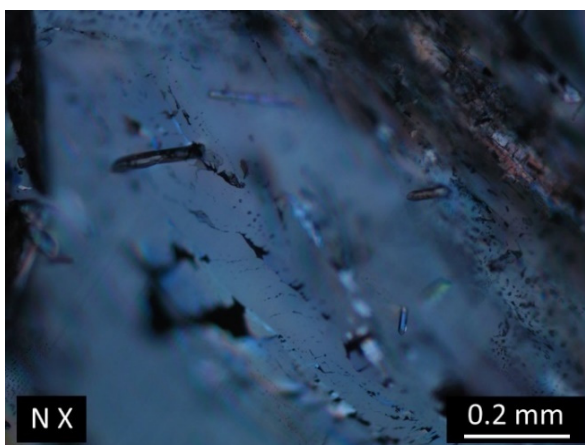
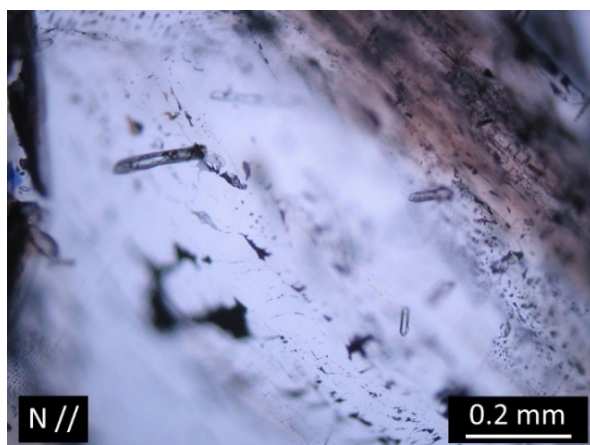


Fig. 3.1.2. Zircon inclusions in corundum (thin-section NX1a).

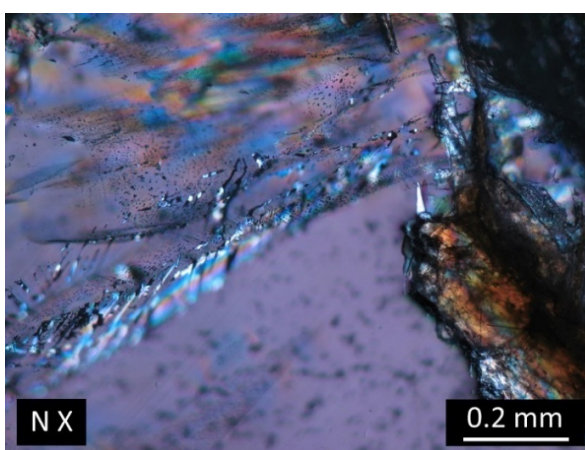
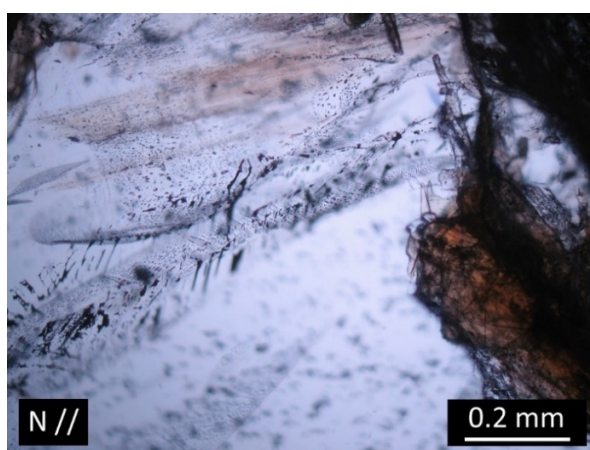


Fig. 3.1.3. Fluid inclusions in corundum with linear orientation. A biotite-like mineral is shown on the right (thin-section NX1a).

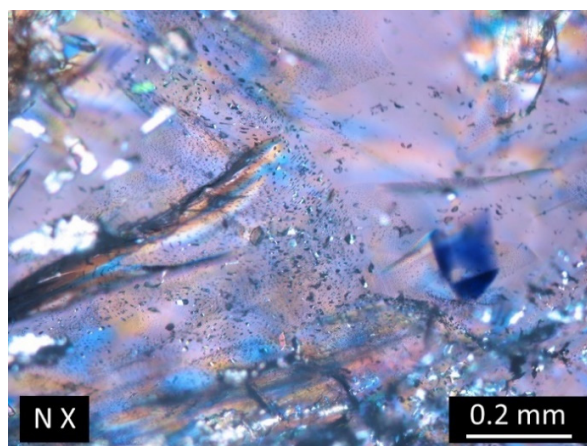
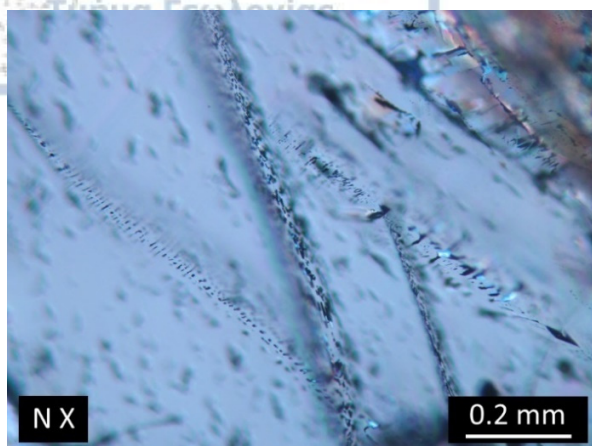


Fig. 3.1.4. Fluid inclusions in corundum with linear orientation (thin-section NX1a).

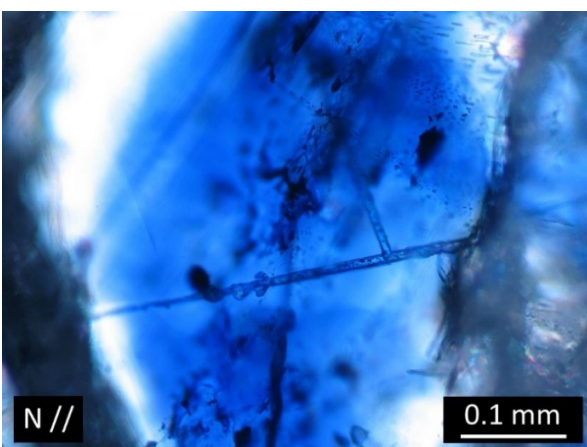
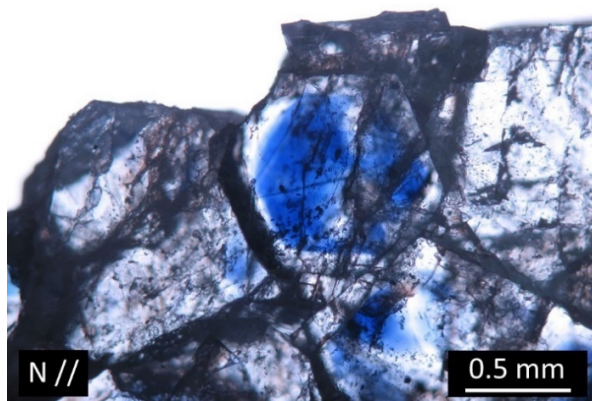


Fig. 3.1.5. Left: Hexagonal euhedral corundum crystal with blue coloration. Right: Needle-like mineral inclusions inside corundum (thin-section NX2b).

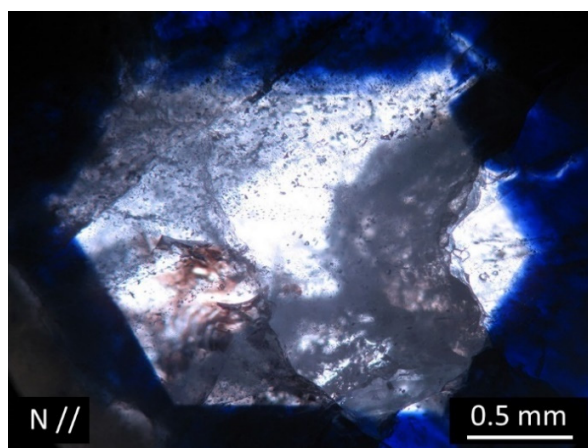
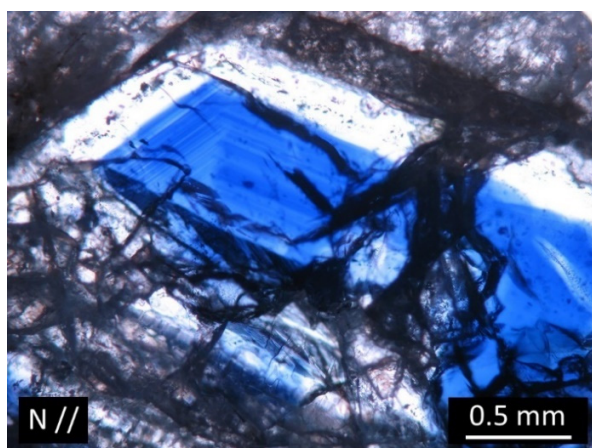


Fig. 3.1.6. Left: Blue core of corundum surrounded by a white rim (thin-section NX2b). Right: Colorless core surrounded by blue rim (thin-section NX2a).

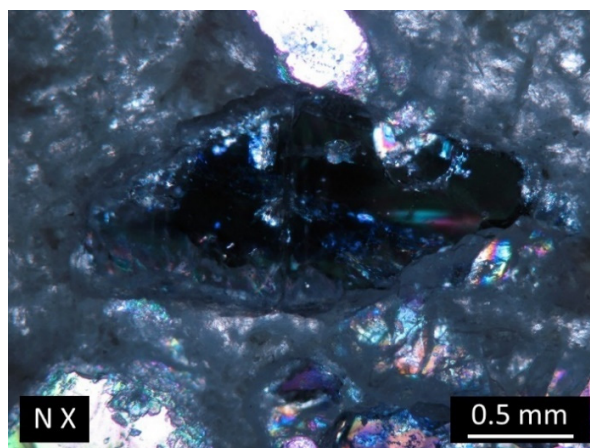
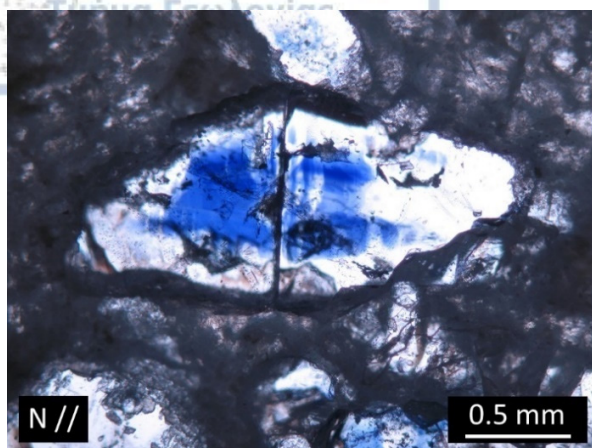


Fig. 3.1.7. Blue-colored barrel shaped corundum crystals exhibiting parallel (thin-section NX4b).

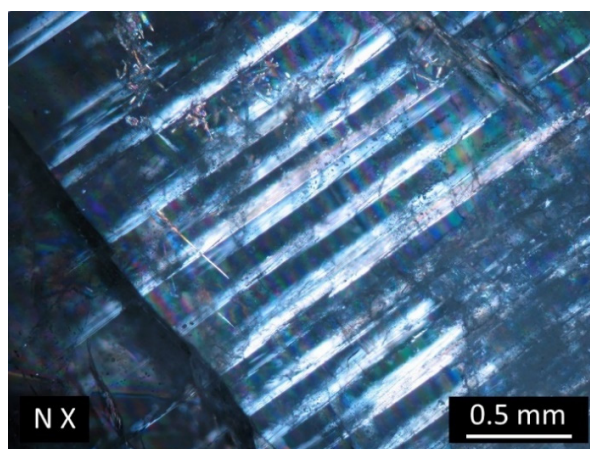
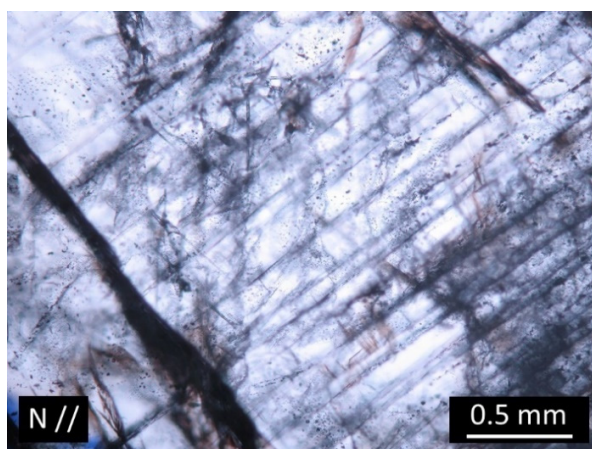


Fig. 3.1.8. Polysynthetic twinning in corundum (thin-section NX4a).

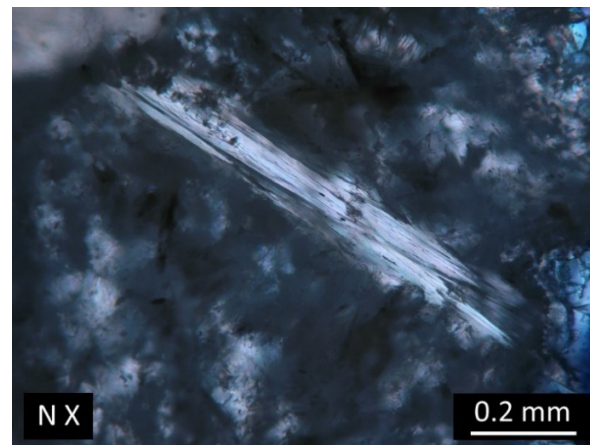
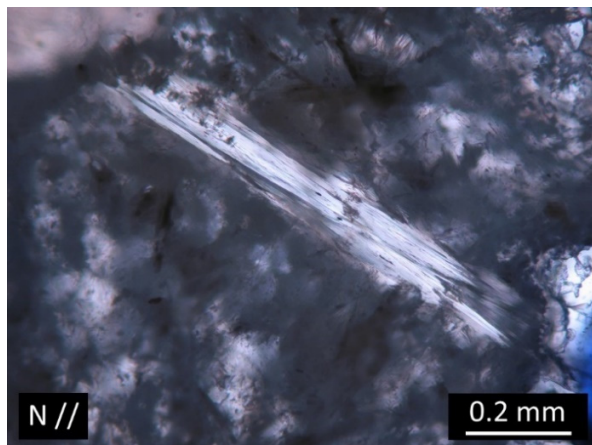


Fig. 3.1.9. A colorless micaceous chlorite-like mineral with anomalous interference colors (thin-section NX4b) (10x)

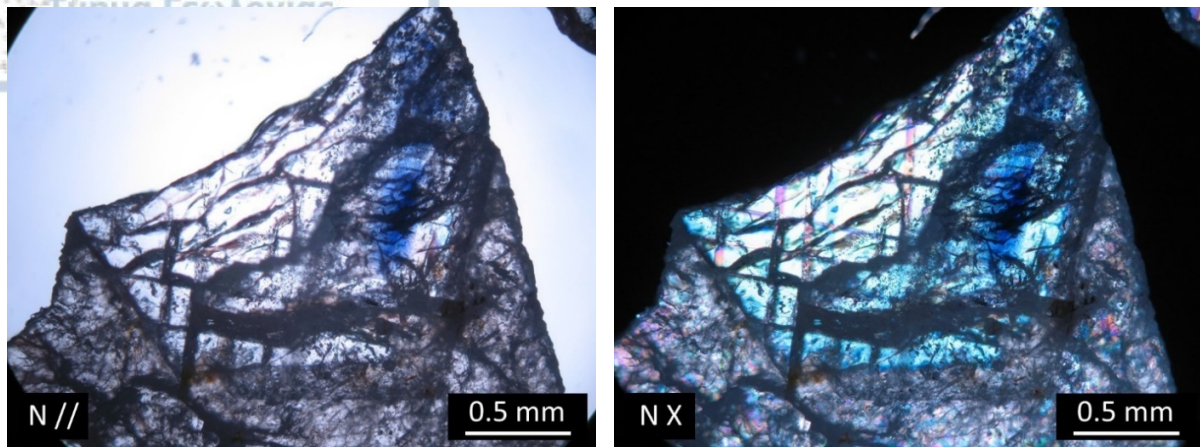


Fig. 3.1.10. Rhombohedral polysynthetic twinning of corundum (thin-section NX4b).

Ikaria samples: In thin section IK1b blue corundum crystals occur as granular masses of anhedral and euhedral crystals of different size (Fig. 3.1.11, 3.1.12). A colorless micaceous margarite-like mineral is observed adjacent to corundum filling most of the cavities between the grains (Fig. 3.1.13, 3.1.14). It is associated with a brown biotite-like mineral aggregate (Fig. 3.1.15). Green spots appear in biotite plates, indicating a possible alteration to chlorite (Fig. 3.1.16).

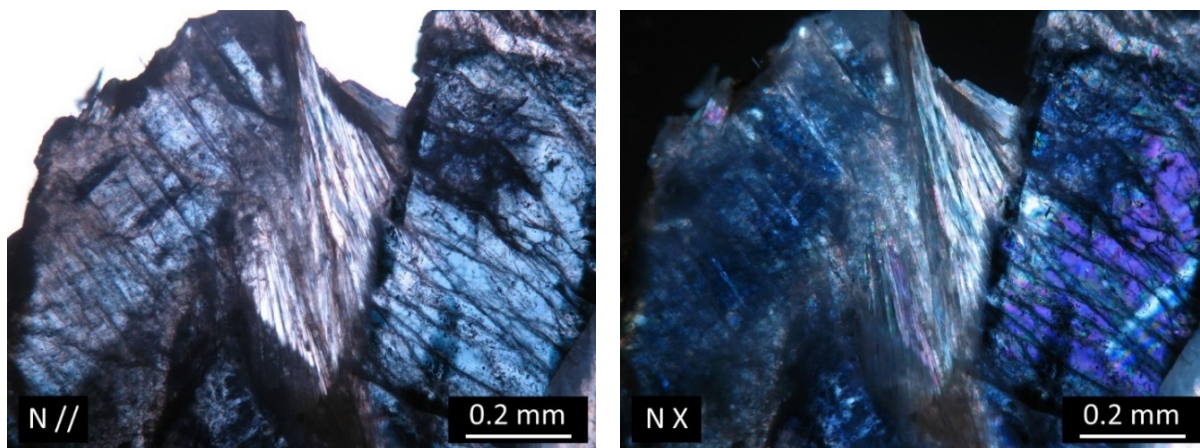


Fig. 3.1.11. Two euhedral blue corundum crystals with a margarite-like mineral in between (thin-section IK1b).

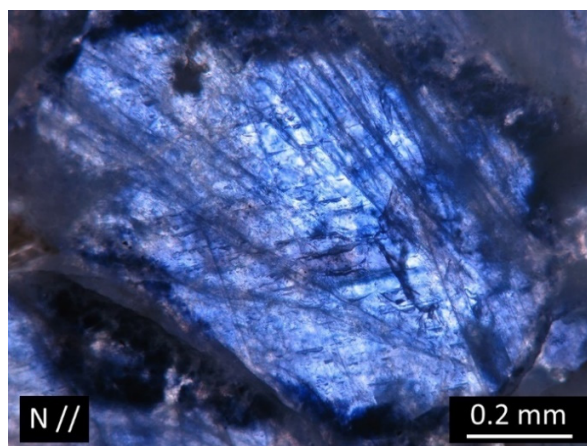
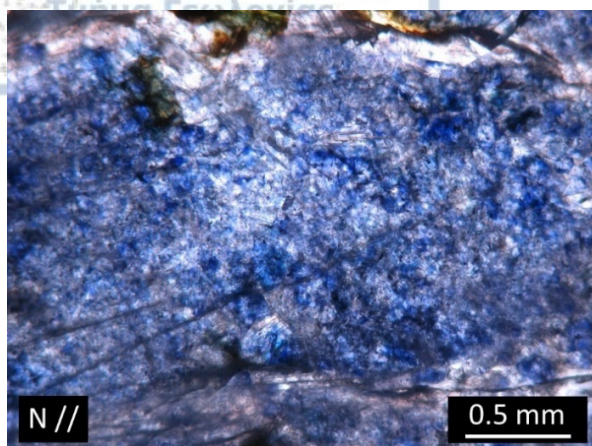


Fig. 3.1.12. Anhedral blue corundum crystals (thin-section IK1b).

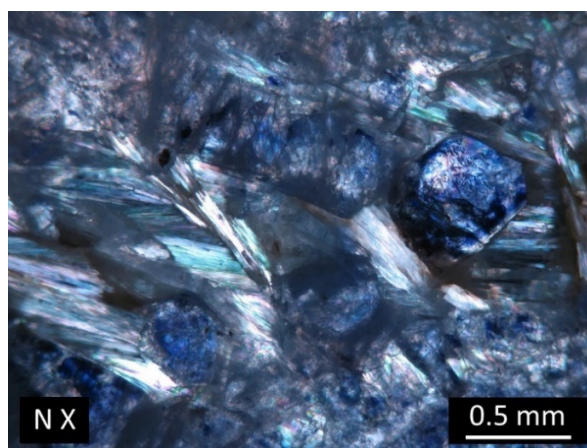
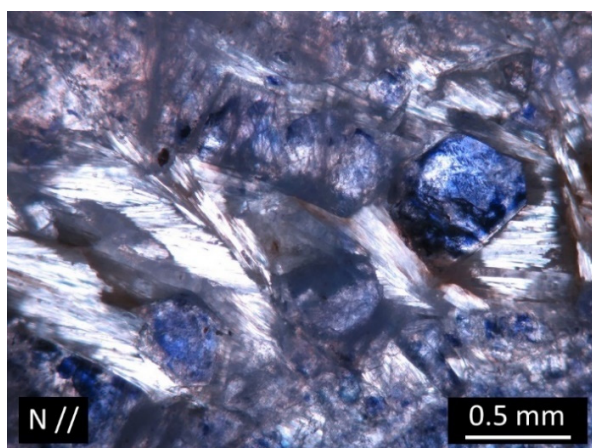


Fig. 3.1.13. A micaceous margarite-like mineral filling the cavities between euhedral corundum grains (thin-section IK1b).

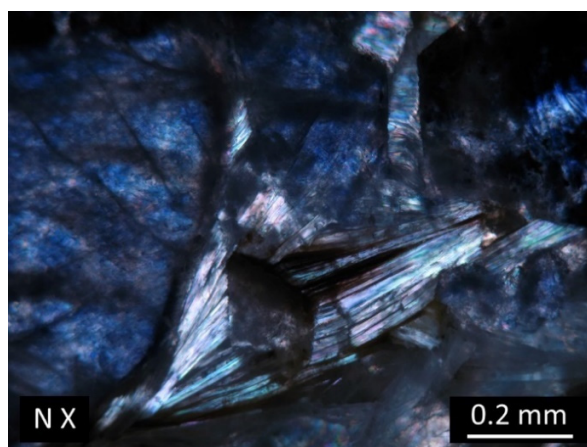


Fig. 3.1.14. A micaceous margarite-like mineral (white) with a biotite-like mineral (brown) filling the cavities between corundum grains (thin section IK1b).

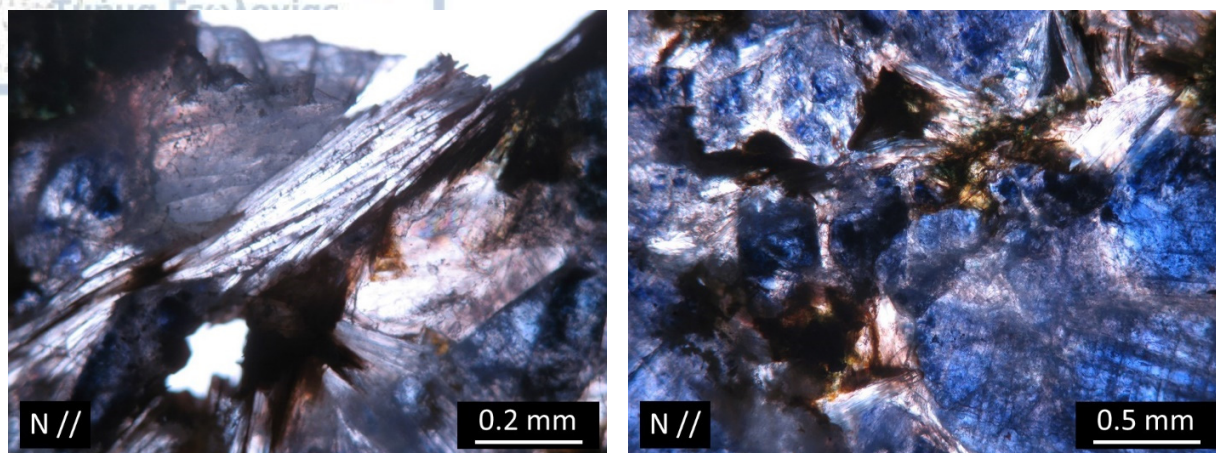


Fig. 3.1.15. Left: Margarite-like mineral (white) intergrowing with biotite-like plates (brown). Right: Assemblage of margarite-like and biotite-like minerals, filling the cavities between corundum grains (thin-section IK1b).

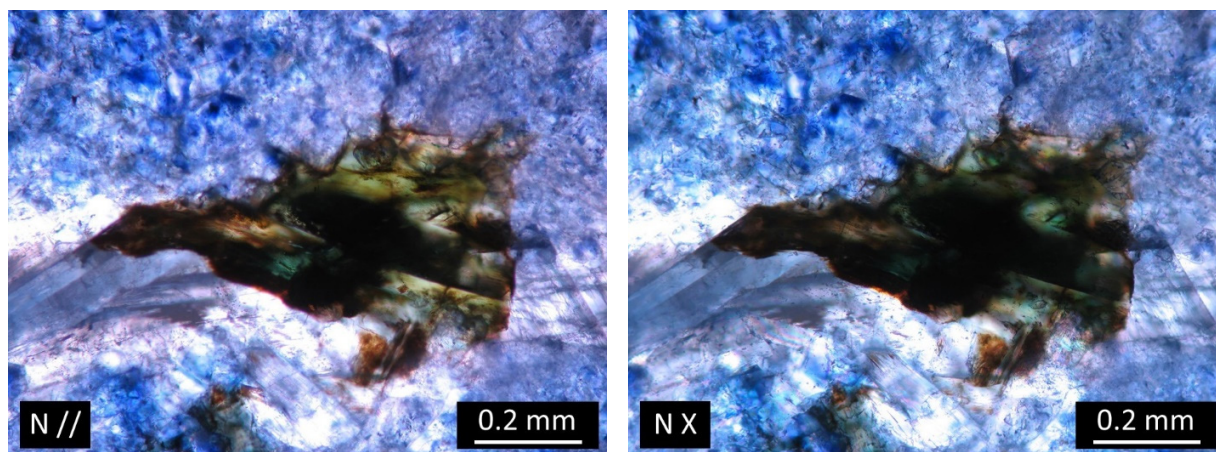


Fig. 3.1.16. Green color on biotite-like plates indicating possible alteration to chlorite (thin-section IK1b).

Xanthi samples: In thin-section GORa corundum crystals under parallel nicols occur as heavily fractured or brecciated crystals of irregularly distributed blue color exhibiting pleochroism (Fig. 3.1.17). They are associated with a brown mineral aggregate, which wasn't able to be identified through the observation with the polar microscope (Fig. 3.1.18). Figure 3.1.19 shows a large kyanite crystal. The corundum crystals in the thin-sections GO5a and GO5b exhibit a light pink color under parallel nicols and a very clear parting (Fig. 3.1.20). The succession of high-order interference colored lamellae indicates the presence of polysynthetic twinning in corundum (Fig. 3.1.21, 3.1.22, 3.1.23). Allanite-like inclusions within corundum are observed in thin-section GO5a (Fig. 3.1.24).

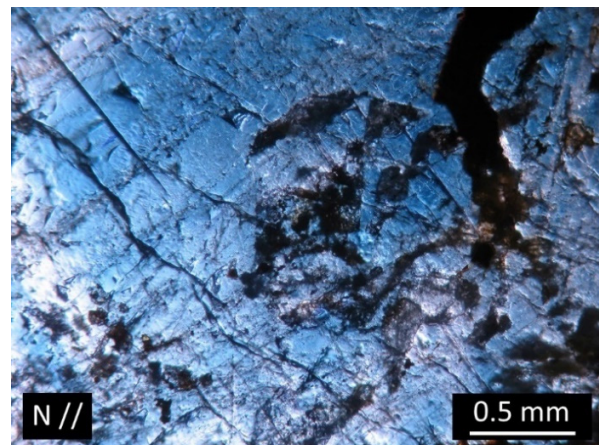
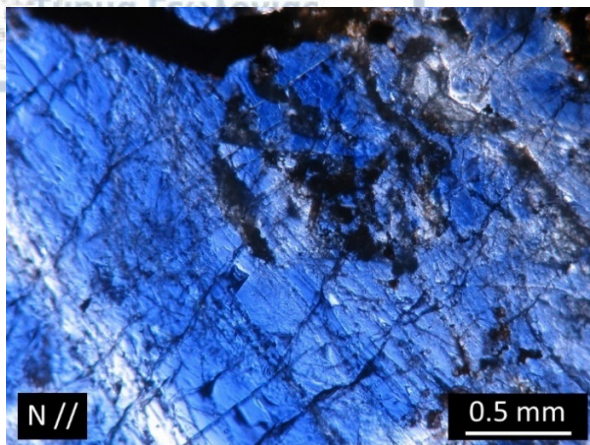


Fig. 3.1.17. Heavily fractured blue colored corundum crystal exhibiting strong pleochroism (thin-section GORa).

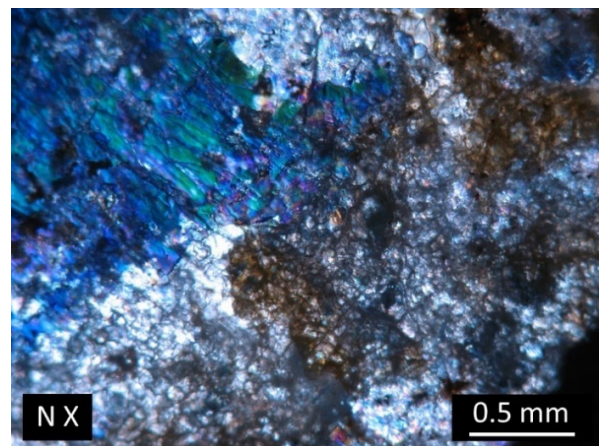
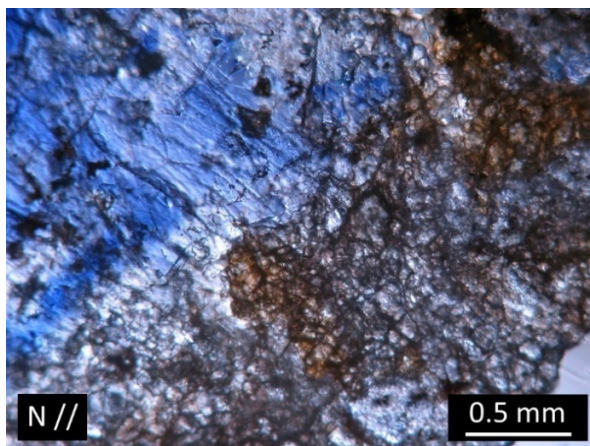


Fig. 3.1.18. Blue corundum crystal associated with a brown mineral aggregate (thin-section GORa).

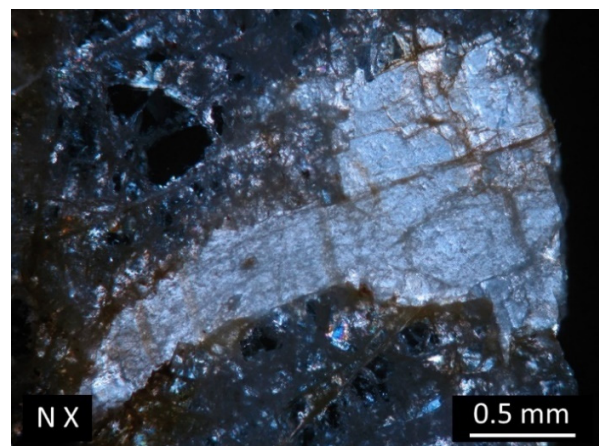
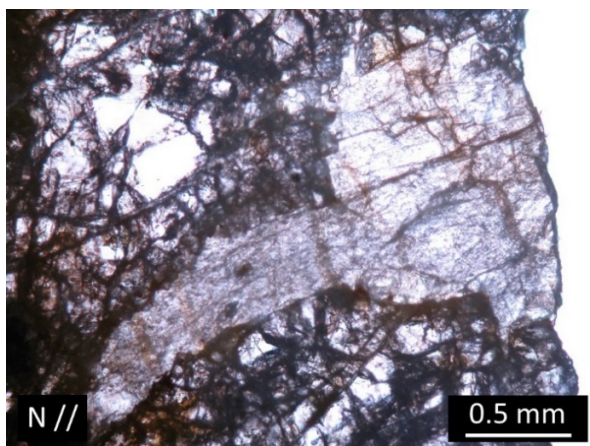


Fig. 3.1.19. Large kyanite crystal (thin-section GORa).

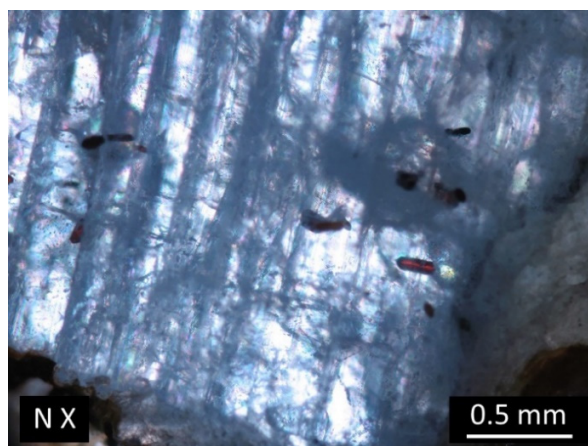


Fig. 3.1.20. Pink corundum crystal with clear parting and allanite inclusions (brown) (thin-section GO5a).

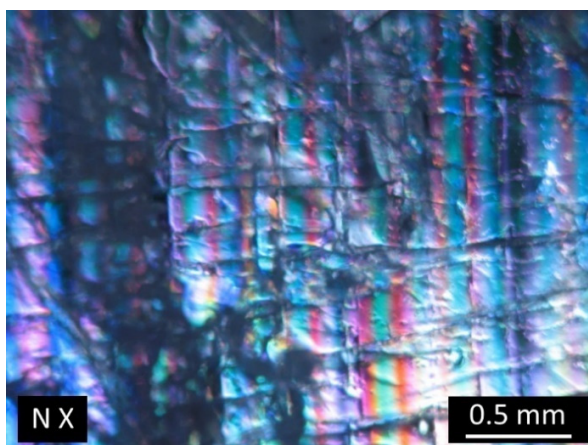
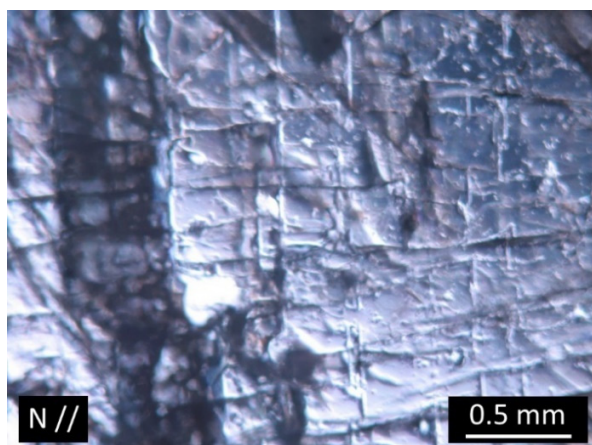


Fig. 3.1.21. Partings and polysynthetic twinning in corundum (thin section GO5b).

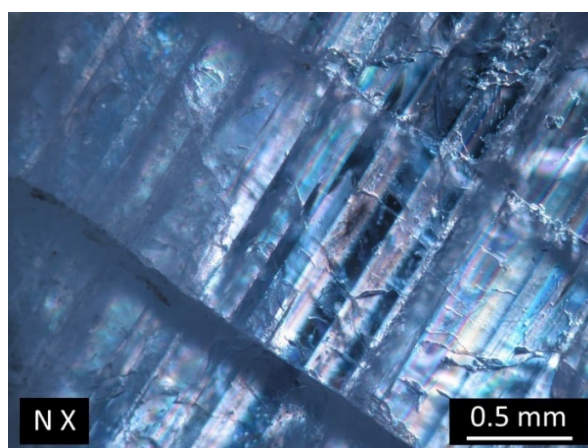
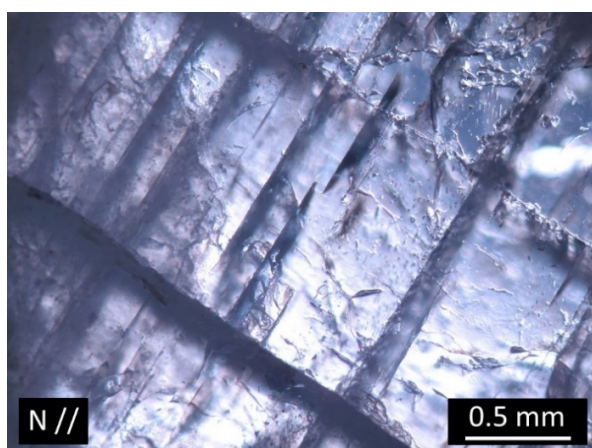


Fig. 3.1.22. Partings and polysynthetic twinning in corundum (thin-section GO5b).

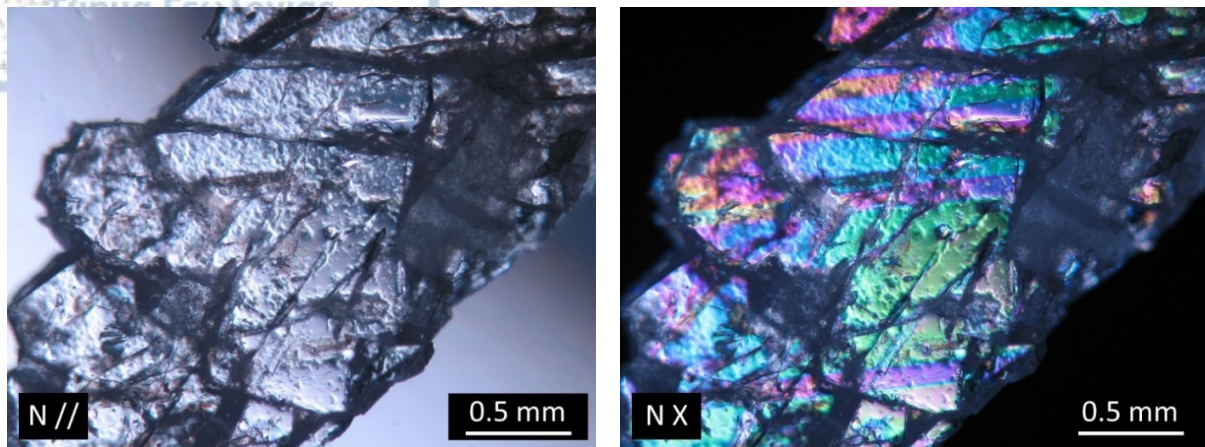


Fig. 3.1.23. Partings and polysynthetic twinning in corundum (thin-section GO5b).

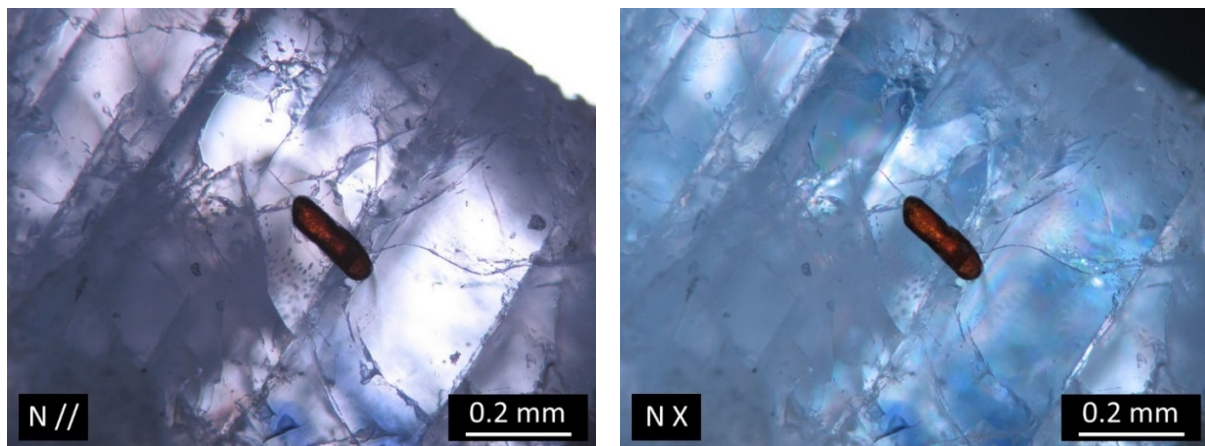


Fig. 3.1.24. Allanite inclusion in corundum (thin-section GO5a).

Drama samples: Under parallel nicols corundum crystals in thin-section DR1a occur as light pink to colorless heavily fractured or brecciated crystals (Fig. 3.1.25). They exhibit clear parting and polysynthetic twinning under crossed nicols (Fig. 3.1.26). Figure 3.1.27 illustrates a green chlorite-like mineral showing pleochroism and anomalous interference colors, filling a crack in corundum. In thin-sections PARa and PARb corundum is less fractured than DR1a's and shows clear parting (Fig. 3.1.28). Under parallel nicols the corundum has a light pink color and exhibits impressive polysynthetic twinning under crossed nicols (Fig. 3.1.29, 3.1.30).

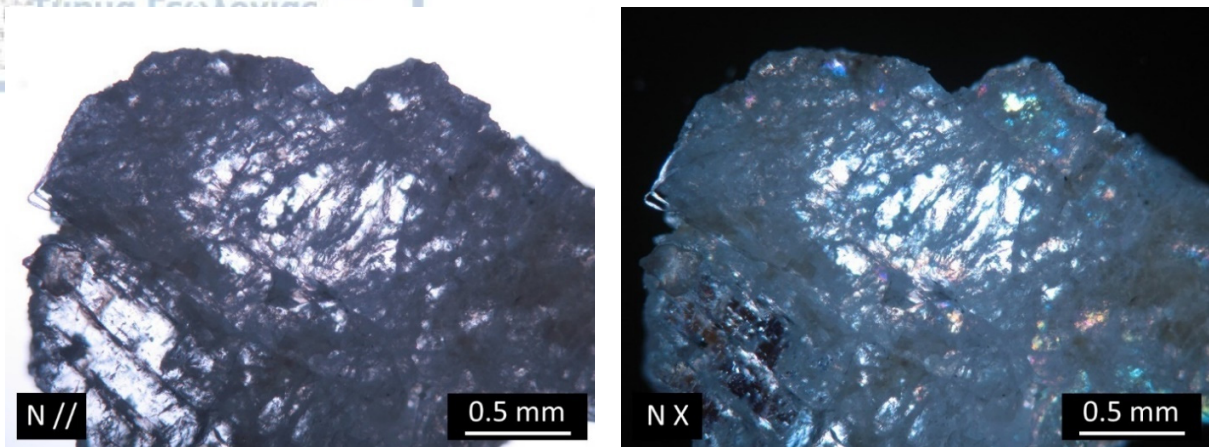


Fig. 3.1.25. Light pink heavily brecciated corundum crystal (thin-section DR1a).

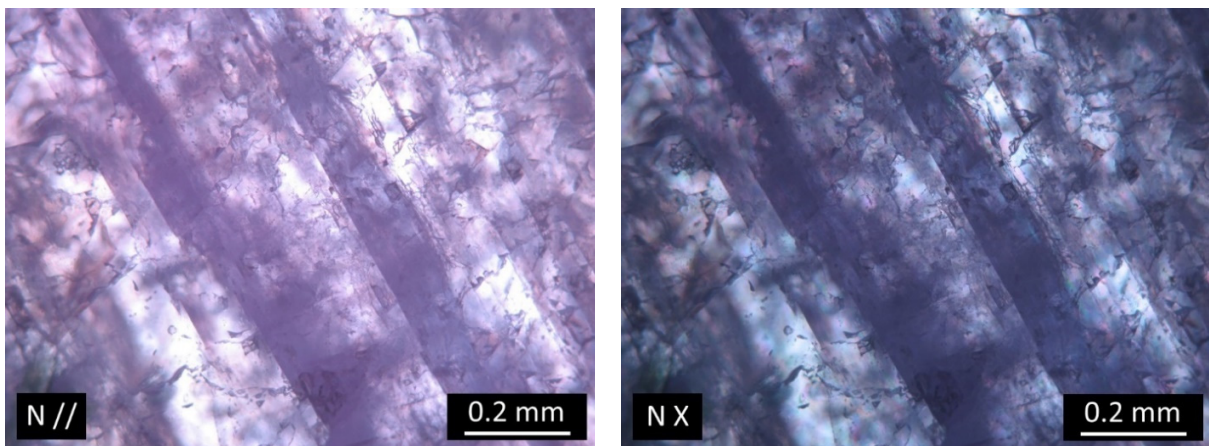


Fig. 3.1.26. Clear parting and polysynthetic twinning in corundum (thin-section DR1a).

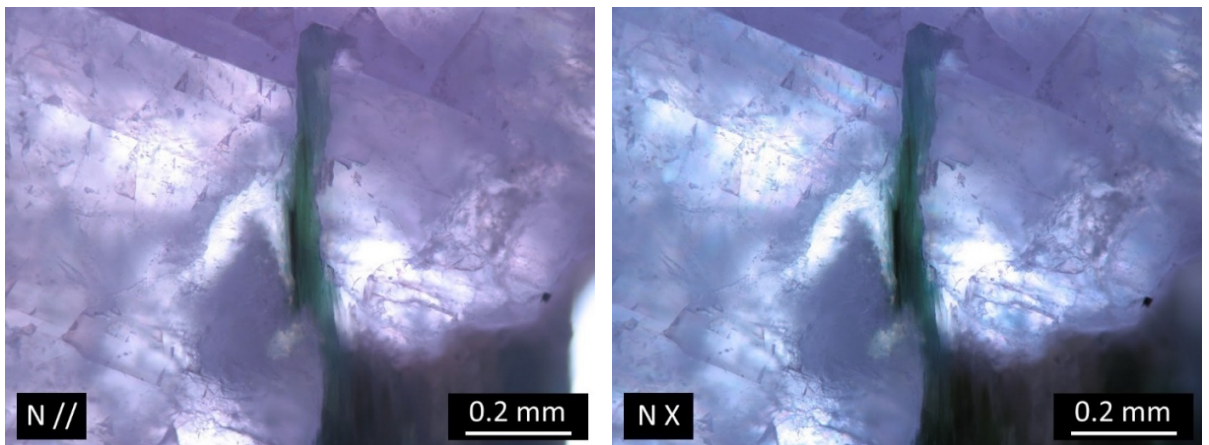


Fig. 3.1.27. Chlorite filling a crack in corundum (thin section DR1a).

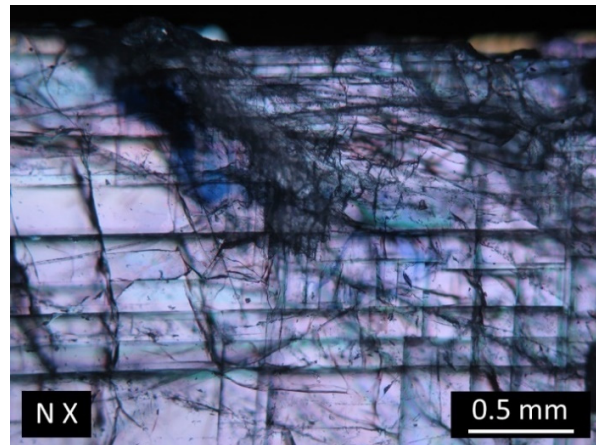
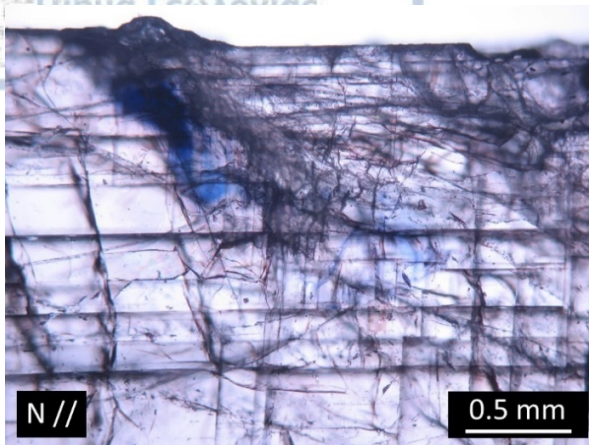


Fig. 3.1.28. Light pink corundum crystal with a blue spot showing clear parting (thin-section PARb).

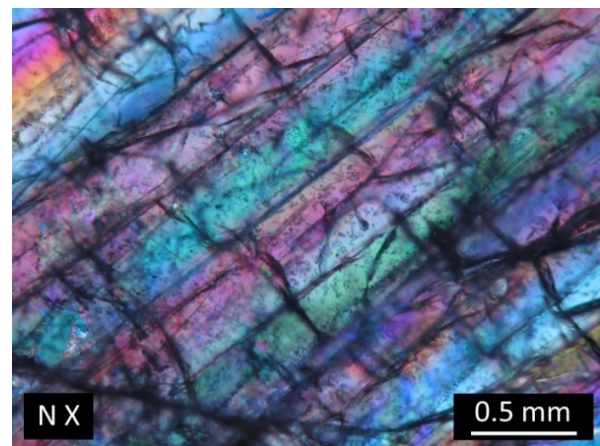
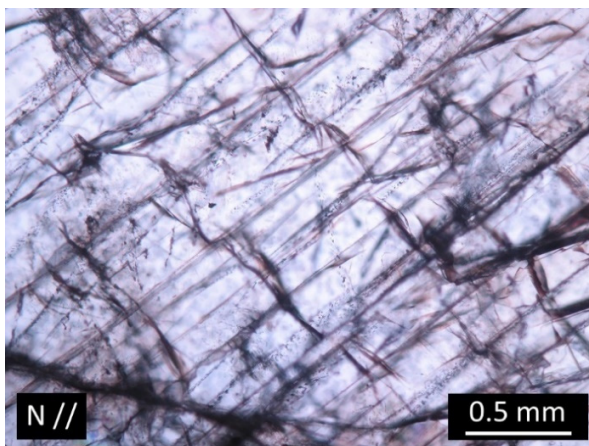


Fig. 3.1.29. Polysynthetic twinning on corundum (thin-section PARa).

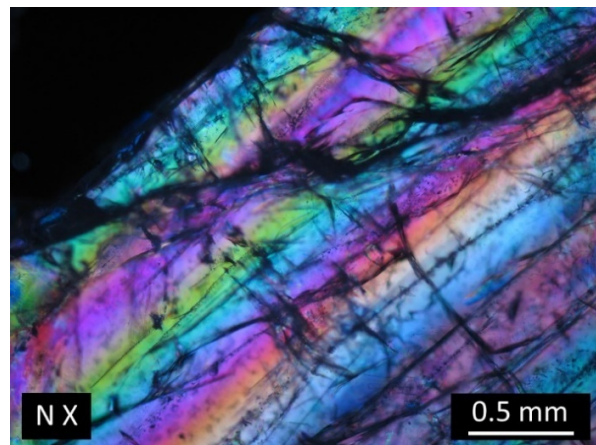
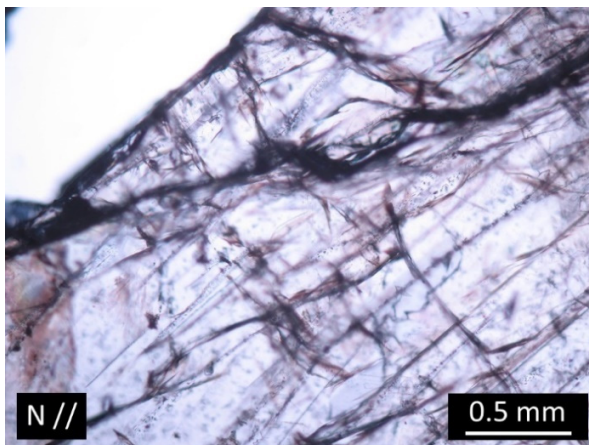


Fig. 3.1.30. Polysynthetic twinning on corundum (thin-section PARa).

In this paragraph the IR spectra acquired from the GGTL are discussed. The analysis was performed in transmission on the corundum samples. Though measurements were taken for all the 15 samples, only the IR spectra of the first 8 samples were deemed suitable for the identification of corundum.

Fig. 3.2.1 illustrates the CO₂ and H₂O measurements of the instrument used for the analysis of the samples. The duplet at approximately 2362 represents the atmospheric CO₂ while the noisy band between 3500 and 3900 cm⁻¹ the H₂O of the instrument.

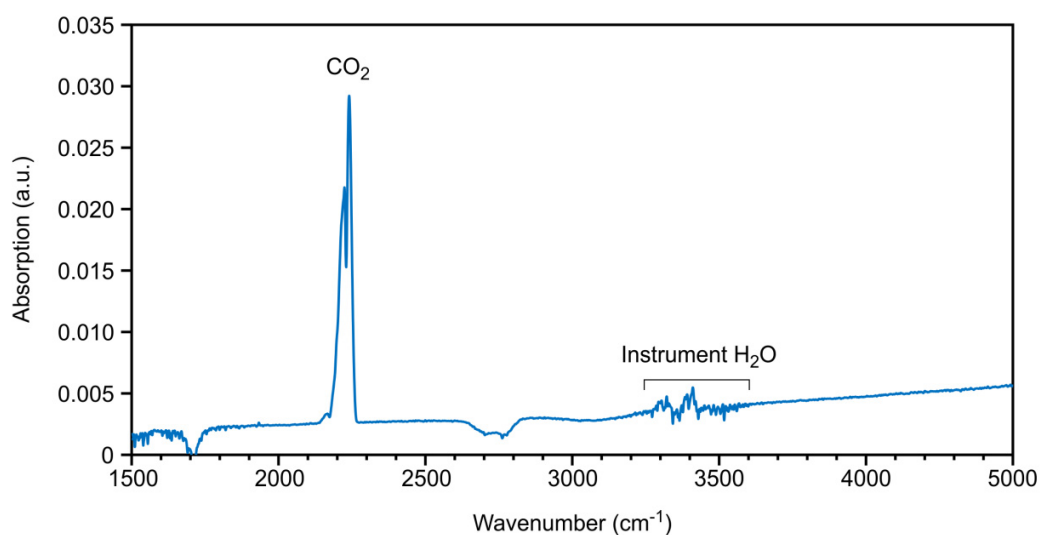


Fig. 3.2.1. Absorption spectra of CO₂ and H₂O.

In Fig. 3.2.2, the IR spectra acquired in transmission for the samples NX1a, NX2a and NX4a are presented. Measurements were taken in both the blue and whitish spots of the crystal, with no apparent difference being noticed in the spectra (Fig.3.2.2). The spectra of all the three samples present small peaks at approximately 1980 and 2109 cm⁻¹, indicating the presence of boehmite (Bhm) (Emmett et al., 2017). A doublet between 2300 and 2400 cm⁻¹, probably assigned rather to CO₂ from fluid inclusions than from the atmospheric CO₂ (organic matter vibrations), is obvious (Phan, 2015). The broad noisy band developing between 3500 and 4000 cm⁻¹ could correspond either to chlorite (Beran and Rossman, 2006) and other micas or rutile inclusions, but since it presents no characteristic features it is probably related to the H₂O of the instrument.

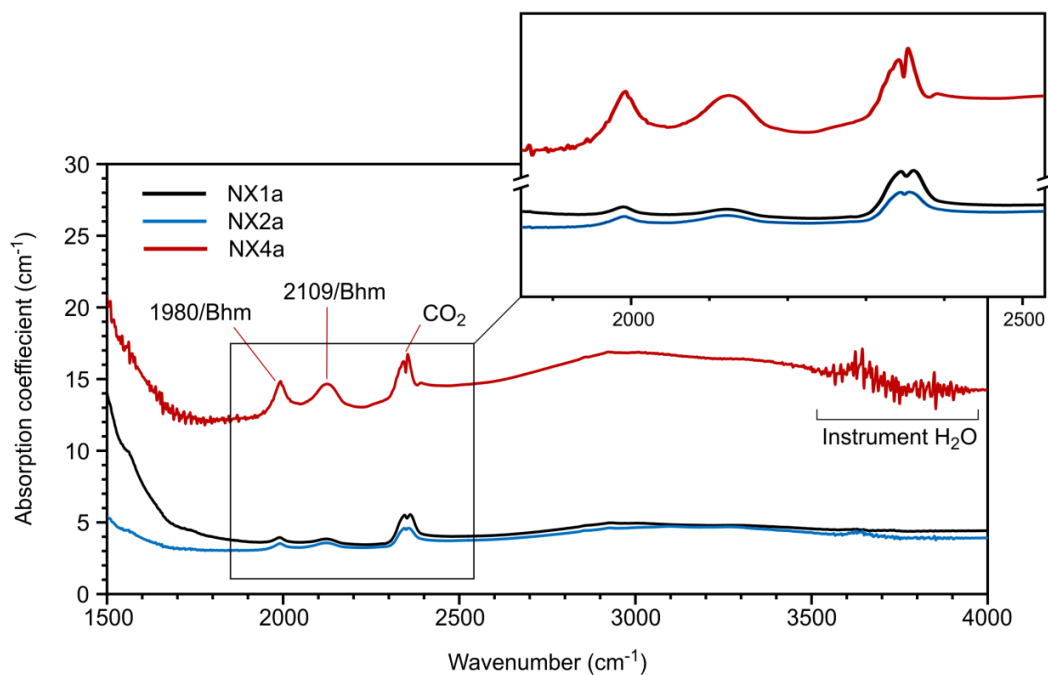


Fig. 3.2.2. Absorption spectra of corundum NX1a, NX2a and NX4a.

In Fig. 3.2.3 the boehmite peaks at 1980 and 2109 cm^{-1} are clearer with additional small peaks at 3278 and 3391 cm^{-1} , as is the CO_2 absorption at 2360 cm^{-1} related to fluid inclusions because of its clear shoulder. A small peak at around 3111 cm^{-1} possibly assigned to goethite (Gth) is also visible (Beran and Rossman, 2006; Emmett et al., 2017). In the noisy area between 3500 and 4000 cm^{-1} a small peak at 3645 cm^{-1} discerns probably attributed to chlorite (Chl) (Emmett et al., 2017). The peaks at 2872 and 2936 cm^{-1} are indicators of finger grease (Emmett et al., 2017).

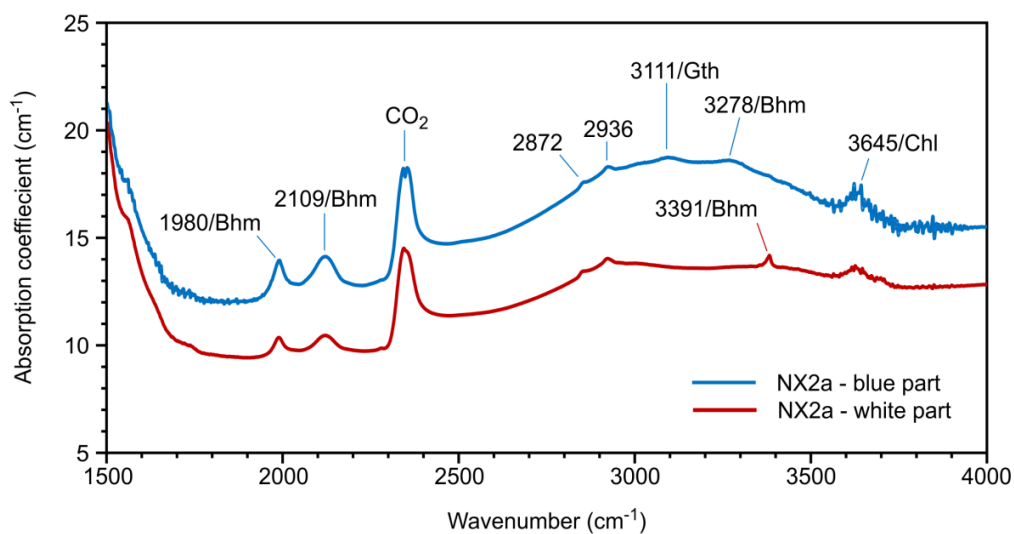


Fig. 3.2.3. Absorption spectra of corundum NX2a in different parts of the sample.

The strongest absorption of OH was acquired by the Ikaria samples (IK1a, IK1b), as shown in the Fig.3.2.4. The strong peaks at approximately 1994 and 2130 cm^{-1} , together with the peaks at 3082 and 3302 cm^{-1} are correlated to boehmite (Emmett et al., 2017). The 2900 and 3020 peaks indicate the presence of diasporite (Dsp) (Smith, 1995; Beran and Rossman, 2006; Emmett et al., 2017), while the small absorption at 3627 cm^{-1} is related to chlorite (Beran and Rossman, 2006). The small absorption at around 2861 cm^{-1} may be related to finger grease. The CO_2 -fluid inclusion related peak at around 2355 cm^{-1} is discernible (Phan, 2015).

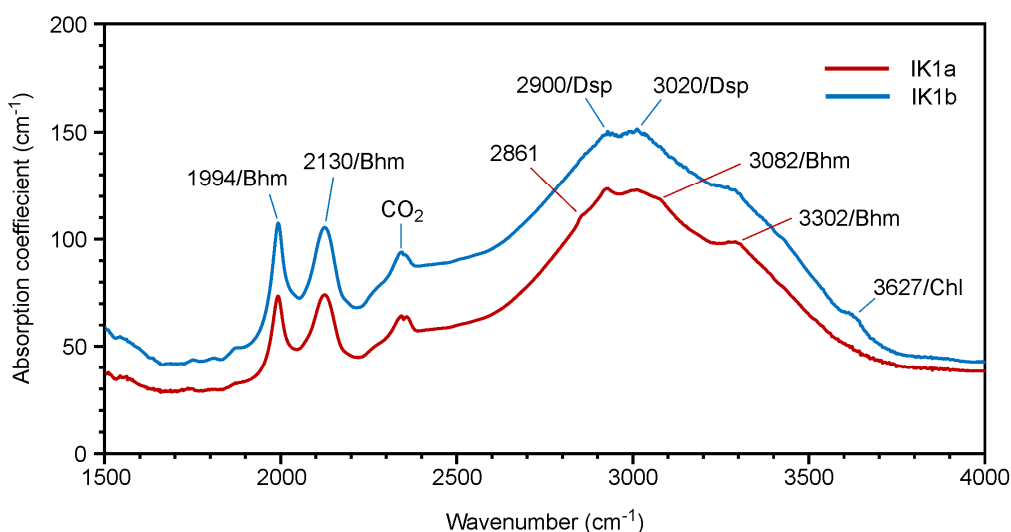


Fig. 3.2.4. Absorption spectra of samples IK1a and IK1b.

Gorgona's spectra are quite similar to Ikaria's, presenting peaks at approximately the same wavelength but of lesser intensity. In both GORa and GO5 the bands with the stronger intensity present many shoulders, rendering it difficult to detect the exact position of the stronger absorption. The series of peaks for the sample GORa (Fig. 3.2.5) at 1989, 2121, 3068 and 3306 cm^{-1} and for the sample GO5a at 1990, 2123, 3069 and 3307 cm^{-1} approximately, corroborate the presence of boehmite in both samples (Emmett et al., 2017). The 2930 and 3015 peaks in sample GORa and the 2938 and 3002 in sample GO5a are related to diasporite (Smith, 1995; Beran and Rossman, 2006; Emmett et al., 2017). The CO_2 absorption peaks in both samples are attributed to the CO_2 of fluid inclusions (Phan, 2015). The noisy area between 3500 and 4000 related to H_2O from the instrument is also visible. In the sample GO5a two small peaks at around 3500 and 3600 cm^{-1} indicate possibly the presence of chlorite (Beran and Rossman, 2006). Sample GOR

shows a small peak around 2500 cm^{-1} probably attributed to calcite (Emmett et al., 2017). A similar but hardly visible peak may be observed in sample GO5.

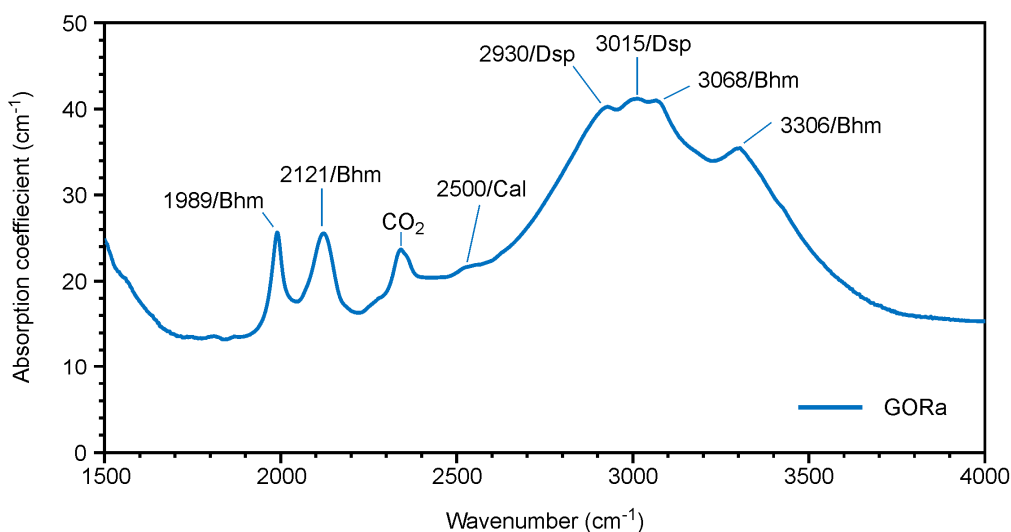


Fig. 3.2.5. Absorption spectra of sample GORa.

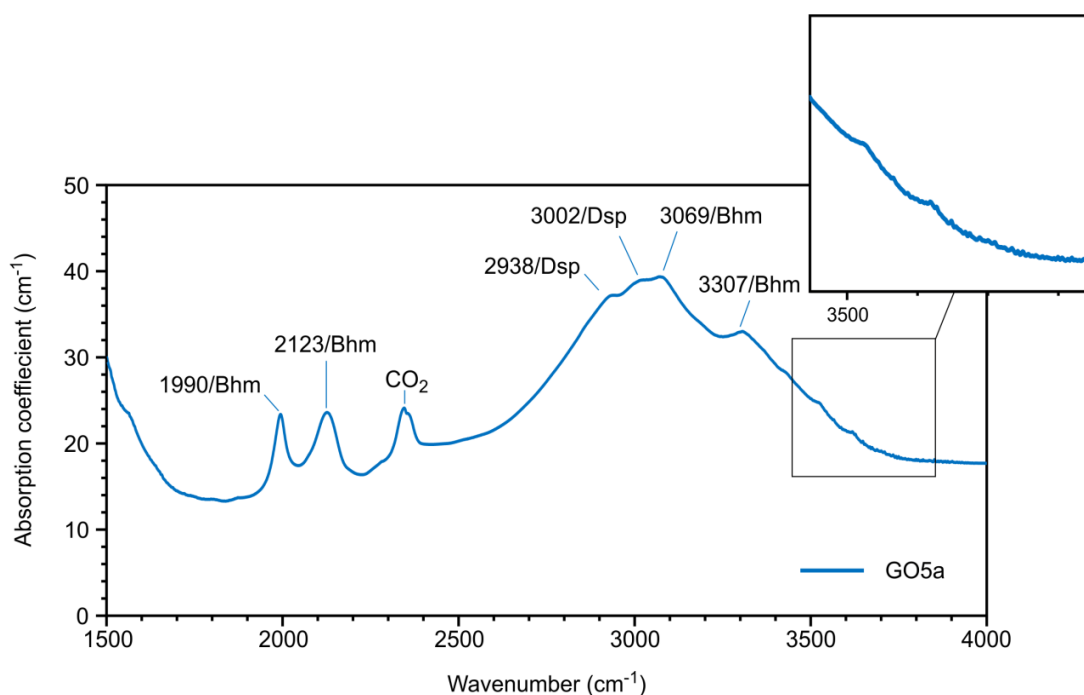


Fig. 3.2.6. Absorption spectra of sample GO5a.

OH absorptions are reported in closely the same position in the IR spectra of the Drama samples (Fig. 3.2.7). Sample DR1a shows typical boehmite-related OH absorption at approximately 1996, 2141, 3096 and 3325 cm^{-1} . Respectively, the same boehmite related peaks

for the sample PARa (Fig. 3.2.8), appear around 1987, 2118, 3095 and 3328 cm^{-1} (Emmett et al., 2017). The maximum peak at 3095 cm^{-1} along with the 3328-peak have quite sharp and narrow shoulders in opposition to the respective peaks of the rest of the samples. Diaspore related peaks are present at 2938 and 3025 cm^{-1} for sample DR1 and a small one appears at 2938 cm^{-1} for sample PAR (Smith, 1995; Beran and Rossman, 2006; Emmett et al., 2017). The CO_2 from fluid inclusions absorption is visible in both samples (Phan, 2015). In sample DR1 a small peak around 3635 cm^{-1} indicates the presence of chlorite, as does a small one at 3650 cm^{-1} for sample PAR (Beran and Rossman, 2006).

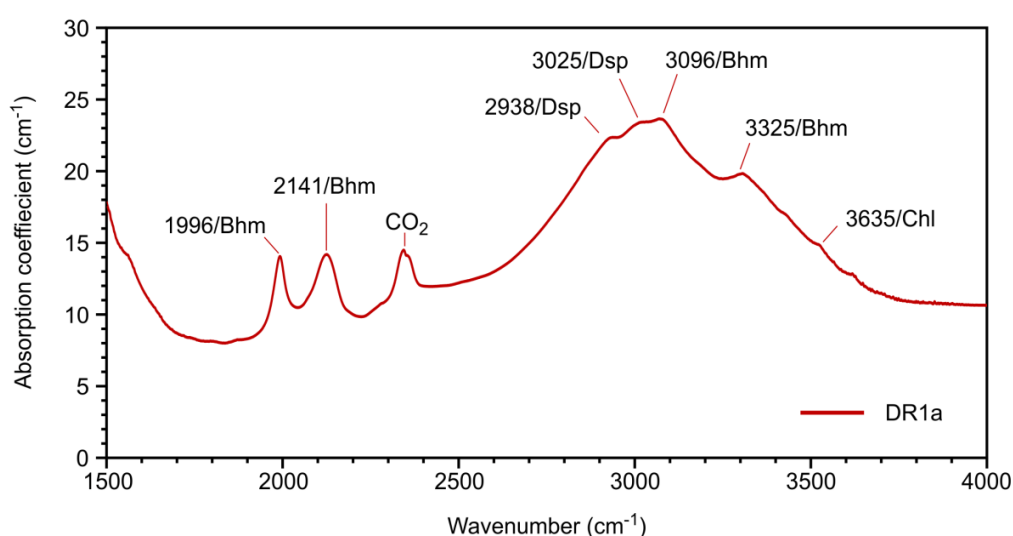


Fig. 3.2.7. Absorption spectra of sample DR1a.

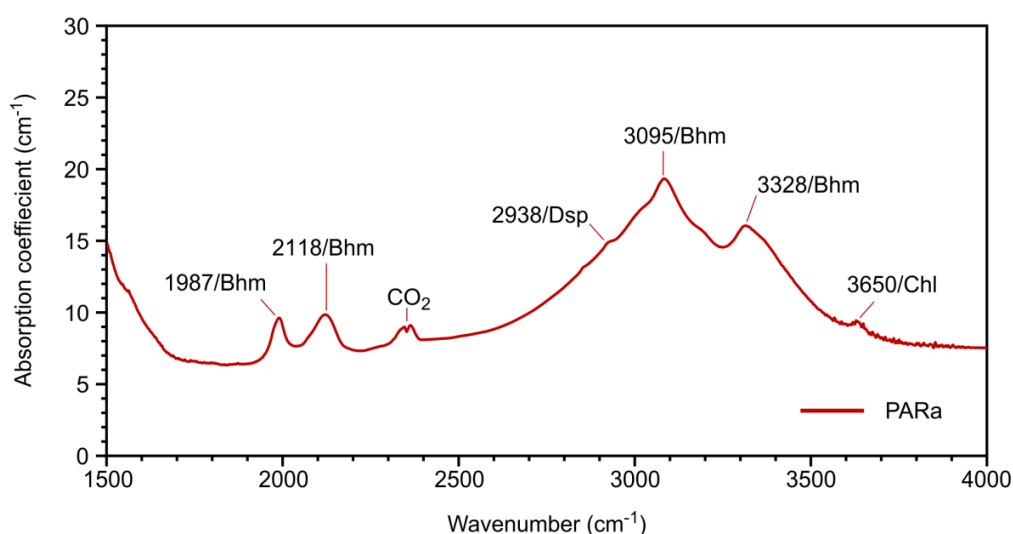


Fig. 3.2.8. Absorption spectra of sample PARa.

3.3. UV-VIS-NIR SPECTROSCOPY

UV-Vis-NIR measurements were conducted for all the 18 pieces (9 different samples), but only the most characteristic ones are presented below. The UV range is completely absorbed up to 300 nm. No iron related absorption band above 700 nm is detected in any studied sample.

All Naxos' samples show Fe^{3+} and $\text{Fe}^{2+}/\text{Ti}^{4+}$ absorption features. NX1 (Fig. 3.3.1) presents characteristic Fe^{3+} peaks at 377, 388 and a smaller one at 450 nm, as well as a very weak $\text{Fe}^{2+}/\text{Ti}^{4+}$ peak. At around 330 nm, there is a full absorption ("cut off"). No shoulder between 300 and 350 nm is visible. Samples NX2 and NX4 (Fig. 3.3.2, 3.3.3) present quite different spectra. Weak Fe^{3+} peaks at 377 and 388 nm and a strong absorption band between 500 and 700 nm, related to $\text{Fe}^{2+}/\text{Ti}^{4+}$ intervalence charge transfer, are present in both samples. In sample NX2 the $\text{Fe}^{2+}/\text{Ti}^{4+}$ absorption band is quite strong. Sample NX4 presents an additional Fe^{3+} peak at 450 nm. Both samples present a very weak and hardly visible shoulder of debatable origin (Emmett et al., 2017) at around 330 nm. NX2 presents a "cut off" at around 300 nm, while NX4 at around 320 nm.

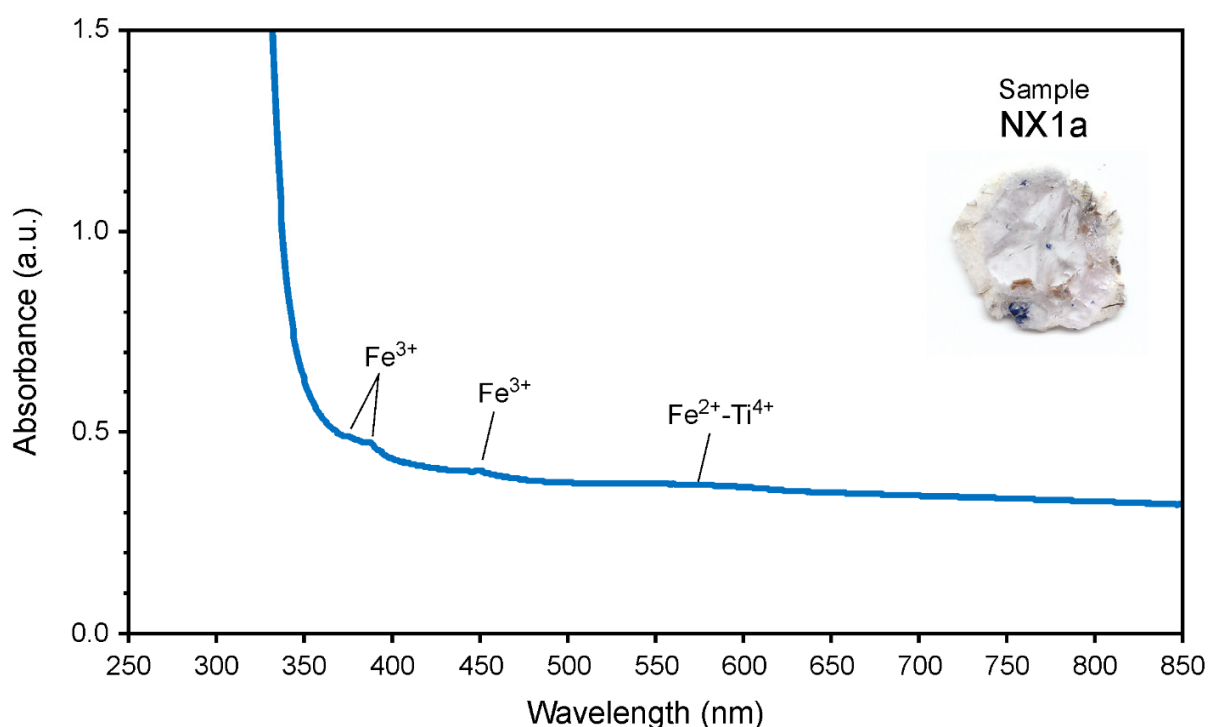


Fig. 3.3.1. UV-Vis-NIR absorption spectra of blue to colorless sapphire NX1 from Naxos.

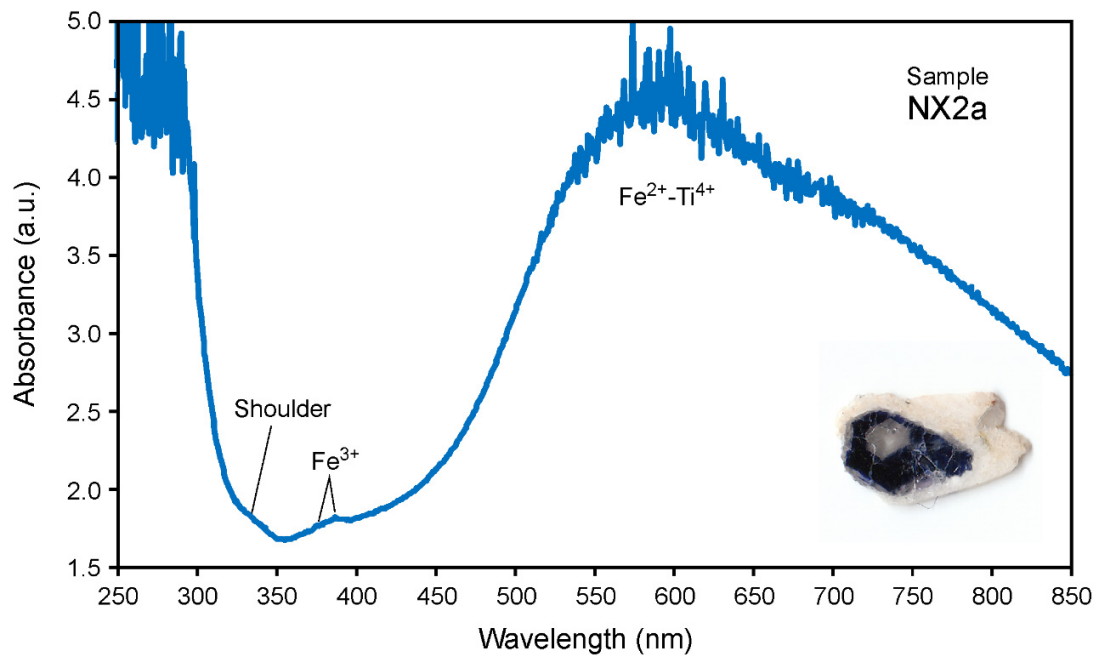


Fig. 3.3.2. UV-Vis-NIR absorption spectra of blue to colorless sapphire NX2 from Naxos.

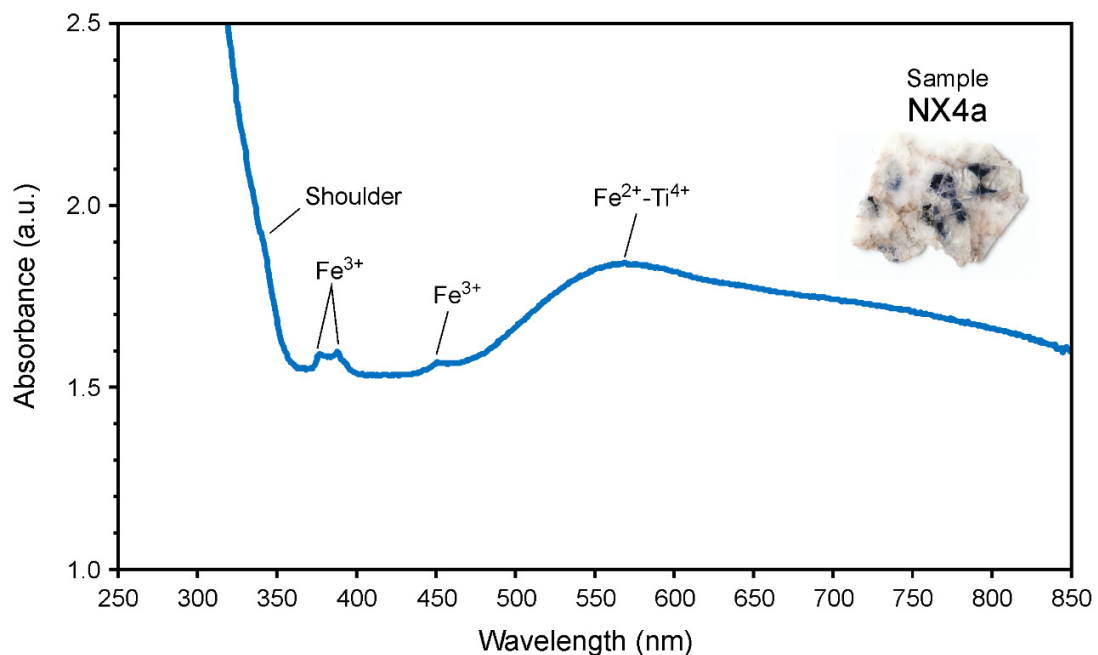


Fig. 3.3.3. UV-Vis-NIR absorption spectra of blue to colorless sapphire NX4 from Naxos.

UV-Vis-NIR absorption spectra of Ikaria's samples (Fig. 3.3.4) are typically contributed by a broad band between 500 and 700 nm with a maximum at around 570 nm, typical of intervalence charge transfer by $\text{Fe}^{2+}/\text{Ti}^{4+}$, accompanied by weak Fe^{3+} peaks at approximately 377, 387 and 450 nm. IK1b presents a full absorption ("cut off") at around 300 nm and the shoulder of debatable origin at 330 nm.

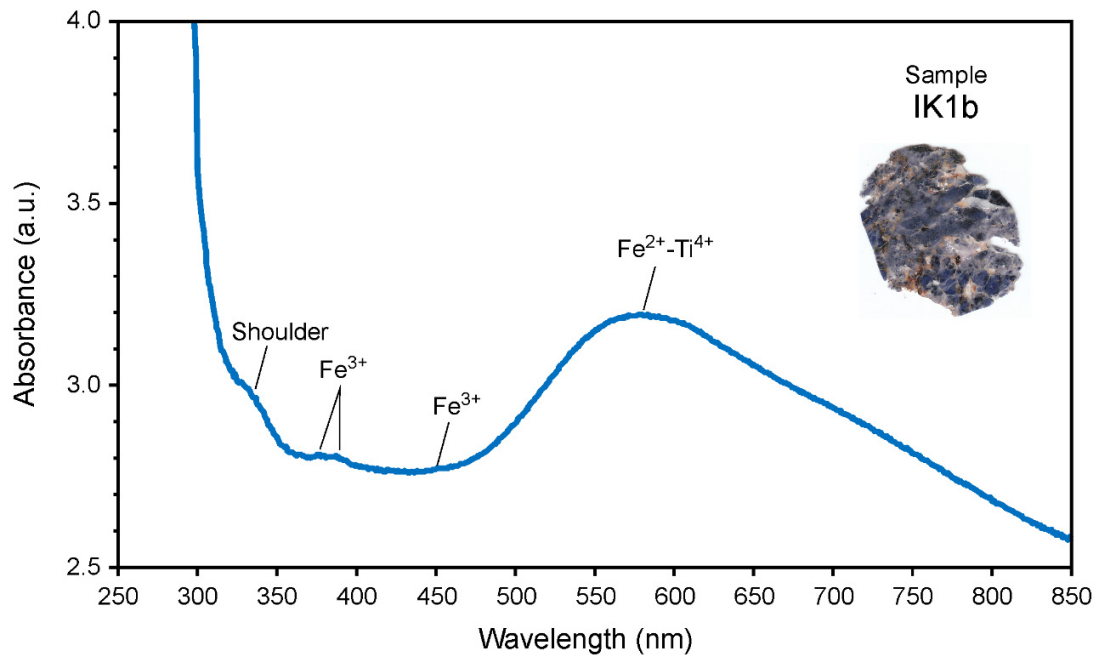


Fig. 3.3.4. UV-Vis-NIR absorption spectra of IK1 blue sapphire from Ikaria.

Xanthi's samples present a strong variation. Sample GOR (Fig. 3.3.5) shows a broad absorption between 500 and 700 nm with a maximum near 570 nm, attributed to intervalence charge transfer by $\text{Fe}^{2+}/\text{Ti}^{4+}$, and weak Fe^{3+} bands at around 377 and 388 nm. A weak shoulder of debatable origin at around 340 nm is visible. The "cut off" for this sample is located at around 320 nm.

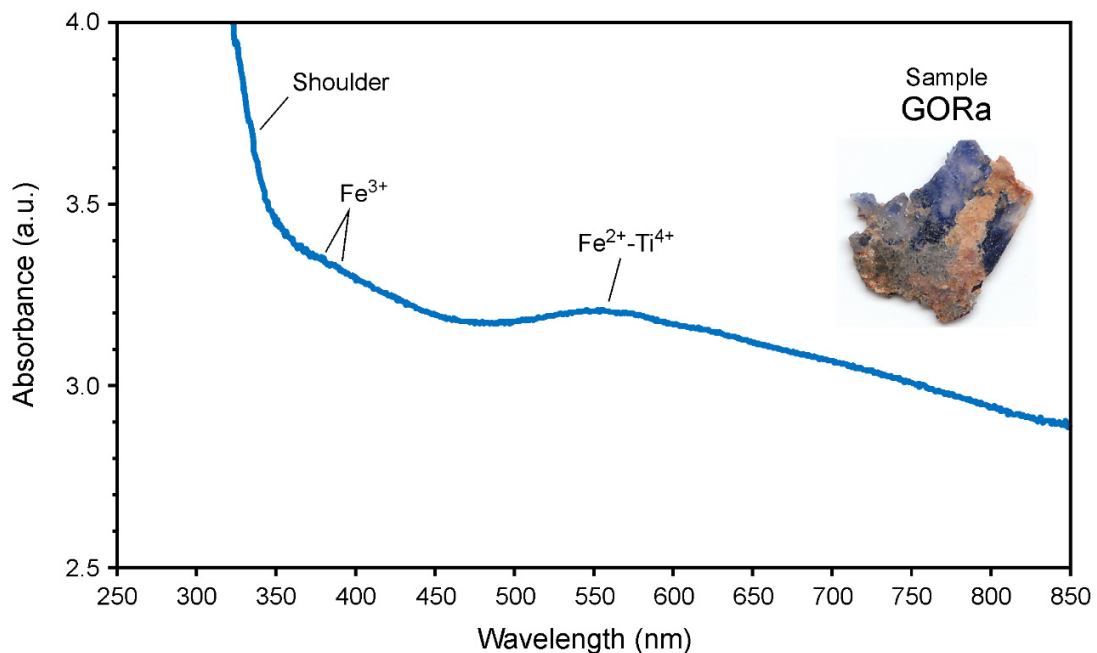


Fig. 3.3.5. UV-Vis-NIR absorption spectra of GOR blue sapphire from Xanthi.

Sample GO5 (Fig. 3.3.6) presents a quite different spectrum than GOR's. Weak Fe^{3+} peaks at 377, 388 and 450 are present, as well as a characteristic Cr^{3+} absorption band at 560 nm. No $\text{Fe}^{2+}/\text{Ti}^{4+}$ intervalence charge transfer features are observed at this spectrum. The sample presents full absorption ("cut off") at around 330 nm. No shoulder between 300 and 350 nm is visible.

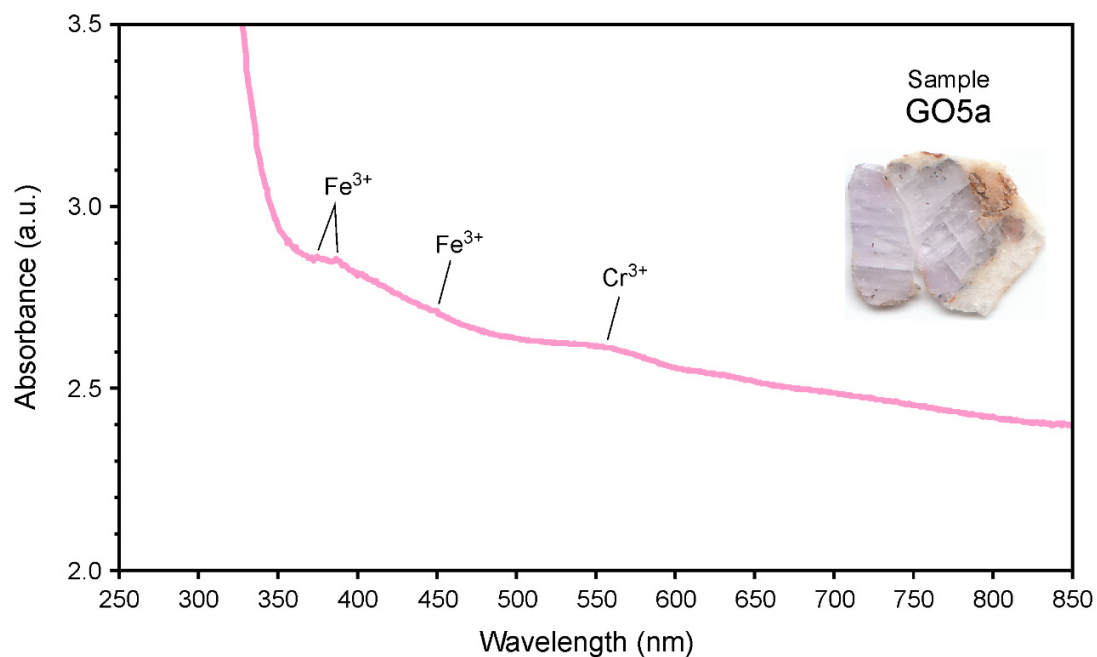


Fig.3.3.6. UV-Vis-NIR absorption spectra of GO5 light pink sapphire from Xanthi.

Both Drama samples (Fig. 3.3.7, 3.3.8) show characteristic Cr^{3+} absorption bands at 405 and 560 nm, as well as a weak peak, related also to Cr^{3+} , at 694 nm. The 377, 388 and 450 peaks attributed to the presence of Fe^{3+} are also present. No $\text{Fe}^{2+}/\text{Ti}^{4+}$ intervalence charge transfer features are observed in both samples. DR1 and PAR, both show a very weak shoulder at around 340 nm. The "cut off" for sample DR1 is located around 310 nm, while for sample PAR at around 320 nm.

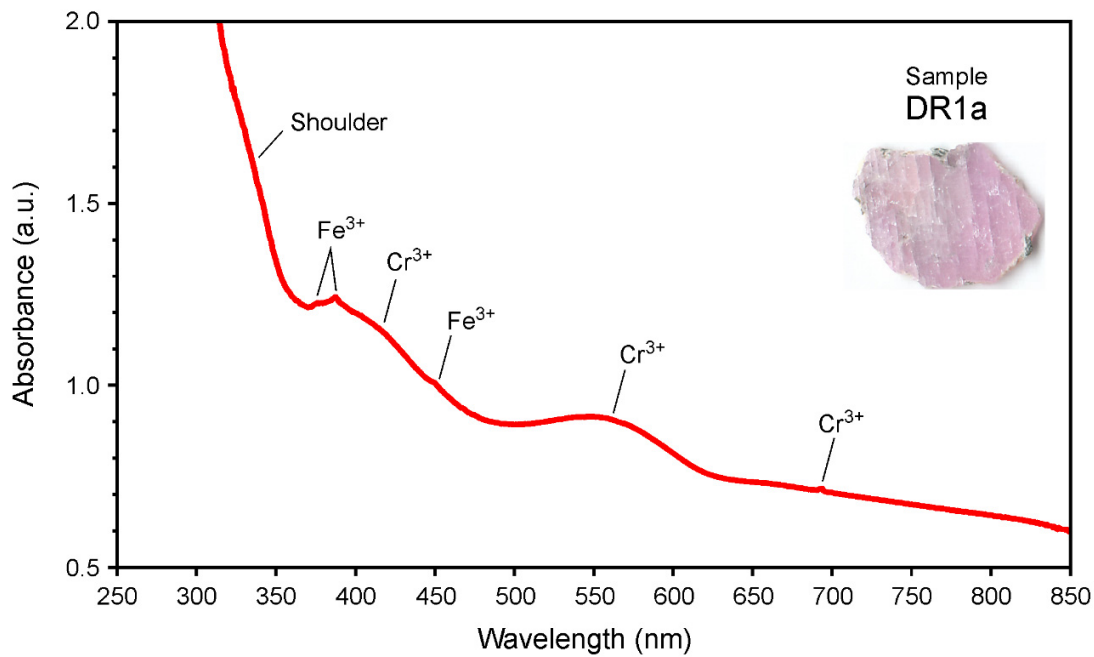


Fig. 3.3.7. UV-Vis-NIR absorption spectra of DR1 ruby from Drama.

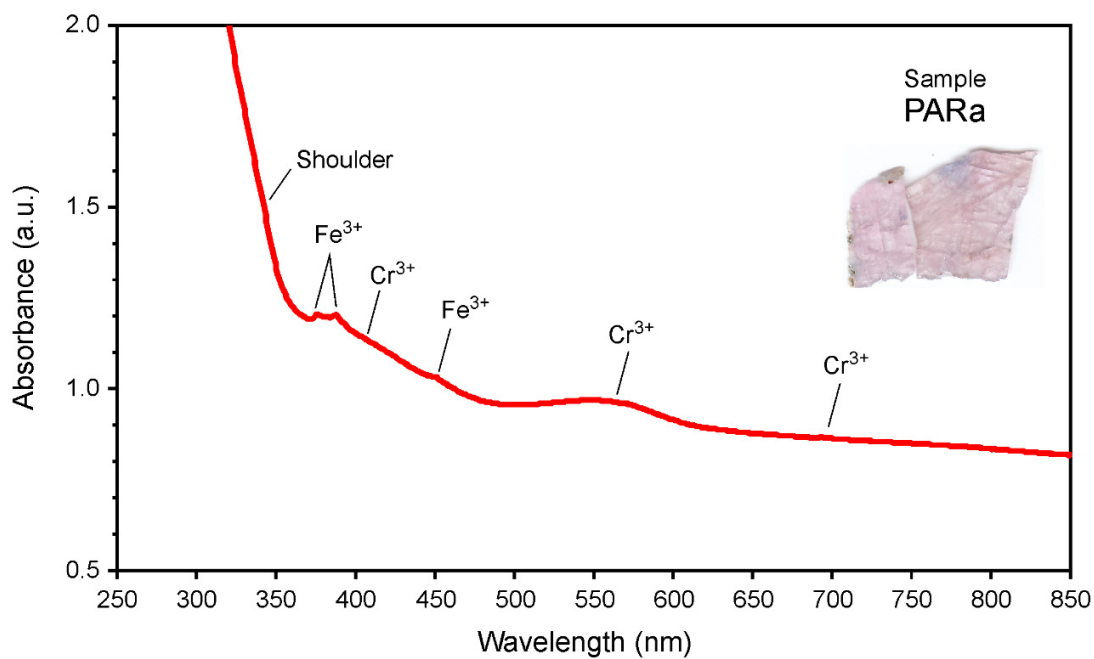


Fig.3.3.8. UV-Vis-NIR absorption spectra of PAR ruby from Drama.

Table 3.4.1 presents the percentages of titanium, chromium, iron, vanadium and gallium oxides measured in all corundum samples. Vanadium is below detection limit in all samples. Chromium is present only in rubies from Drama, Ikaria's sapphires and GO5 from Xanthi.

Naxos' sapphires present high titanium and iron values reaching up to 0.6065 wt% titanium and 0.7216 wt% iron. NX1 presents the highest average titanium content of all studied samples. In samples NX2 and NX4 the average titanium content is low, with the exemption of a measurement giving a value of 0.1030 wt%, probably attributed to rutile inclusions. Rutile needles are possibly the reason for the strong titanium measurements in sample NX1. Samples NX2 and NX4 present higher iron values than sample NX1, which explain their stronger blue color in comparison to sample NX1. The gallium content of Naxos' samples lies between 0.0073 and 0.0117 wt%.

Ikaria's sample shows an average titanium value of 0.1891 wt% reaching a maximum of 0.2138 wt% and a high iron content ranging from 0.4464 to 0.6561 wt%, which is verified by the strong blue color of this sample. The presence of biotite in the host rock may have affected the iron measurements in corundum. Gallium exhibits an average value of 0.0103 wt% in Ikaria's sapphires, being the highest average value of all examined samples. Chromium content lies between 0.4464 and 0.6561 wt%.

The titanium values in Xanthi's sapphires show a large variation, ranging from 0.0144 to 0.6030 wt%. All measurements from sample GO5 show low titanium content; only one spot shows an unusually high value of 0.6030 wt%, probably attributed to rutile inclusions. The iron content in this sample ranges between 0.0128 and 0.1785 wt%, giving high values for certain measurements possibly due to allanite inclusions. Chromium content is low with an average value of 0.0110 wt%, justifying the weak pink color of sample GO5 in opposition to colorless sample GOR in which chromium content is below detection limit. GOR sample has titanium values going from 0.0449 to 0.1099 wt% and iron content ranging from 0.1015 to 1.4414 wt%. The measurements with high titanium values coincide with the ones with high iron content, which is probably related to certain mineral inclusions. Gallium content is low in both samples with values lying at 0.0037 to 0.0130 wt% and 0.0130 wt% being the highest gallium value in all studied samples. Apart from two measurements in sample GOR showing high iron content, Xanthi's samples exhibit lower iron content than Drama's, Ikaria's and Naxos' samples.

Table 3.4.1. EDXRF analyses of trace and minor elements in sapphires (in weight %) from Naxos, Ikaria, Xanthi and Drama regions.

Region	Sample	Content wt%				
		TiO ₂	Cr ₂ O ₃	Fe ₂ O ₃	V ₂ O ₃	GaO
Naxos	NX1	0.3713	-	0.3288	-	0.0077
		0.6065	-	0.3277	-	0.0094
		0.4614	-	0.3230	-	0.0084
		0.3817	-	0.3470	-	0.0092
		0.3816	-	0.3356	-	0.0080
		0.2263	-	0.3943	-	0.0074
	NX2	0.0202	-	0.5567	-	0.0108
		0.1030	-	0.6028	-	0.0077
		0.0471	-	0.6365	-	0.0073
		0.0000	-	0.4996	-	0.0089
	NX4	0.0000	-	0.5094	-	0.0075
		0.0580	-	0.5980	-	0.0078
		0.0974	-	0.7216	-	0.0117
Ikaria	IK1	0.1696	0.0453	0.4464	-	0.0093
		0.1787	0.0357	0.4953	-	0.0112
		0.2138	0.0242	0.6561	-	0.0106
Xanthi	GOR	0.0449	-	0.1210	-	0.0037
		0.0662	-	0.1015	-	0.0042
		0.1099	-	0.9721	-	0.0043
		0.1020	-	1.4414	-	0.0040
	GO5	0.0522	0.0000	0.1503	-	0.0103
		0.0421	0.0000	0.1785	-	0.0130
		0.6030	0.0311	0.1449	-	0.0085
		0.0144	0.0255	0.1404	-	0.0099
		0.0224	0.0000	0.0340	-	0.0051
		0.0261	0.0000	0.0128	-	0.0085
Drama	DR	0.0131	0.1107	0.3058	-	0.0031
		0.0052	0.1173	0.3049	-	0.0034
	PAR	0.0709	0.0639	0.4192	-	0.0028
		0.0414	0.0598	0.4509	-	0.0029
		0.0686	0.0685	0.3883	-	0.0036
		0.0206	0.1213	0.5461	-	0.0038

Drama's rubies have a high chromium content ranging between 0.0598 and 0.1213 wt%, with sample DR1 reaching an average value of 0.1140 wt%. The high chromium values in these samples justify their pink color. The samples are poor in titanium with average values of 0.0092 wt% for sample DR1 and 0.0488 wt% for sample PAR, but rich in iron with values ranging from 0.3049 to 0.5461 wt%. Gallium content is low with an average value of 0.0033 wt%.

3.5. FLUID INCLUSIONS

The fluid inclusions in the studied corundums (Figs. 3.5.1, 3.5.2) range in size between $<1\ \mu\text{m}$ and $55\ \mu\text{m}$. One main type of fluid inclusions (Type 1) was observed: monophasic CO_2 vapor or liquid fluid inclusions, and hence too dark to see other phase in the inclusions (Fig. 3.5.1a, 3.5.2a-d). They often have an elongated negative crystal shape of the host corundum (Fig. 3.5.1e, 3.5.2a). They occur as isolated and based on their similarity in shape and the mode of occurrence they are considered as primary fluid inclusions (Fig. 3.5.1d, e, 3.5.2a, c, f). However, the most significant criterion to identify primary fluid inclusions is when they occur along the growth zones of the corundum (Fig. 3.5.1c), based on the criteria suggested by Bodnar (2003).

Oriented clusters of monophasic CO_2 vapor or liquid fluid inclusions along planes are very common in the studied samples and are related to micro-cracks and subsequent fractures healed during crystal growth, and therefore are considered as pseudosecondary (Fig. 3.5.1a, f, 3.5.2b). Numerous tiny fluid inclusions along trails are usually observed, but due to their small size no phases can be identified (Fig. 3.5.2e). They are considered as secondary fluid inclusions. The majority of the fluid inclusions appears stretched and necked or empty due to leaking phenomena (Fig. 3.5.1b, 3.5.2a, d). Microthermometric results were based on primary and pseudosecondary inclusions, without necking down and leaking phenomena. However, many measurements were unsuccessful due to the black color of the carbonic monophasic fluid in the inclusions and the difficulty to observe phase changes.

The temperatures of first melting (T_m) range between -57.3° and -56.6°C , at the triple point of CO_2 ($T=-56.6^\circ\text{C}$) and slightly lower, indicating that the fluid is dominated mainly by CO_2 with very small quantities of CH_4 and/or N_2 . Temperatures of T_m were not possible to be obtained in the sample PAR1a from Paranesti (Drama) because all the heating runs caused violent exploding of the fluid inclusions at -56.6°C , on the critical temperature of CO_2 , breaking

the protecting glass of the heating/freezing stage. We suggest that this happened because fluid from the majority of the inclusions leaked and the inclusions became unstable after melting of ice CO₂ at T=-56.6° C.

Clathrate nucleation was not observed in any measured fluid inclusion, demonstrating that liquid water (H₂O) was not incorporated in the whole process of the corundums formation. All fluid inclusions homogenized to the liquid phase at temperatures (Th) varying from 27.3° to 31.0°C. This Th is close to the critical temperature of pure CO₂ and corresponds to relatively low densities of the source fluids, which vary from 0.46 to 0.67 g/cm³. Figure 3.5.3 shows histograms of the Th carbonic fluid inclusions from the four different studied corundum occurrences in Greece (Paranesti, Gorgona, Naxos, Ikaria).

Table 3.5.1 presents the microthermometric data of all studied fluid inclusions from Drama, Xanthi, Ikaria and Naxos.

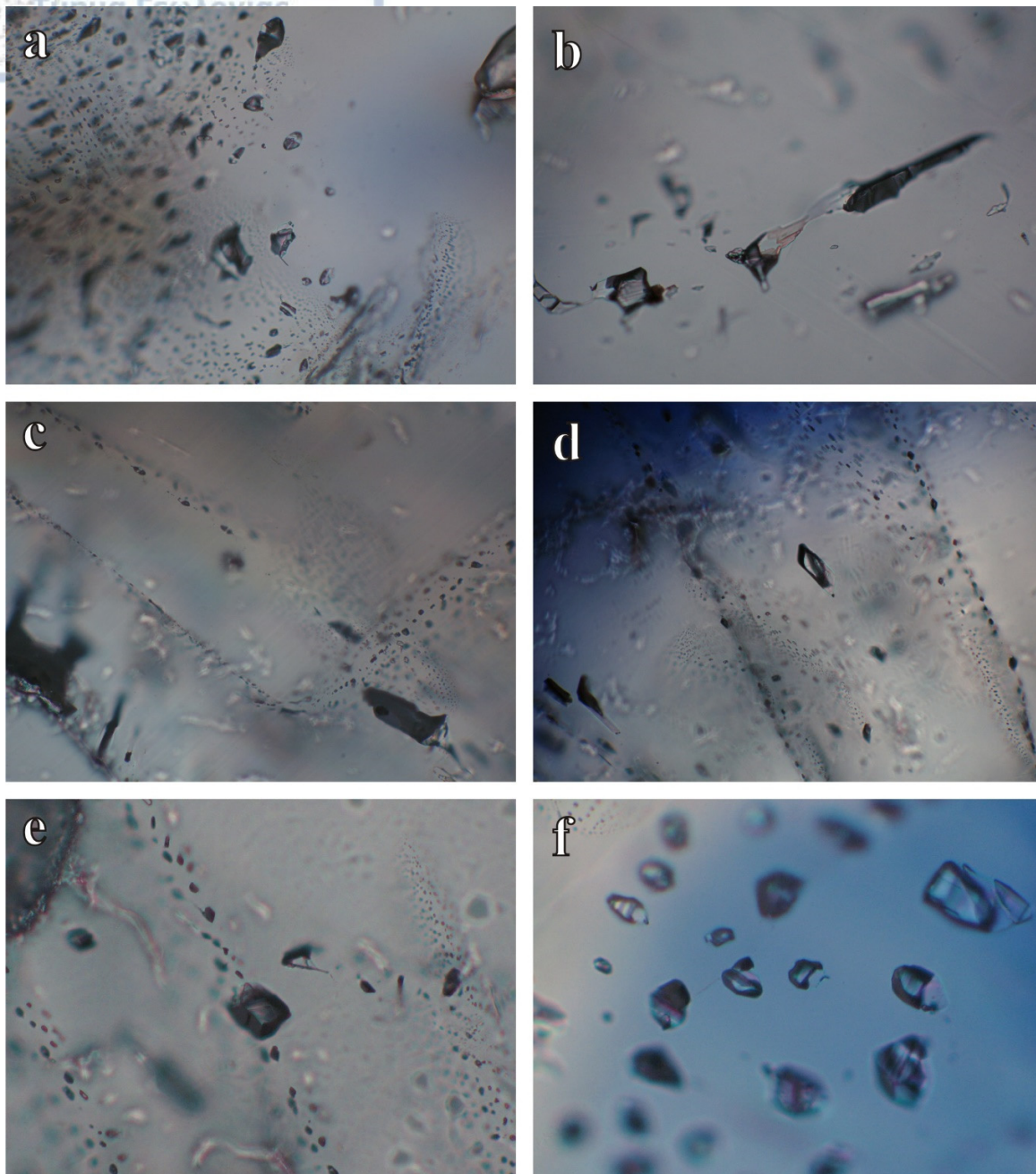


Fig. 3.5.1. Photomicrographs of fluid inclusions in sapphires from the Attic-Cycladic massif of Greece, Naxos island. (a) Oriented cluster of pseudosecondary carbonic fluid inclusions along fractures healed during crystal growth (thin-section, NX1a). (b) Isolated primary type 1 inclusion containing a liquid carbonic phase with necking deformation (thin-section, NX1a). (c) Fluid inclusions along growth zones of the corundum (thin-section, NX1a). (d, e) Type 1 primary fluid inclusions containing a carbonic liquid phase (thin-section, NX2a). (f) Pseudosecondary type 1 carbonic fluid inclusions along a fracture healed during crystal growth (thin-section, NX2b).

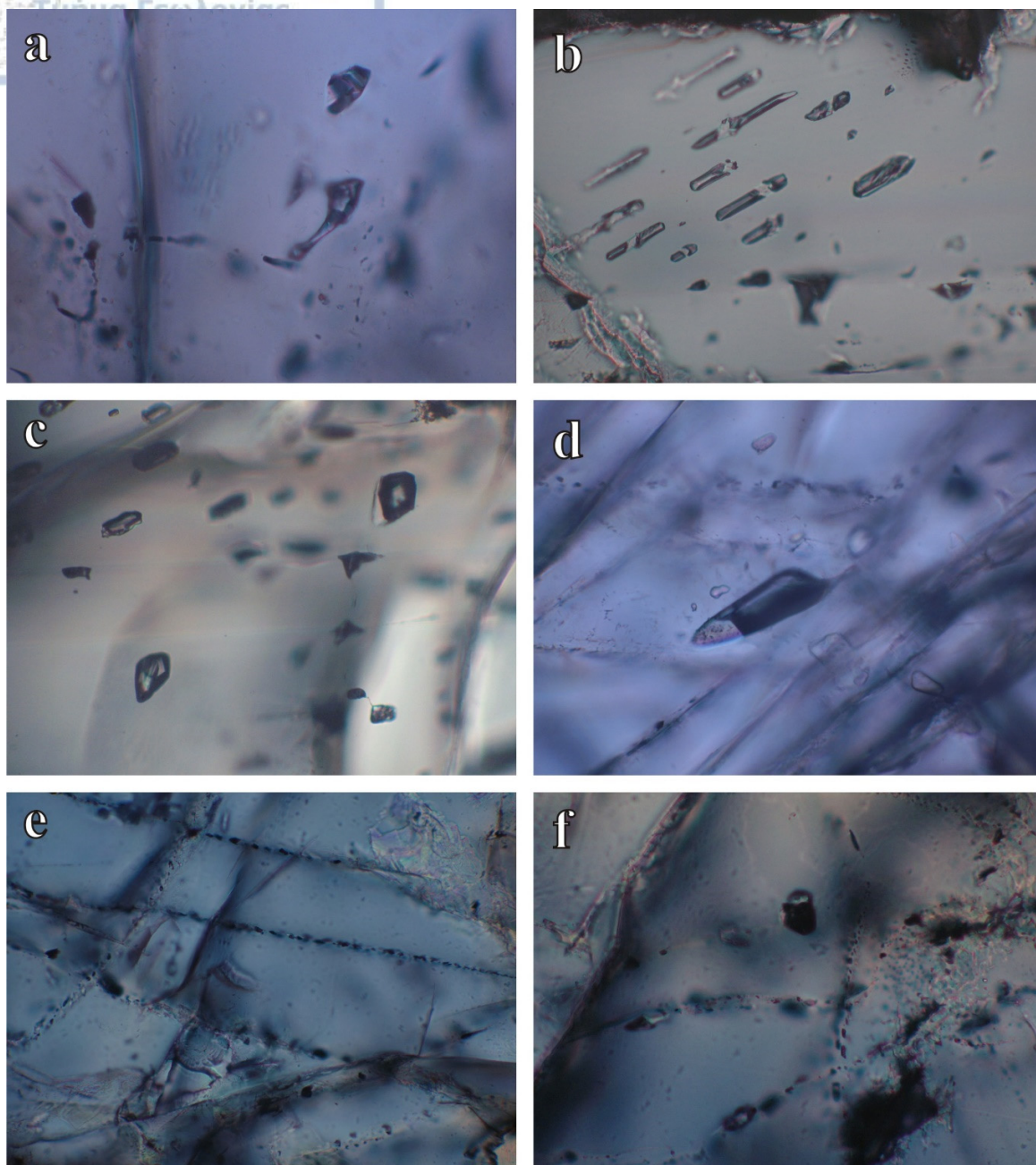


Fig. 3.5.2. Photomicrographs of fluid inclusions in corundums from the Rhodope massif of Greece, Paranesti and Gorgona. (a) Isolated primary type 1 inclusions containing a liquid phase composed of $\text{CO}_2 \pm (\text{CH}_4 \text{ and/or } \text{N}_2)$. The inclusion at the upper part has a negative crystal shape, and the inclusion underneath shows necking deformation (Drama, thin-section PARb). (b) Pseudosecondary type 1 carbonic fluid inclusions along a fracture healed during crystal growth (Xanthi, thin-section GO5a). (c) Type 1 primary fluid inclusion containing a carbonic liquid phase (Xanthi, thin-section GO5a). (d) Type 1 inclusion which shows leaking phenomena (Xanthi, thin-section GO5b). (e) Tiny fluid inclusions along fracture planes trails, but due to their small size no phases can be identified (Xanthi, thin-section GORb). (f) Isolated type 1 inclusion containing a carbonic liquid phase (Xanthi, thin-section GORb).

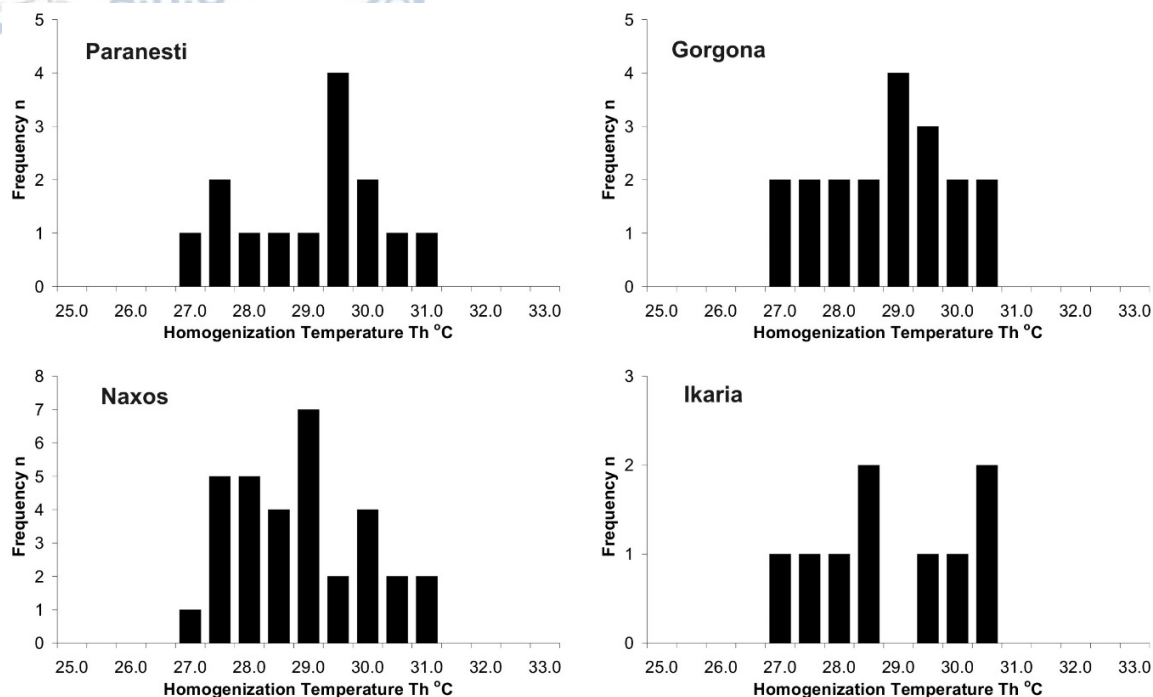


Fig. 3.5.3. Histograms of homogenization temperatures of the CO₂ phase in the fluid inclusion from the Rhodope massif (Paranesti, Gorgona) and the Attic-Cycladic massif (Naxos, Ikaria) from Greece.

Table 3.5.1. Microthermometric data of studied fluid inclusions from corundums in Greece.

Sample	Geotectonic Zone	Region	Type of fluid inclusions	n	Tm CO ₂	Th CO ₂	Densities g/cm ³	Chemical composition of the fluid
NX1a	Attico-Cycladic Massif	Naxos	Type 1	8	-57.2 to -56.6	27.3-31.0	0.51-0.67	CO ₂ ± (CH ₄ and/or N ₂)
NX1b			Type 1	10	-57.3 to -56.7	28.1-30.5	0.57-0.65	CO ₂ ± (CH ₄ and/or N ₂)
NX2a			Type 1	4	-57.2 to -56.6	27.9-29.3	0.62-0.66	CO ₂ ± (CH ₄ and/or N ₂)
NX2b			Type 1	6	-57.1 to -56.8	28.9-31.0	0.51-0.63	CO ₂ ± (CH ₄ and/or N ₂)
NX4b			Type 1	4	-57.2 to -56.9	27.5-30.4	0.57-0.67	CO ₂ ± (CH ₄ and/or N ₂)
IK1a		Ikaria	Type 1	3	-56.9 to -56.6	30.1-30.8	0.54-0.59	CO ₂ ± (CH ₄ and/or N ₂)
IK1b			Type 1	6	-57.0 to -56.6	27.4-28.3	0.65-0.67	CO ₂ ± (CH ₄ and/or N ₂)
GORa	Rhodope Massif		Type 1	4	-57.0 to -56.8	29.2-30.2	0.58-0.62	CO ₂ ± (CH ₄ and/or N ₂)
GORb			Type 1	3	-56.7 to -56.6	27.8-30.5	0.57-0.66	CO ₂ ± (CH ₄ and/or N ₂)
GO5a		Xanthi	Type 1	6	-57.2 to -56.8	28.2-30.9	0.53-0.65	CO ₂ ± (CH ₄ and/or N ₂)
GO5b			Type 1	6	-57.2 to -56.7	27.4-29.2	0.62-0.67	CO ₂ ± (CH ₄ and/or N ₂)
DR1a		Drama	Type 1	7	-57.2 to -56.7	28.7-31.1	0.46-0.64	CO ₂ ± (CH ₄ and/or N ₂)
PARa			Type 1	-	Exploding at -56.6	-	-	-
PARb			Type 1	7	-57.1 to -56.6	27.4-30.4	0.57-0.67	CO ₂ ± (CH ₄ and/or N ₂)



CHAPTER 4. DISCUSSION AND CONCLUSIONS

4.1. PETROLOGY

Table 4.1.1 presents an overview of the characteristic features that all studied samples exhibit under the polar microscope.

Table 4.1.1. Characteristic features of all studied samples observed under polarizing microscope.

Region	Sample	Pleochroism	Polysynthetic twinning	Parting	Color zoning	Fractures	Fluid inclusions
Naxos	NX1	-	+	-	+	+	+
	NX2	-	+	+	+	+	+
	NX4	-	+	+	+	+	+
Ikaria	IK1	-	-	+	+	+	+
Xanthi	GOR	+	+	+	+	+	+
	GO5	-	+	+	+	+	+
Drama	DR1	-	-	+	+	+	+
	PAR	-	+	+	+	+	+

The phenomenon of color zoning is prominent in all samples in the form of: a) a blue core surrounded by a white rim, b) a blue-zoned outer rim surrounding a colorless core, or c) blue and white spots distributed irregularly in the crystal. The presence of fluid inclusions is also clear in all samples (see chapter 4.5). Apart from Ikaria's IK1 and Drama's DR1, all the other samples present polysynthetic twinning under crossed nicols. Under parallel nicols, only Xanthi's sample GOR presents pleochroism. However, since

all corundum crystals tend to be pleochroic when colored, we conclude that the observation of pleochroism only in sample GOR, is due to the thin-section's orientation. Partings are observed in all samples, except in Naxos' NX1. Finally, all the studied corundums are highly fractured and brecciated, indicating high deformational conditions taking place after the crystallization of corundum which decreased the gem quality of the samples.

Due to the thickness of thin-sections, as well as the absence of host-rocks in the examined samples, only an approximate identification of the mineral assemblages was possible. Table 4.1.2 displays the more easily recognizable minerals under the polar microscope.

Table 4.1.2. Mineral assemblages in all studied samples under the polar microscope.

Region	Sample	Biotite	White Micas	Chlorite	Kyanite	Zircon	Allanite	Rutile (?)	Opaque minerals
Naxos	NX1	+	-	-	-	+	-	-	+
	NX2	+	-	-	-	-	-	+	-
	NX4	+	-	+	-	-	-	-	-
Ikaria	IK1	+	+	+	-	-	-	-	+
Xanthi	GOR	-	-	-	+	-	-	-	+
	GO5	-	-	-	-	-	+	-	+
Drama	DR1	-	-	+	-	-	-	-	-
	PAR	-	-	-	-	-	-	-	-

A biotite-like mineral was observable in Naxos's samples. However, the literature references for Naxos' sapphires record the presence of phlogopite. Since the two minerals have a similar image under the polar microscope, the distinction between the two was not possible. Chlorite and zircon were also identified in Naxos' samples, as were rutile-like inclusions forming needles within corundum; though not recorded in the OH absorption spectra of these samples. An opaque mineral was present in sample NX1, but it was not possible to be identified. Ikaria's samples were characterized by the presence of biotite, white mica (probably margarite according to literature, see chapter 1.6.2), chlorite and an unidentified opaque mineral. The type of Ikaria's deposit (corundum in metabauxites

hosted in Ca marbles) and the literature references for the presence of margarite, hematite-ilmenite and Fe-chlorite, accord with the microscopic observations of this thesis. The presence of kyanite in Xanthi's sample GOR complies with the geology of the wider Gorgona area of corundum-bearing marbles hosted in eclogitic amphibolites and Ky-eclogites (see chapter 1.6.1). An allanite inclusion was recognised in the sample GO5, as were traces of an opaque mineral in both Xanthi's samples. The thin-sections of samples DR1 and PAR from Drama were sole corundum crystals and hence, no minerals were recognized apart from a trace of chlorite-inclusion in the sample DR1.

4.2. FTIR

Table 4.2.1 summarizes the OH absorption bands obtained with FTIR spectroscopy in all studied samples.

Table 4.2.1. OH absorption peaks, related to mineral and fluid inclusions, obtained with FTIR spectroscopy from all studied samples.

Region	Sample	Boehmite	Diaspore	Goethite	Chlorite	Calcite	CO ₂ in fluid inclusions
Naxos	NX1	+	-	-	-	-	+
	NX2	+	-	+	+	-	+
	NX4	+	-	+	-	-	+
Ikaria	IK1	+	+	-	+	-	+
Xanthi	GOR	+	+	-	-	+	+
	GO5	+	+	-	-	+	+
Drama	DR1	+	+	-	+	-	+
	PAR	+	+	-	+	-	+

The main similarity in their spectra of all studied samples is the presence of OH absorption bands related to boehmite inclusions. Diaspore related peaks are prominent in all spectra, apart from the ones of Naxos' samples. Another similar and important feature in all samples is the presence of the CO₂ peak. The shoulder of this peak is characteristic of the CO₂ from fluid inclusions and not from the atmosphere. Figures 4.2.1 and 4.2.2

illustrate the CO₂-fluid inclusions related peaks for all the blue samples (Naxos, Ikaria and Xanthi) and all the pink to red samples (Xanthi and Drama).

Blue samples

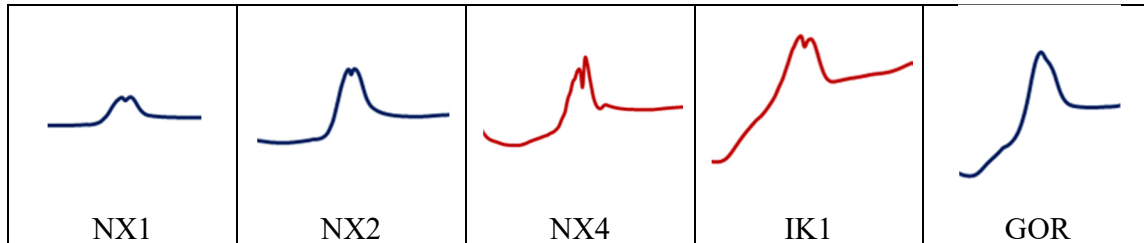


Fig. 4.2.1. Absorption peaks, related to CO₂ from fluid inclusions from blue samples from Naxos (NX1, NX2, NX4), Ikaria (IK1) and Xanthi (GOR).

Pink-Red samples

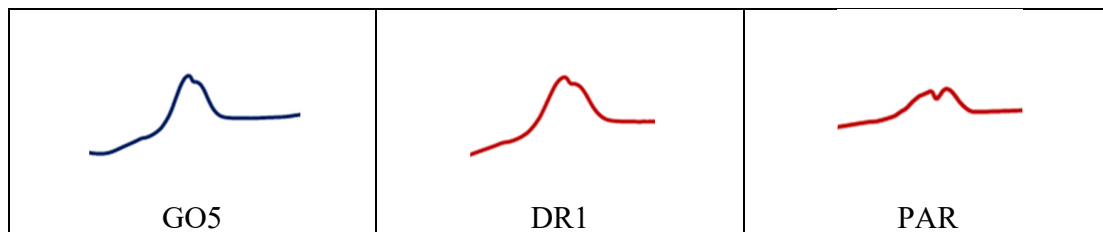


Fig. 4.2.2. Absorption peaks, related to CO₂ from fluid inclusions from pink to red samples from Xanthi (GO5) and Drama (DR1, PAR).

Blue samples: IK1 and GOR present diasporite related OH absorption peaks. A calcite related peak is discernible in sample GOR. Ikaria's samples also present a chlorite related OH peak, as does sample NX2 from Naxos. Samples NX2 and NX4 show goethite related OH peaks, which are absent from any other studied sample. IK1 and GOR show the strongest OH absorption bands, while Naxos' samples the weakest. Since IK1 and GOR seem to be the most fractured samples, we can conclude that: a) the presence of OH peaks in the spectra is due to epigenetic inclusions and b) there is a correlation between the intensity of absorption and the intensity of the deformation that the examined samples have undergone.

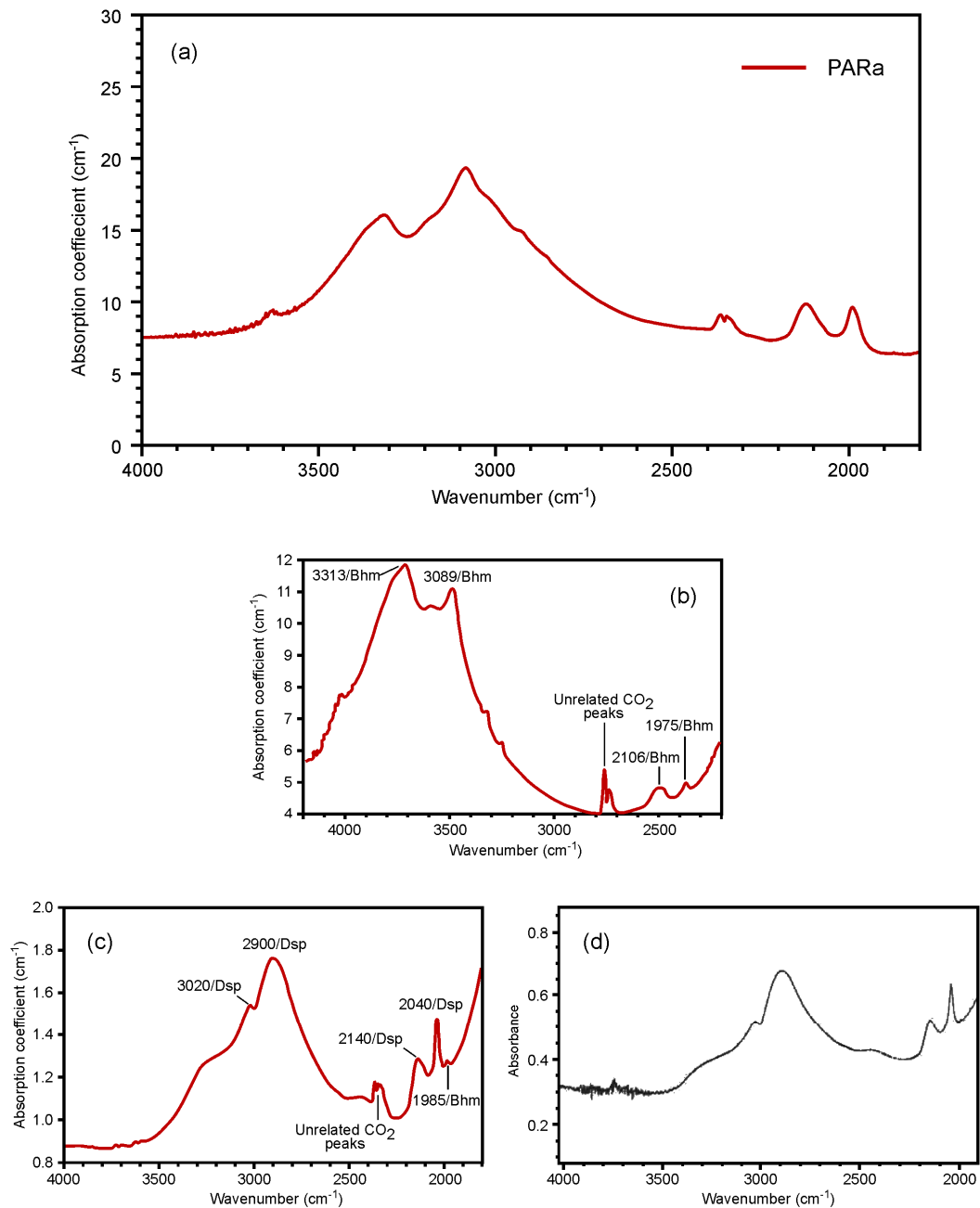


Fig. 4.2.3. Comparison of the morphology of a) a diaspore-boehmite related OH spectrum Drama's PAr ruby, b) a boehmite related OH spectrum of an untreated ruby from Montepuez (Mozambique; Emmett et al. 2017), c) a diaspore related OH spectrum of an untreated Myanmar ruby (Emmett et al., 2017) and d) a diaspore related OH spectrum of a Mong Hsu ruby (Myanmar; Smith, 1995). PAR presents the maximum OH peaks related to boehmite and presented in Mozambique ruby too, but the second peak being weaker in opposition to spectrum a.

Pink to red samples: The spectra of GO5 from Xanthi and DR1 and PAR from Drama present more or less the same features. Boehmite and diaspore related OH peaks are visible in all three samples, while goethite related peaks are absent and a weak and hardly noticeable peak in GO5 is probably related to calcite. Both DR1 and PAR from Drama show a small chlorite related OH peak. The spectra of all three samples are similar to the spectrum of a non-heat-treated natural Mon Hsu ruby proposed by Karampelas and Kiefert (2012) (see chapter 2, Fig. 2.3.2.5). PAR's maximum peaks are quite narrow in comparison with the rest of the samples. Figure 4.2.3 shows a correlation between the spectrum of sample PAR (d) and the ones of an untreated ruby from Montepuez (a) (Mozambique; Emmett et al., 2017), an untreated Myanmar ruby (b) (Emmett et al., 2017) and a Mong Hsu ruby (c) (Myanmar; Smith, 1995). The spectrum of Mozambique ruby (a) is related to the presence of boehmite, while the spectra of Myanmar rubies (b and c) to the presence of diaspore. While the maximum peaks in the spectrum of sample PAR (d) are related to boehmite (a weaker absorption related to diaspore is also visible in the main band), the morphology of its spectrum resembles the morphology of the spectra of Myanmar rubies (b and c), which are related to diaspore, and not so much the morphology of boehmite related spectrum of the Mozambique ruby (a).

4.3. UV-Vis-NIR

Table 4.3.1 summarizes the main features obtained by the UV-Vis-NIR spectra of all studied samples. The absence of an iron related absorption with a maximum above 700 nm (from the red to the near infrared region) from all spectra, indicates a non-basaltic origin for all studied samples (blue and pink-red).

Blue samples: Apart from NX1, all the rest (NX2, NX4, IK1 and GOR) present a shoulder at around 330 to 340 nm. Despite the fact that this shoulder is of debatable origin, its presence denotes the metamorphic origin of the samples. Hence, samples NX2, NX4, IK1 and GOR can be characterized as metamorphic or "Burma-type" deposits. The shoulder is absent from sample NX1, thus indicating its possible metasomatic ("Kashmir-type") origin (see chapter 3, Fig. 2.3.3.2). Sample NX1 shows a complete absorption

("cut off") around 330 nm, while the "cut off" for the rest is situated below 330 nm.

Samples NX2, NX4, IK1 and GOR present weak Fe^{3+} absorption peaks and a strong absorption band related to Fe^{2+} - Ti^{4+} intervalence charge transfer, another indicator of a metamorphic origin (see chapter 2, Fig. 2.3.3.3). The strong absorption at this region of the spectrum (green-yellow) is the cause of the blue color of these samples. The spectra of IK1 presents a similarity with the spectra of a metamorphic light blue sapphire from Mogok (Myanmar) proposed by Elmaleh (2014) (Fig. 4.3.1). Both spectra present the Fe^{3+} peaks at 377, 388 and 450 nm (though in sample IK1 the peaks are weaker) and the strong $\text{Fe}^{2+}/\text{Ti}^{4+}$ band at 570 nm. Sample NX1 presents weak absorptions at the ultraviolet region of the spectrum (weak Fe^{3+} peaks at 377 and 388 nm), and even weaker absorptions at the violet-blue (Fe^{3+} peak at 450 nm) and the green-yellow region (Fe^{2+} - Ti^{4+} peak at 570 nm), showing again a possible metasomatic character (Smith, 2010; see chapter 2; Fig. 2.3.3.4).

Table 4.3.1. OH absorption peaks, related to mineral and fluid inclusions, obtained with FTIR spectroscopy from all studied samples.

Region	Sample	Shoulder around 300 nm	Full absorption "cut off"	377 Fe^{3+}	388 Fe^{3+}	450 Fe^{3+}	570 Fe^{2+} - Ti^{4+}	405 Cr^{3+}	560 Cr^{3+}	694 Cr^{3+}
Naxos	NX1	-	330	weak	weak	weak	weak	-	-	-
	NX2	+	300	weak	weak	-	strong	-	-	-
	NX4	+	320	weak	weak	weak	strong	-	-	-
Ikaria	IK1	+	300	weak	weak	weak	strong	-	-	-
Xanthi	GOR	+	320	weak	weak	-	strong	-	-	-
	GO5	-	330	weak	weak	weak	weak	-	weak	-
Drama	DR1	+	310	weak	weak	weak	-	strong	strong	weak
	PAR	+	320	weak	weak	weak	-	strong	strong	weak

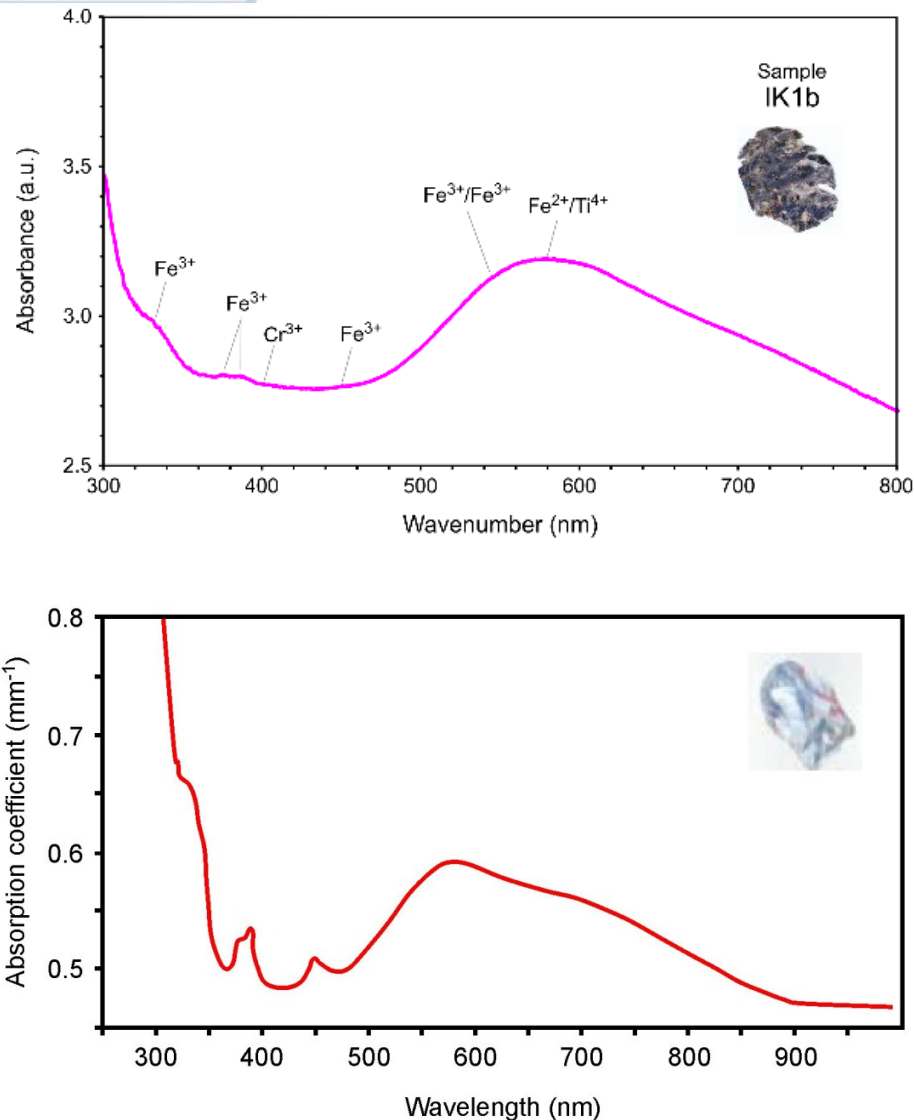


Fig. 4.3.1. Absorption spectra of sample IK1 from Ikaria (top) in comparison to the absorption spectra of blue sapphire from Mogok (bottom; modified after Elmaleh, 2014).

Pink-red samples: Sample GO5 presents no shoulder at around 300 nm, while samples DR1 and PAR present a very weak and hardly visible shoulder at around 340 nm. Since the color of these samples is ranging from light pink to red, the presence or absence of the “300” shoulder is not a strong indicator of their origin. GO5 shows a complete absorption at around 330 nm, while DR1 and PAR at around 310 and 320 nm respectively. GO5 presents very weak absorption at the ultraviolet (Fe^{3+} peaks at 377 and 388 nm), violet-blue (Fe^{3+} peak at 450 nm) and green-yellow (Cr^{3+} peak at 560 and Fe^{2+} -

Ti⁴⁺ peak at 570 nm) region of the spectrum. DR1 and PAR present weak Fe³⁺ peaks at 377, 388 and 450 nm and strong Cr³⁺ peaks at 405 and 560 nm. An additional weak Cr³⁺ peak at 694 nm is visible in both samples. The strong absorption at the violet and green region (Cr³⁺ peaks at 405 and 560 nm, respectively), in combination to the weak Fe³⁺ peaks and the absence of Fe²⁺-Ti⁴⁺ intervalence charge transfer, may be the cause for the pink to red color of these samples.

4.4. EDXRF

Different trace element correlation diagrams are presented below to present and compare all studied samples. The different color of the symbols used in the diagrams, represents the color of each sample (red, pink and blue), while the shape represents the region of the occurrence (triangle for Naxos, rhombus for Ikaria, circle for Xanthi and square for Drama). For instance, pink circles represent Xanthi's sample GO5 (pink to colorless corundum) and blue circles Xanthi's sample GOR (blue corundum). In literature, different diagrams are used usually for the plotting of sapphires and rubies. However, none of the studied samples can be characterized as a ruby in the true sense of the word (though pink to red samples are referred as rubies in this thesis for a better discrimination); hence, all studied samples are plotted together in the diagrams.

In the Fe₂O₃ versus TiO₂ diagram (Fig. 4.4.1) values from Drama, Ikaria and Naxos plot within a small field in relation to Fe₂O₃ content, while Xanthi's values are scattered presenting a great variation in the Y axis. In the X axis the discrimination between Drama's and Naxos' TiO₂ values (apart from one Drama's sample overlapping to a Naxos' one) is clear; Drama's highest TiO₂ values plot at the same area with Naxos' lowest values.

In the Fe₂O₃ versus Ga₂O₃ diagram (Fig. 4.4.2), Ikaria's values overlap with Naxos' values, while Drama's samples present the lowest Ga₂O₃ content together with sample GO5 from Xanthi. A correlation can be made between the Ga₂O₃ content of the samples and their color, since pink to red samples seem to present lower values of Ga₂O₃ than blue samples. Xanthi's values are scattered, showing a large variation and divergence compared to the rest of the samples.

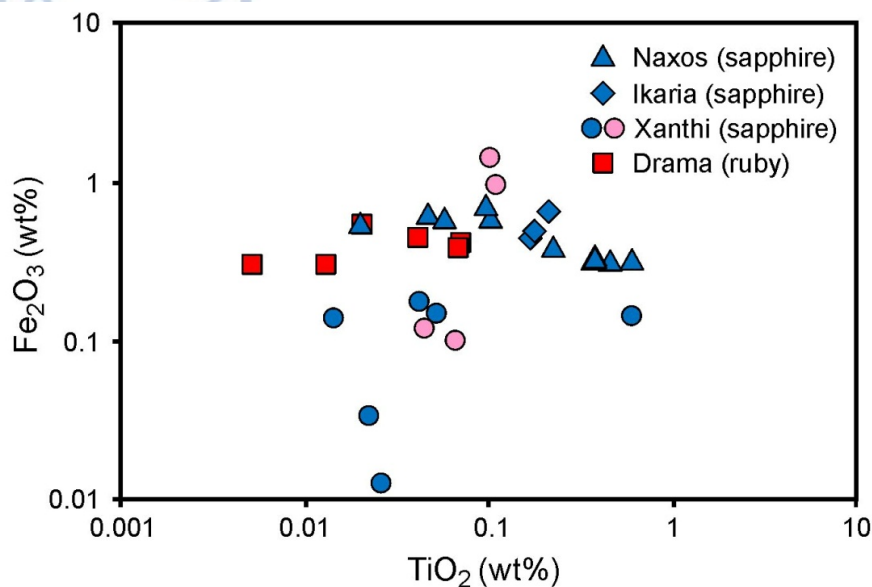


Fig. 4.4.1. Diagram Fe_2O_3 wt% function of TiO_2 wt% for sapphires from Drama, Xanthi, Ikaria and Naxos.

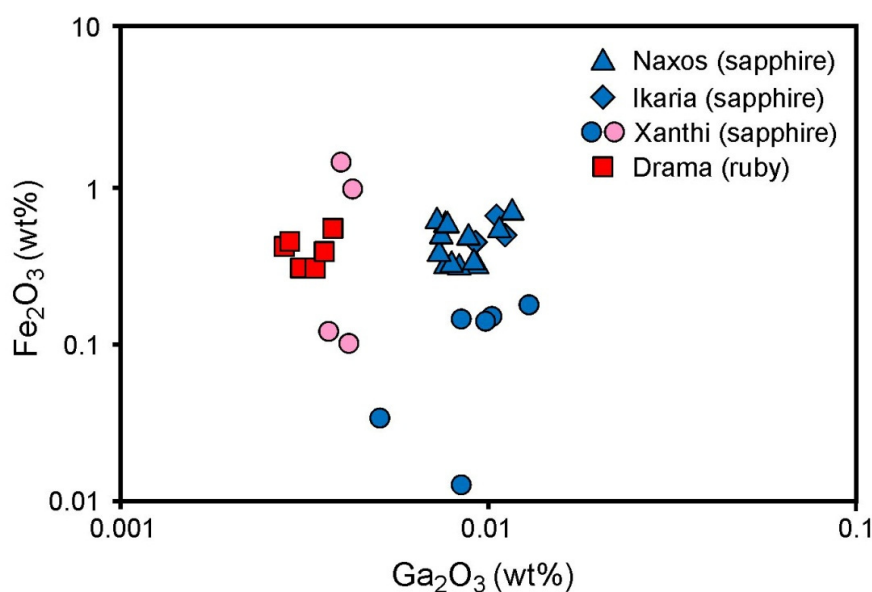


Fig. 4.4.2. Diagram Fe_2O_3 wt% function of Ga_2O_3 wt% for sapphires from Drama, Xanthi, Ikaria and Naxos.

Applying the $\text{TiO}_2/\text{Ga}_2\text{O}_3$ versus $\text{Fe}_2\text{O}_3/\text{Cr}_2\text{O}_3$ and $\text{Cr}_2\text{O}_3/\text{Ga}_2\text{O}_3$ versus $\text{Fe}_2\text{O}_3/\text{TiO}_2$ diagrams (Fig. 4.4.3a, b), modified after Schwarz et al. (2000), to all studied samples (blue and pink to red), it is visible that: a) the samples with absence of chromium (NX1, NX2, NX4 and GOR) cannot plot in these two diagrams, b) all samples present a large variation in $\text{TiO}_2/\text{Ga}_2\text{O}_3$, $\text{Fe}_2\text{O}_3/\text{Cr}_2\text{O}_3$, $\text{Cr}_2\text{O}_3/\text{Ga}_2\text{O}_3$ and $\text{Fe}_2\text{O}_3/\text{TiO}_2$ ratios and c) all

studied samples diverge from the skarn-related and basaltic fields showing no similarity with the deposits from Andranondambo and Ambondromifehy, respectively. Even for Ikaria's samples, which would be expected to plot within the field of skarn-related deposits, the deviation from this field is obvious.

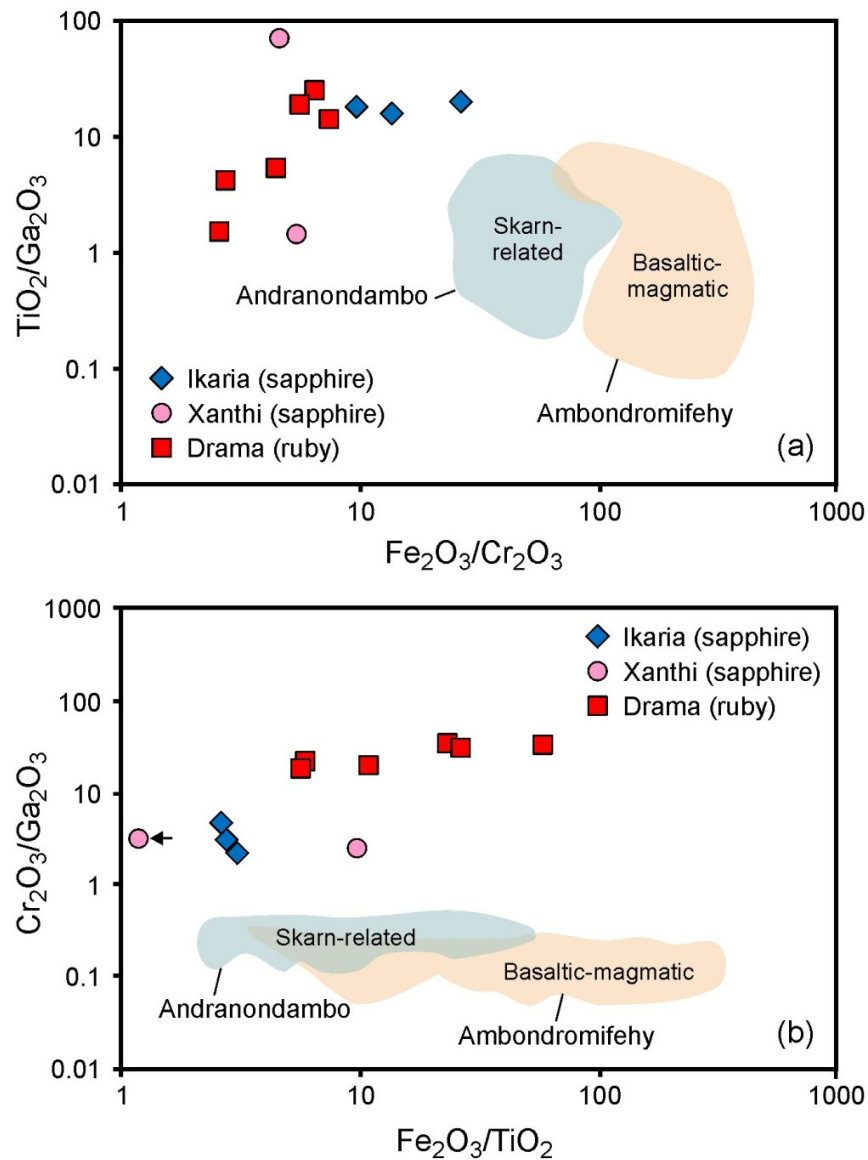


Fig. 4.4.3. a) Diagram TiO_2/Ga_2O_3 function of Fe_2O_3/Cr_2O_3 demonstrating the divergence of Drama's, Xanthi's and Ikaria's samples from the skarn-related and basaltic-magmatic population fields of Andranondambo and Ambondromifehy (modified after Schwarz et al. 2000).
b) Diagram Cr_2O_3/Ga_2O_3 function of Fe_2O_3/TiO_2 demonstrating the divergence of Drama's, Xanthi's and Ikaria's samples from the skarn-related and basaltic-magmatic population fields of Andranondambo and Ambondromifehy (modified after Schwarz et al. 2000).

Figure 4.4.4 illustrates the Cr/Ga versus Fe/Ti diagram, modified after Sutherland et al. (2009), displaying the fields for metamorphic and magmatic corundums along with the plots of Drama's, Xanthi's and Ikaria's samples. Naxos' samples and sample GOR from Xanthi contain no chromium and cannot plot in this diagram. All samples fall into the metamorphic field exhibiting a large variation of Fe/Ti ratios (especially pink to red samples from Drama and Xanthi). Drama's samples are displayed in the same area with Paranesti sapphires studied by Wang et al. (2017) (see Fig. 2.3.4.5 chapter 2). The same samples plot in the Fe-Cr*10-Ga*100 diagram (Fig. 4.4.5), modified after Sutherland et al. (2009). Ikaria's sapphires present higher iron values compared to Drama's and Xanthi's samples. In this diagram there is a small deviation between the plots presented by Wang et al. (2017) and the studied samples, with the second presenting higher Fe values and much lower Cr values, thus being displayed in the left corner of the diagram.

Figure 4.4.6 illustrates Fe-Ti-(Cr+V) diagram, modified after Peucat et al. 2007, plotting the fields for Colombia, Mogok and Umba metamorphic blue sapphires hosted in desilicated pegmatites (Colombia and Umba) and marbles (Mogok) along with the plots for Ikaria's samples, which seem to plot near the Mogok field. Naxos' samples and sample GOR cannot plot in this diagram, because of the absence of Cr.

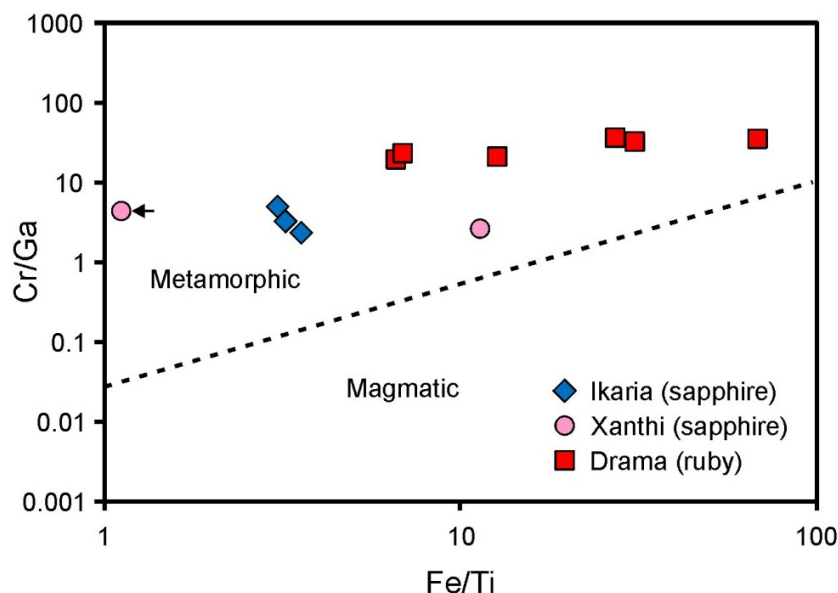


Fig. 4.4.4. Trace element discrimination diagram Cr/Ga versus Fe/Ti showing the fields for magmatic and metamorphic corundums. All studied samples fall into the metamorphic field. Samples with absence of chromium cannot plot in this diagram (modified after Sutherland et al., 2009).

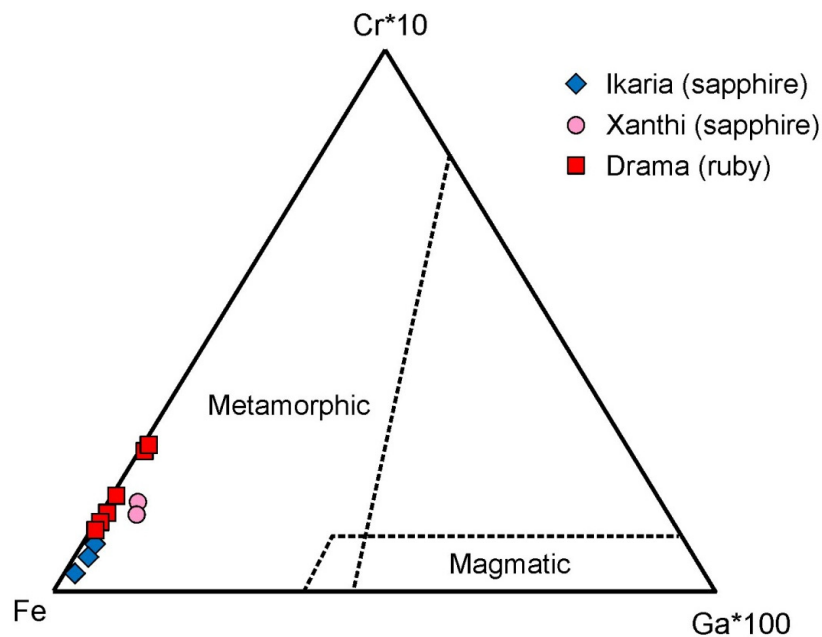


Fig. 4.4.5. Trace element discrimination diagram Fe-Cr*10-Ga*100 showing the fields for magmatic and metamorphic corundums. All studied samples fall into the metamorphic field. Samples with absence of chromium cannot plot in this diagram (modified after Sutherland et al., 2009).

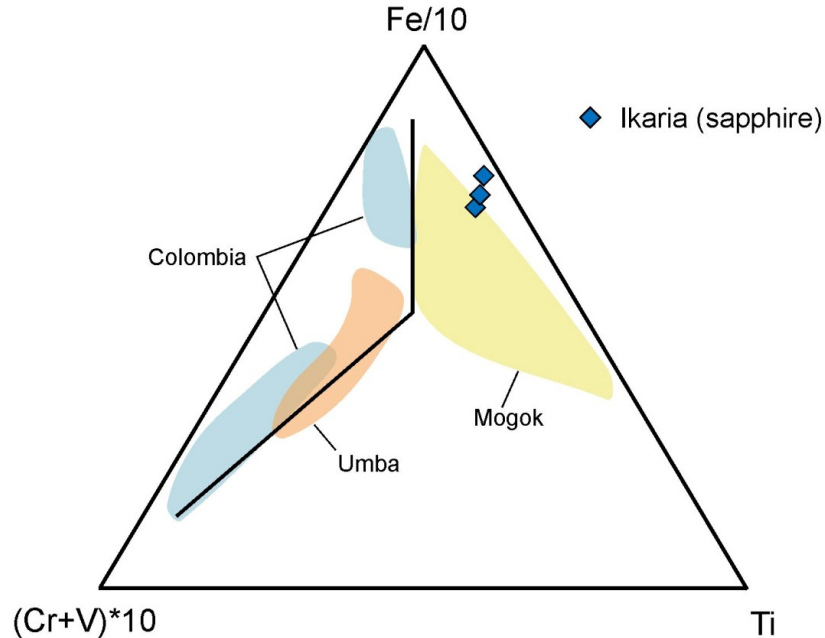


Fig. 4.4.6. Fe-Ti-(Cr+V) (ppm) diagram for Colombia, Mogok and Umba blue sapphires along with the plots from Ikaria (modified after Peucat et al. 2007).

Figure 4.4.7 illustrates a Cr_2O_3 versus Fe_2O_3 diagram, modified after Schwarz et al. (2008) in which different types of African deposits are plotted: marble-type from Mong Hsu and Mogok (Myanmar), gneissic-type metamorphosed in granulitic face from Mangari (Kenya) and Chimwadzulu (Malawi), amphibolitic-type metamorphosed in granulitic face from Songea and Winza (Tanzania) and basaltic-type from Thai (Thailand-Cambodia border region). Drama's and Ikaria's samples fall into the Winza field of corundum hosted in amphibolitic rocks metamorphosed in granulitic face - and more specifically in the area of the field with low Cr content - while Xanthi's samples lie in the area of low Fe_2O_3 and almost no Cr_2O_3 concentrations.

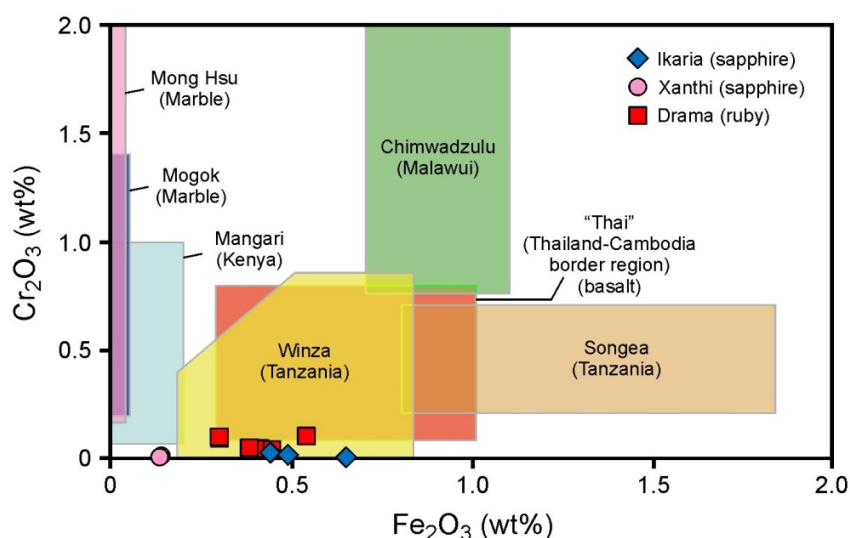


Fig. 4.4.7. Cr_2O_3 versus Fe_2O_3 correlation diagram plotting the fields of different African deposits along with the plots of Drama's, Xanthi's and Ikaria's samples (modified after Schwarz et al., 2008).

The $\text{Cr}_2\text{O}_3/\text{Ga}_2\text{O}_3$ versus $\text{Fe}_2\text{O}_3/\text{TiO}_2$ diagram in figure 4.4.8, modified after Rakotondrazafy et al. (2008), displays the geochemical fields of different types of corundum deposits. Drama's, Ikaria's and one value from Xanthi's sample GO5 fall into the metamorphic field. Ikaria's samples fall into the area of the diagram where the field of Vietnam's marble type corundum deposits overlaps with the geochemical field of Vietnam's desilicated pegmatite in marble deposits. Drama's PAR values fall into the field of Vietnam's marble type deposits, in the area where this field overlaps with the Soamiakatra field, while DR1 values (together with a PAR value) fall solely into the

Soamiakatra field of corundum hosted in clinopyroxenite enclaves in alkali basalts. Xanthi's GO5 presents a great variation, as it falls into Vietnam's marble type deposits, but only one of the two values is included in the field of metamorphic type deposits.

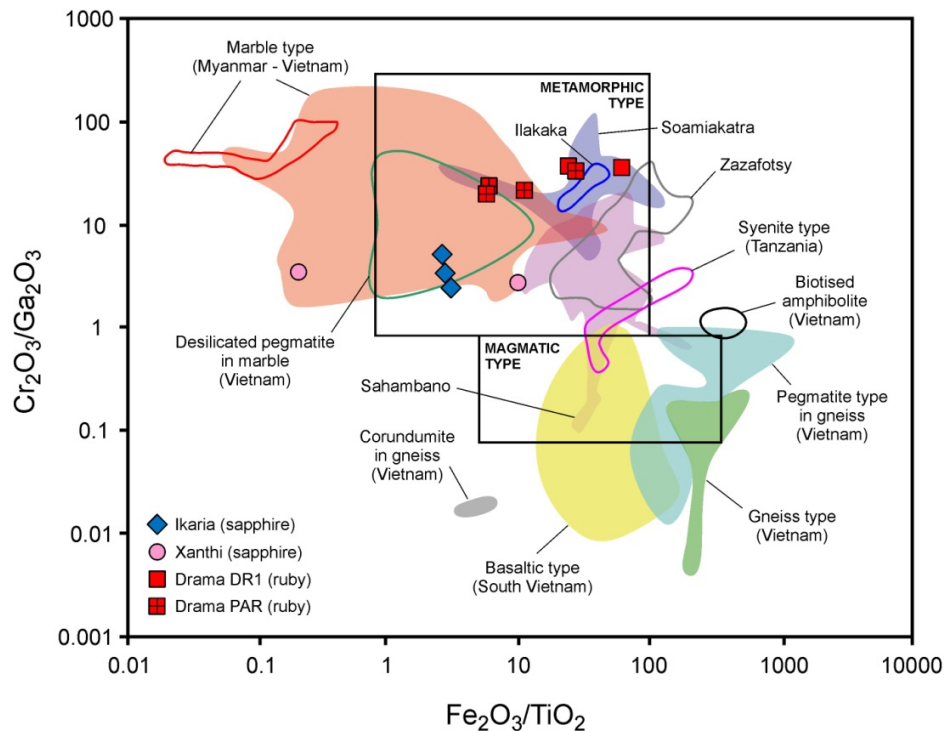


Fig. 4.4.8. Plot of the chemical composition of Drama's, Xanthi's and Ikaria's samples in a $\text{Cr}_2\text{O}_3/\text{Ga}_2\text{O}_3$ versus $\text{Fe}_2\text{O}_3/\text{TiO}_2$ diagram (modified after Rakotondrazafy et al., 2008; Sutherland et al., 1998, 2003; Pham Van et al., 2004; Simonet et al., 2004). The geochemical fields of Sahambano and Zazafotsy represent the fields of deposits hosted by feldspathic gneisses, while the Soamiakatra field represents the field of deposits hosted by clinopyroxenite enclaves in alkali basalts.

4.5. FLUID INCLUSIONS

The fluid inclusions study in the corundums (rubies and sapphires) from the four occurrences in Greece revealed the presence of CO_2 dominated fluids with very small quantities of CH_4 and/or N_2 , and relatively low densities, varying between 0.46 and 0.67 g/cm^3 . Type 1 primary and pseudosecondary water-free carbonic fluid inclusions represent the main fluid which was incorporated during the crystallization of rubies and

sapphires. The absence of any significant change in the fluid composition of the primary and pseudosecondary inclusions possibly suggests that the host rocks acted as a closed system which did not allow any contribution from external fluids.

Most of the corundums in different geological environments worldwide generally contain free-water, pure or nearly pure CO₂ fluids. Previous studies have shown that in metamorphic complexes, pure CO₂ bearing fluids were incorporated in the corundum formation from granulite facies rocks in Sri Lanka (De Maesschalck and Oen 1989), in the marble hosted ruby deposits from Luc Yen in North Vietnam (Giuliani et al. 2003) and from highly deformed paragneisses along the Nestos Shear Zone in Greece, where microdiamonds provide evidence for ultrahigh-pressure metamorphism (Krenn et al. 2008). Corundum occurrences with pure or almost pure CO₂ bearing fluids, without any water included, were documented in sapphires from pegmatites in the Kerala district of India (Menon et al. 1994) and in a corundum bearing skarn from granulites in Southeast Madagascar (Rakotondrazafy et al. 1996). In other corundum occurrences such as in the Kashmir blue sapphires and in the Thailand sapphires, CO₂ is an important component of the source fluids (Peretti et al. 1990, Srithai and Rankin 1999).

The occurrence of high density CO₂ rich fluid inclusions in granulite facies rocks shows that large amounts of CO₂ infiltrate the lower crust during the peak of metamorphism (Touret 1971, Newton et al. 1980, Morrison and Valley 1988). However, Hollister et al. (1979) have shown that low-density CO₂ fluid inclusions must have been trapped after the peak of metamorphism. Baker and Fallick (1988) suggested two main sources for the considerable input of pure CO₂ fluids in the lower crust: from the mantle (Newton et al. 1980, Newton 1986) or from the metamorphism of previously dehydrated crust (Lamb and Valley 1984, Newton 1986). It is documented that large quantities of CO₂ can be released through high grade (granulite) metamorphic devolatilization of a spilitic ocean floor or of the partly carbonaceous sediments. High Al and low Si protoliths in a high regional metamorphic grade can produce a pure supercritical CO₂ fluid and lead to the formation of corundum. A mantle derived CO₂ has been suggested for Naxos by Schuiling and Kreulen (1979).

In the present study of the corundums from Greece, similar fluids, containing almost pure CO₂, have been documented. Water was not identified in the fluid inclusions neither

by optical microscopy nor by any phase transition during microthermometry. This excludes the possibility of fluid immiscibility for the corundum formation and implies the presence of a primary water-free CO₂ dominated fluid at high P-T conditions.

It is very possible that the studied primary low-density fluid inclusions ($d = 0.46\text{--}0.67 \text{ g/cm}^3$) were entrapped after the peak of metamorphism. The pseudosecondary, also low density, carbonic fluid inclusions were entrapped in trails during the corundums formation process and are related to the evolution of the metamorphic events at a retrograde metamorphic regime of cooling and uplift and the subsequent exhumation, also after the peak of the granulite facies metamorphism. Similar formation conditions were documented for the corundums in gem gravels in Sri Lanka by De Maesschalck and Oen (1989).

The variations in the density of the fluid inclusions (0.46 and 0.67 g/cm^3) are interpreted to result from the variation of pressures associated with successive localized microfracturing, a process which was suggested in the case of Luc Yen rubies of North Vietnam (Giuliani et al. 2003).

4.6. CLASSIFICATION OF STUDIED SAMPLES

According to the results taken from all the analytical methods the studied samples can be classified into the categories proposed by Giuliani et al. (2007, 2012) and Simonet et al. (2008) (see chapter 1: Table 1.5.1, 1.5.2).

Blue samples: Despite their plumasitic origin, based on the results taken from the UV-Vis-NIR analysis, Naxos' samples seem to be both of metamorphic and metasomatic nature. The rest of the analytical methods enhance the theory for their origin from two different geological environments. Sample NX1 presents characteristic features of metasomatic origin, falling into the category of sapphire in plumasites of table 1.5.1 and in the category of sapphire-bearing desilicated pegmatites (plumasites) of table 1.5.2. On the contrary, samples NX2 and NX4 seem to have a quite different nature.

Ikaria's samples can be characterized as metamorphic deposits, falling into the same category with samples NX2 and NX4 from Naxos: the one of ruby and sapphire-bearing desilicated pegmatites in skarns of table 1.5.1 and that of sapphire-bearing skarns of table 1.5.2. The results of this thesis accord with the results presented for Ikaria's sapphires from literature references.

Xanthi's GOR falls into the category of ruby and sapphire-bearing meta-limestones of the metamorphic s.s. deposits according to both classification tables. The results taken from FTIR and UV-Vis-NIR analysis for this sample are typical of blue sapphires hosted in meta-limestones. Though high values of TiO_2 concentration have been recorded for Xanthi's blue sapphires, the concentration of TiO_2 in GOR is generally low. In addition, Fe content presents a great variation, from very low to quite high values, thus creating an uncertainty over the actual origin of sapphires. We can suggest the possible origination of Xanthi's blue sapphires from the eclogitic amphibolites and not from the marbles. In this case, the classification changes to ruby and sapphire-bearing gneisses (of granulite facies) of table 1.5.1 and sapphire-bearing aluminous gneisses and granulites of table 1.5.2.

Pink to red samples: Xanthi's GO5 also shows characteristic features of sapphire-bearing metalimestones. It could be classified to the same category as GOR of ruby and sapphire-bearing metalimestones of the metamorphic s.s. deposits according to both classification tables.

Drama's samples fall into the category of ruby-bearing amphibolites of metamorphic s.s. deposits in table 1.5.1 and the category of ruby-bearing mafic granulites of metamorphic s.s. deposits in table 1.5.2. The results taken from all the analytical methods are typical of ruby-bearing amphibolites or mafic granulites and are, generally, in accordance with the results of literature references for Drama's rubies. A small deviation is presented in the trace element correlation diagrams, where Fe and Cr show higher and lower values respectively, than the ones reported by Wang et al. (2017) for Paraneesti rubies.

Different analytical methods were conducted to a group of 15 corundum samples from Naxos, Ikaria, Drama and Xanthi areas in Greece. The aim was to find the similarities and differences between the four deposits and to record the characteristic features of each deposit.

Under the polarizing microscope all the samples presented in general parting, polysynthetic twinning, color zoning and strong fragmentation. A large number of fluid and mineral inclusions was observed in all samples. Apart from Xanthi's samples, traces of chlorite were found in all the other samples. Traces of biotite were found in Naxos' and Ikaria's samples.

The FTIR analysis showed the presence of boehmite and CO₂ related to fluid inclusions in all samples. Diaspore-related peaks were identified for Ikaria's, Xanthi's and Drama's samples. The strongest absorption bands were detected in Ikaria's IK1 and Xanthi's GOR, which are the most fractured samples. The epigenetic nature of boehmite and diaspore inclusions, as well as, the correlation between the intensity of absorption and the intensity of the deformation the samples had undergone, were concluded.

The UV-Vis-NIR analysis verified the relation between the color of corundum and the chromophore agents. The absorption spectra showed that the basic agent for the coloration of pink to red samples (GO5, DR1 and PAR) was the chromophore Cr³⁺ in combination to very weak Fe³⁺ absorptions, while for the blue samples (NX1, NX2, NX4, IK1 and GOR) the basic agent was the intervalence charge transfer by Fe²⁺/Ti⁴⁺. The spectra of GO5 pink sapphire from Xanthi presented weak Cr³⁺ absorption probably the cause for its pink color. The non-basalt related origin of all studied samples was also verified. Apart from Naxos' NX1 which was the only sample showing metasomatic features, a metamorphic nature was concluded for all samples.

Among the pink to red samples, the EDXRF analysis gave the highest Cr₂O₃ concentration for Drama's samples and the lowest for Xanthi's GO5. The highest Fe₂O₃ and TiO₂ concentration values were recorded in the samples from Naxos. Based on their chemical composition Drama's and Ikaria's samples and Xanthi's pink sapphire fall into the metamorphic field of corundum. However, Naxos' samples presented a wide variation

concerning their chemical composition, indicating the possibility of different formation environments for the samples; only sample NX1 showed a clear plumasitic-metasomatic origin though all samples were found within Naxos' plumasites.

The examination of the fluid inclusions within corundum showed that they are dominated by CO₂ with very small quantities of CH₄ and/or N₂, are water free and have low densities (0.46 and 0.67 g/cm³). The CO₂ rich fluids were possibly incorporated in the lower crust from the mantle or from the devolatilization of a spilitic ocean floor during high grade (granulite) metamorphism. However, the low density carbonic fluid inclusions in the studied corundums were entrapped after the peak of metamorphism at a retrograde metamorphic regime of cooling and uplift and the subsequent exhumation.

The strong fragmentation of the corundum crystals enhances the theory of a strong deformational event taking place after the formation of corundum. This characteristic together with the strong parting of the crystals and the presence of a large number of mineral and fluid inclusions render the studied samples of a non-gemological value.

A further examination of the rubies and sapphires from Greece, with other analytical techniques (i.e. Scanning Electron Microscope, LA-ICP-MS, Raman Spectroscopy etc.) could build a larger database concerning the gemological value of Greek corundum deposits and spread more light to their geological history and evolution model.

The gem corundum deposits in Greece are spotted in four regions along two tectono-metamorphic units of the Hellenides Orogen: Drama (Paranesti) and Xanthi (Gorgona-Stirigma) along Nestos Suture Zone in the Rhodope Massif and Naxos and Ikaria islands at the Attico-Cycladic Massif. Eight samples were examined in order to discriminate the four deposits and to record their characteristic features: two rubies from Drama hosted in amphibole schist lenses intercalated in places with Ky-bearing Qtz-Plag-amphibolite gneisses, one pink and one blue sapphire from Xanthi hosted in marbles intercalated with eclogitic amphibolites and gneisses, three blue sapphires from Naxos found within plumasites which were formed by the interaction of pegmatites with ultramafic rocks and a blue sapphire from Ikaria found within the meta-bauxitic lenses hosted within calcic marbles, near the contact with the upper gneisses. Under the polarizing microscope all the samples presented parting, polysynthetic twinning, color zoning and strong fragmentation. A large number of fluid inclusions and few mineral inclusions were also identified. The FTIR analysis showed the presence of boehmite in all samples. Diaspore-related peaks were also observed in Ikaria's, Xanthi's and Drama's spectra. The CO₂ peaks present in all the samples are attributed to the fluid inclusions. The UV-Vis-NIR analysis showed the presence of Cr³⁺ in the red to pink samples and the presence of Fe²⁺-Ti⁴⁺ intervalence charge transfer in the blue samples. Apart from one sample from Naxos showing features of metasomatic origin, all the other samples demonstrated characteristics of a metamorphic origin. The EDXRF analysis gave the highest Cr₂O₃ concentration for Drama's samples and the lowest for Xanthi's sample GO₅. The highest Fe₂O₃ and TiO₂ content was recorded in the samples from Naxos, though the wide variation of their chemical composition indicates the possibility of different formation environments. The fluid inclusions study verified the presence of water free CO₂ dominated fluids with traces of CH₄ or N₂ and low densities (0.46 and 0.67 g/cm³), which were probably trapped after the metamorphism peak. The strong fragmentation of ruby and sapphire crystals is possibly due to a strong deformational event after the formation of corundum and together with the clear parting and the large number of mineral and fluid inclusions render the Greek samples of a non-gemological value.

Keywords: gemology, corundum, ruby, sapphire, FTIR, UV-Vis-NIR, EDXRF, fluid inclusions, Rhodope Massif, Attico-Cycladic Massif, Drama, Xanthi, Ikaria, Naxos, Greece

ΠΕΡΙΛΗΨΗ

Οι πολύτιμες ποικιλίες του κορουνδίου στην Ελλάδα εντοπίζονται σε τέσσερις περιοχές κατά μήκος δύο μεταμορφικών συμπλεγμάτων του ευρύτερου Ελληνικού Ορογενούς: στο Παρανέστι Δράμας και στη Γοργόνα-Στήριγμα Ξάνθης κατά μήκος της Ζώνης Επώθησης του Νέστου (Μάζα Ροδόπης) και στα νησιά Νάξος και Ικαρία (Αττικο-Κυκλαδική Μάζα). Οχτώ δείγματα εξετάστηκαν προκειμένου να μελετηθούν οι ομοιότητες και διαφορές των τεσσάρων εμφανίσεων καθώς και να καταγραφούν τα χαρακτηριστικά της κάθε εμφάνισης: δύο ρουμπίνια από την εμφάνιση της Δράμας που εντοπίζονται μέσα σε φακούς αμφιβολιτικών σχιστολίθων που περιβάλλονται από κυανιτικούς χαλαζιο-αστριούχους αμφιβολιτικούς γνευσίους, ένα ροζ και ένα μπλε ζαφείρι από την Ξάνθη μέσα σε μάρμαρα που εναλλάσσονται με εκλογιτικούς αμφιβολίτες και γνευσίους, τρία μπλε ζαφείρια από την Νάξο μέσα σε πλουμασίτες προερχόμενες από την αλληλεπίδραση μεταξύ πηγματιτών και υπερβασικών πετρωμάτων και ένα μπλε ζαφείρι από την Ικαρία μέσα σε μετα-βωξιτικούς φακούς που συναντώνται σε ασβεστίτικα μάρμαρα κοντά στην επαφή με τους υπερκείμενους γνευσίους. Η παρατήρηση στο πολωτικό μικροσκόπιο έδειξε χαρακτηριστικά αποχωρισμού, πολυδυμιών, χρωματικής ζώνωσης και κατακλαστικής υφής για όλα τα δείγματα. Επίσης παρατηρήθηκε μεγάλος αριθμός ρευστών εγκλεισμάτων καθώς και αρκετά ορυκτά εγκλείσματα. Η φασματοσκοπία υπέρυθρου (FTIR) έδειξε την παρουσία μπαιμίτη σε όλα τα δείγματα και την παρουσία διασπόρου στα δείγματα της Ικαρίας, Ξάνθης και Δράμας. Οι κορυφές απορρόφησης CO₂ των φασμάτων αποδόθηκαν στο CO₂ των ρευστών εγκλεισμάτων. Η φασματοσκοπία υπεριώδους-ορατού-κοντινού υπέρυθρου (UV-Vis-NIR) έδειξε την παρουσία Cr³⁺ στα φάσματα των κόκκινων έως ροζ δειγμάτων και την παρουσία Fe²⁺-Ti⁴⁺ στα φάσματα των μπλε δειγμάτων. Εκτός από ένα μπλε ζαφείρι της Νάξου που έχει χαρακτηριστικά μετασωματικού χαρακτήρα, όλα τα υπόλοιπα δείγματα σχετίζονται με μεταμορφική προέλευση. Οι υψηλότερες συγκεντρώσεις Cr₂O₃ εντοπίστηκαν στις χημικές αναλύσεις των ρουμπινιών της Δράμας, ενώ οι χαμηλότερες

στο ροζ ζαφείρι της Ξάνθης. Τα μπλε ζαφείρια της Νάξου έχουν τις υψηλότερες συγκεντρώσεις Fe_2O_3 και TiO_2 . Γενικά τα δείγματα της Νάξου παρουσίασαν το μεγαλύτερο εύρος τιμών αναφορικά με τη χημική τους σύσταση, γεγονός που υποδεικνύει την πιθανή προέλευσή τους από διαφορετικά περιβάλλοντα. Η μελέτη των ρευστών εγκλεισμάτων επιβεβαίωσε την παρουσία ρευστών πλούσιων σε CO_2 με μικρά ποσοστά CH_4 ή N_2 , χωρίς την παρουσία νερού και με μικρές πυκνότητες (0.46 and 0.67 g/cm^3), που πιθανόν παγιδεύτηκαν μετά την κορύφωση της μεταμόρφωσης. Τα έντονα φαινόμενα κατακλαστικής υφής των ρουμπινιών και ζαφειριών επιβεβαιώνουν την υπόθεση ενός ισχυρού παραμορφωτικού επεισοδίου που έλαβε χώρα μετά το σχηματισμό τους. Η κατακλαστική υφή σε συνδυασμό με τον έντονο αποχωρισμό των δειγμάτων και τον μεγάλο αριθμό ρευστών και ορυκτών εγκλεισμάτων καθιστούν τα ελληνικά κορούνδια μη γεωλογικής αξίας.

Λέξεις κλειδιά: γεωλογία, κορούνδιο, ρουμπίνι, ζαφείρι, φασματοσκοπία υπερύθρου, φασματοσκοπία υπεριώδους-ορατού-κοντινού υπερύθρου, EDXRF, ρευστά εγκλείσματα, Μάζα Ροδόπης, Αττικο-κυκλαδική Μάζα, Δράμα, Ξάνθη, Ικαρία, Νάξος, Ελλάδα

- Altherr, R., Henjes-Kunst, F., Matthews, A., Friedrichsen, H. and Hansen, B.T., 1988. O-Sr isotopic variations in Miocene granitoids from the Aegean: evidence for an origin by combined assimilation and fractional crystallization. *Contributions to Mineralogy and Petrology*, 100, 4, 528-541.
- Altherr, R., Kreuzer, H., Lenz, H., Wendt, I., Harre, W. and Dürr, S., 1994. Further evidence for a Late Cretaceous low-pressure/high-temperature terrane in the Cyclades, Greece, *Chemie der Erde*, 54, 319-328.
- Altherr, R., Kreuzer, H., Wendt, I., Lenz, H., Wagner, G.A., Keller, J., Harre, W. and Höhndorf, A., 1982. A late Oligocene/early Miocene high temperature belt in the Attic-Cycladic crystalline complex (SE Pelagonian, Greece). *Geologisches Jahrbuch E.*, 23, 97-164.
- Anders, B., Reischmann, T. and Kostopoulos, D., 2007. Zircon geochronology of basement rocks from the Pelagonian Zone, Greece: constraints on the pre-Alpine evolution of the westernmost Internal Hellenides. *International Journal of Earth Sciences*, 96, 639-661.
- Andriessen, P.A.M., 1991. K-Ar and Rb-Sr age determinations on micas of impure marbles on Naxos, Greece: the influence of metamorphic fluids and lithology on the blocking temperature. *Schweizerische mineralogische und petrographische Mitteilungen*, 71, 89-99.
- Andriessen, P.A.M., Banga, G., and Hebeda, E.H., 1987. Isotopic age study of pre-Alpine rocks in the basal units on Naxos, Sikinos and Ios, Greek Cyclades. *Geologie en Mijnbouw*, 66, 3, 3-14.
- Andriessen, P.A.M., Hebedaa, E.H., Simonb, O.J. and Verschurea, R.H., 1991. Tourmaline K/Ar ages compared to other radiometric dating systems in Alpine anatectic leucosomes and metamorphic rocks (Cyclades and southern Spain). *Chemical Geology*, 91, 1, 33-48.

- Anthony, J.W., Bideaux, R.A., Bladh, K.W. and Nichols, M.C., 1997. *Handbook of Mineralogy, Vol. 3, Halides, Hydroxides, Oxides*. Mineral Data Publishing Tucson, Arizona, 630 pp.
- Avigad, D. and Garfunkel, T., 1989. Low-angle faults above and below a blueschist belt, Tinos Island, Cyclades, Greece. *Terra Nova*, 1, 182-187.
- Baker, J. and Matthews, A., 1995. The stable isotopic evolution of a metamorphic complex, Naxos, Greece. *Contributions to Mineralogy and Petrology*, 120, 3, 391-403.
- Barr, S.R., Temperley, S. and Tarney, J., 1999. Lateral growth of the continental crust through deep level subduction-accretion: a re-evaluation of central Greek Rhodope. *Lithos*, 46, 69-94.
- Bauer, C., Rubatto, D., Krenn, K., Proyer, A. and Hoinkes, G., 2007. A zircon study from the Rhodope Metamorphic Complex, Northern Greece: time record of a multistage evolution. *Lithos*, 99, 3-4, 207-228.
- Baziotis, I., Mposkos, E. and Perdikatsis, V., 2007. Geochemistry of amphibolitized eclogites and crosscutting tonalitic-trondhjemitic dykes in the Metamorphic Kimi Complex in East Rhodope (N.E. Greece): implications for partial melting at the base of a thickened crust. *International Journal of Earth Science*, 97, 3, 459-477.
- Belt, R.F., 1967. Hydrothermal ruby: Infrared spectra and X-ray topography. *Journal of Applied Physics*, 38, 6, 2688-2689.
- Beran, A., 1991. Trace hydrogen in Verneuil-grown corundum and its colour varieties - an IR spectroscopic study. *European Journal of Mineralogy*, 3, 6, 971-975.
- Beran, A. and Rossman, G.R., 2006. OH in naturally occurring corundum. *European Journal of Mineralogy*, 18, 4, 441-447.
- Bodnar, R.J., 2003. Introduction to fluid inclusions. In: Samson, I.M., Anderson, A.J. and Marshall, D.D. (eds) *Fluid inclusions: Analysis and Interpretation*. Mineralogical Association of Canada, Short Course Series 32, 1-8.

Boronkay, K. and Doutsos, T., 1994. Transpression and transtension within different structural levels in the central Aegean region. *Journal of Structural Geology*, 16, 11, 1555-1573.

Bottinga, Y. and Richet, P., 1981. High pressure and temperature equation of state and calculation of the thermodynamic properties of gaseous carbon dioxide, *American Journal of Sciences*, 281, 615-660.

Bröcker, M. and Franz, L., 1998. Rb–Sr isotope studies on Tinos Island (Cyclades, Greece): additional time constraints for metamorphism, extent of infiltration-controlled overprinting and deformational activity. *Geological Magazine*, 135, 3, 369-382.

Brown, P., 1989. FLINCOR: a microcomputer program for the reduction and investigation of fluid-inclusion data. *American Mineralogist*, 74, 1390-1393.

Brown, W.H. and Poon, T., 2005. *Introduction to organic chemistry*. John Wiley & Sons.

Brun, J-P. and Sokoutis, D., 2007. Kinematics of the Southern Rhodope Core Complex (North Greece). *International Journal of Earth Sciences (Geol Rundsch)*, 96, 6, 1079-1099.

Buick, I.S. and Holland, T.J.B., 1989. The P-T path associated with crustal extension, Naxos, Cyclades, Greece, In: Daly, J.S., Cliff, R.A. and Yardley, B.W.D. (eds) *Evolution on Metamorphic Belts*. Geological Society of London, Special Publications, 43, 1, 365-369.

Buick, I.S. and Holland, T.J.B., 1991. The nature and distribution of fluids during amphibolite facies metamorphism, Naxos (Greece). *Journal of Metamorphic Geology*, 9, 3, 301-314.

Burg, J-P., 2012. Rhodope: from Mesozoic convergence to Cenozoic extension. Review of petro-structural data in the geochronological frame. *Journal of the Virtual Explorer*, 42, 1-44.

Cartier, L.E., 2009. Ruby and sapphire from Marosely, Madagascar. *The Journal of Gemmology*, 31, 5-8, 171-179.

Coccato, A., 2011. *Non-destructive studies of gem quality and Neolithic jade materials*.

M.Sc. thesis, Università Degli Studi di Parma, Italy, 123 pp.

De Maesschalck, A.A. and Oen, I.S., 1989. Fluid and mineral inclusions in corundum from gem gravels in Sri Lanka. *Mineralogical Magazine*, 53, 539–545.

Derrick, M.R., Stulic, D. and Landry, J.M., 1999. *Scientific tools for conservation: Infrared spectroscopy in conservation science*. The Getty Conservation Institute, Los Angeles, 235 pp.

Doutsos, T., Piper, G., Boronkay, K. and Koukouvelas, I., 1993. Kinematics of the Central Hellenidesm. *Tectonics*, 12, 936-953.

Driesner, T. and Heinrich, C.A., 2007. The system H₂O-NaCl. I. Correlations for molar volume, enthalpy and isobaric heat capacity from 0 to 1000 degrees C, 1 to 5000 bar, and 0 to 1 X-NaCl. *Geochimica et Cosmochimica Acta*, 71, 4880-4901.

Duroc-Danner, J., 2002. *A study of Colombian corundum*. Diplôme d'Université en Gemmologie (DUG), Université de Nantes, France, 216 pp.

Dürr, S., Altherr, R., Keller, J., Okrusch, M. and Seidel, E., 1978. The median Aegean crystalline belt: stratigraphy, structure, metamorphism, magmatism. In: Closs, H., Roeder, D.H. and Schmidt, K. (eds) *Alps, Apennines, Hellenides*. IUGS report no.38, Schweizerbart, Stuttgart, 455-476.

Edwards, H. and Vandenabeele, P., 2016. *Analytical Archaeometry: Selected Topics*. The Royal Society of Chemistry, Cambridge, 593 pp.

Eigenmann, K. and Günthard, H., 1971. Hydrogen incorporation in doped α -Al₂O₃ by high temperature redox reactions. *Chemical Physics Letters*, 12, 1, 12-15.

Eigenmann, K. and Günthard, H., 1972. Valence states, redox reactions and biparticle formation of Fe and Ti doped sapphire. *Chemical Physics Letters*, 13, 1, 58-61.

Eigenmann, K., Kurtz, K. and Günthard, H., 1972. Solid state reactions and defects in doped Verneuil Sapphire. *Helvet Physica Acta*, 45, 452-480.

Eigenmann, K., Kurtz, K. and Günthard, H., 1972. The optical spectrum of α -Al₂O₃: Fe³⁺. *Chemical Physics Letters*, 13, 1, 54-57.

- Elmaleh, E., 2014. *Blue sapphires from Madagascar, Sri Lanka, Tanzania and Burma (Myanmar): gemological, chemical, spectroscopic characterization and dating of zircon inclusions*. M.Sc. thesis, Université de Genève, Switzerland, 135 pp.
- Emmett, J.L., Dubinsky, E.V., Hughes, R.W. and Scarratt, K., 2017. Color, Spectra & Luminescence. In: Hughes, R. (ed) *Ruby & Sapphire: A Gemmologist's guide*. RWH Publishing, 90-148.
- Emmett, J.L., Scarratt, K., McClure, S.F., Moses, T., Douthit, T.R., Hughes, R., Novak, S., Shigley, J.E., Wang, W., Bordelon, O. and Kane, R.E., 2003. Beryllium diffusion of ruby and sapphire. *Gems & Gemology*, 3, 2, 84-135.
- Faure, M., Bonneau, M. and Pons, J., 1991. Ductile deformation and syntectonic granite emplacement during the late Miocene extension of the Aegean (Greece): *Bulletin de la Société géologique de France*, 162, 1, 3-11.
- Feenstra, A., 1985. *Metamorphism of bauxites on Naxos, Greece*. Ph.D. thesis, Instituut voor Aardwetenschappen, Rijksuniversiteit te Utrecht, The Netherlands, 206 pp.
- Feenstra, A., and Wunder, B., 2002. Dehydration of diasporite to corundite in nature and experiment. *Geology*, 30, 2, 119-122.
- Ferguson, J. and Fielding, P.E., 1971. The origin of the colours of yellow, green and blue sapphires. *Chemical Physics Letters*, 10, 3, 262-265.
- Ferguson, J. and Fielding, P.E., 1972. The origins of the colours of natural yellow, blue, and green sapphires. *Australian Journal of Chemistry*, 25, 7, 1371-1385.
- Filipov, P. and Marchev, P., 2011. U-Pb zircon and $^{40}\text{Ar}/^{39}\text{Ar}$ ages of Mesta volcanic rocks and Central Pirin pluton. *Bulgarian National Conference "GEOSCIENCES 2011"*, 49-50.
- Forster, M. A. and Lister, G. S., 2005. Several distinct tectono-metamorphic slices in the Cycladic eclogite–blueschist belt, Greece. *Contributions to Mineralogy and Petrology*, 150, 5, 523–545.
- Frederickson, L.D.Jr., 1954. Characterization of hydrated aluminas by infrared spectroscopy. *Analytical Chemistry*, 26, 12, 1883-1885.

- Fritsch, E. and Rossman, G.R., 1987. An update on color in gems. Part I. Introduction and colors caused by dispersed metal ions, *Gems & Gemology*, 23, 126-139.
- Fytikas, M., Innocenti, F., Manetti, P., Mazzuoli, R., Peccerillo, A. and Villari, L., 1984. Tertiary to Quaternary evolution of volcanism in the Aegean region, In Robertson, A.H.F. and Dixon, J.E. (eds) *The geological evolution of the Eastern Mediterranean*. Geological Society of London, Special Publications, 17, 687-699.
- Garnier, V., Giuliani, G., Ohnenstetter, D., Fallick, A.E., Dubessy, J., Banks, D., Hoang Quang, V., Lhomme, T., Maluski, H., Pêcher, A., Bakhsh, K. A., Pham Van, L., Phan Trong, T. and Schwarz, D., 2006. Marble-hosted ruby deposits from Central and Southeast Asia: towards a new genetic model. *Ore Geology reviews*, 34, 169-191.
- Garnier, V., Giuliani, G., Ohnenstetter, D., Schwarz, D. and Kausar, A.B., 2006a. Les gisements de rubis associés aux marbres de l'Asie centrale et du Sud-est. *Règne Minéral*, 67, 17-48.
- Garnier, V., Maluski, H., Giuliani, G., Ohnenstetter, D. and Schwarz, D., 2006b. Ar-Ar and U-Pb ages of marble hosted ruby deposits from central and southeast Asia. *Canadian Journal of Earth Sciences*, 43, 1-23.
- Garnier, V., Ohnenstetter D., Giuliani G. and Schwarz, D., 2002. Rubis trapiches de Mong Hsu, Myanmar. *Review de Gemmology*, 144, 5-12.
- Garnier, V., Ohnenstetter D., Giuliani G. and Schwarz, D., 2004. Saphirs et rubis. Classification des gisements de corindon. *Règne Minéral*, 55, 4-47.
- Garnier, V., Ohnenstetter D., Giuliani G., Fallick A.E., Phan Trong T., Schwarz, D., Hoang Quang V. and Pham Van L., 2005. Basalt petrology, zircon ages and sapphire genesis from Dak Nong, Southern Vietnam. *Mineralogical Magazine*, 69, 1, 21-38.
- Garrels, R.M. and Christ, C.L., 1965. *Solutions, minerals and equilibria*. Harper and Row, New York, 450 pp.
- Gautier, P. and Brun, J.P., 1994. Crustal-scale geometry and kinematics of late-orogenic extension in the central Aegean (Cyclades and Ewia Island). *Tectonophysics*, 238, 1-4, 399-424.

- Gautier, P. and Brun, J.P., 1994. Ductile crust exhumation and extensional detachments in the central Aegean (Cyclades and Evvia Islands). *Geodinamica Acta*, 7, 2, 57-85.
- Gautier, P., Brun, J.P. and Jolivet, L., 1993. Structure and kinematics of upper Cenozoic extensional detachment on Naxos and Paros (Cyclades Islands, Greece). *Tectonics*, 12, 5, 1180-1194.
- Gautier, P., Gerdjikov, I., Ruffet, G., Bosse, V., Cherneva, Z., Pitra P. and Hallot, E., 2010. Persistent synmetamorphic thrusting in the Rhodope until 33 Ma: evidence from the Nestos Shear Zone and implications for Aegean geodynamics. *19th Congress of the Carpathian-Balkan Geological Association, 23-26 September, 2010, Thessaloniki, Greece, Geologica Balcanica*, 39, 122-123.
- Giuliani, G., Dubessy, J., Banks, D., Quang, V.H., Lhomme, T., Pironon, J., Garniere, V., Trong Trinh, P., Van Long, P., Ohnenstetter, D., and Schwarz D., 2003. CO₂-H₂S-COS-S₈-AlO(OH)-bearing fluid inclusions in ruby from marble-hosted deposits in Luc Yen area, North Vietnam. *Chemical Geology*, 194, 1, 167-185.
- Giuliani, G., Fallick, A.E., Garnier, V., France-Lanord, Ch., Ohnenstetter, D. and Schwarz, D., 2005. Oxygen isotope composition as a tracer for the origins of rubies and sapphires. *Geology*, 33, 249-252.
- Giuliani, G., Ohnenstetter D., Fallick A.E., Groat, L. and Fagan, A.J., 2014. The geology and genesis of gem corundum deposits. In: Groat, L. (ed) *Geology of gem deposits*. Mineralogical Association of Canada, Short Course Series 44, Tucson, USA.
- Giuliani, G., Ohnenstetter, D., Fallick, A.E., Groat, L.A. and Feneyrol, J., 2012. Geographic origin of gems linked to their geological history. *InColor*, 19, 16-27.
- Giuliani, G., Ohnenstetter, D., Garnier, V., Fallick, A.E., Rakotondrazafy, M. and Schwarz, D., 2007. The geology and genesis of gem corundum deposits. In: Groat, L. (ed) *Geology of gem deposits*. Mineralogical Association of Canada, Short Course Series 37, Québec, Canada, 23-78.
- Godfriaux, I., 1968. Etude géologique de la region de l'Olympe (Grèce). *Annales Géologiques des Pays Helleniques*, 19, 1-271.

- Graham, I., Voudouris, P., Melfos, V., Zaw, K., Meffre, S., Sutherland, F., Giuliani, G. and Fallick, A., 2012. Gem corundum deposits of Greece: a spectrum of compositions and origins. *34th IGC conference, Brisbane, Australia*.
- Graham, I.T., Khin, Z. and Cook, N., J., 2008. The genesis of gem deposits. *Ore Geology Reviews*, 34, 1-2, 215.
- Häger, T., 1996. *Farbrelevante Wechselwirkungen von Spurenelementen in Korund*. Ph.D. thesis, Johannes Gutenberg-Universität, Mainz, Germany, 170 pp.
- Häger, T. and Greiff, S.K., 1994. A study of hydrous components in corundum. *European Journal of Mineralogy*, 6, 89.
- Henjes-Kunst, F., Altherr, R., Kreuzer, H. and Hansen, B.T., 1988. Disturbed U-Th-Pb systematics of young zircons and uranothorites: the case of the Miocene Aegean Granitoids (Greece). *Chemical Geology, Isotope Geoscience section*, 73, 2, 125-145.
- Henley, R.W., Truesdell, A.H., Barton, P.B.Jr. and Whitney, J.A., 1984. Fluid-mineral equilibria in hydrothermal systems. *Reviews in Economic Geology*, 1, 1-267.
- Hezel, D. and Kalt, A., 2011. Major-element and Li, Be compositional evolution of tourmaline in an S-type granite-pegmatite system and its country rocks: an example from Ikaria, Aegean Sea, Greece. *The Canadian Mineralogist*, 49, 321-340.
- Hollister, L.S., Burruss, R.C., Henry, D.L. and Hendel, E.M., 1979. Physical conditions during uplift of metamorphic terrains, as recorded by fluid inclusions. *Bulletin de Minéralogie*, 102, 555-561.
- Hughes, R., W., 1997. *Ruby and sapphire*. RWH publishing, Bangkok, 512 pp.
- Hughes, R.W., 1990. *Corundum*. Butterworth's Gem Books, Butterworth-Heinemann, London, 315 pp.
- Iliopoulos, I., 2005. *Petrogenesis of metamorphic rocks from Ikaria Island*. Ph.D. thesis, University of Patras, Greece, 592 pp. (in Greek).
- Iliopoulos, I. and Katagas, C., 2004. Corundum bearing metabauxites from Ikaria island (Greece): mineralogy and geochemistry. *10th International Congress of the Geological Society of Greece, 15-17 April, 2004, Thessaloniki, Greece*, 423-424.

- Jahn-Awe, S., Froitzheim, N., Nagel, T.J., Frei, D., Georgiev, N. and Pleuger, J., 2010. Structural and geochronological evidence for Paleogene thrusting in the western Rhodopes, SW Bulgaria: elements for a new tectonic model of the Rhodope Metamorphic Province. *Tectonics*, 29, TC3008, doi:10.1029/2009TC002558.
- Jansen, J.B.H. and Schuiling, R.D., 1976. Metamorphism on Naxos; petrology and geothermal gradients. *American Journal of Science*, 276, 10, 1225-1253.
- Jansen, J.B.H., Feenstra, A., Schuiling, R.D., 1987. A spinel-forming reaction in aluminous dolomitic marbles of Naxos, Greece. *Neues Jahrbuch für Mineralogie, Monatshefte*, 4, 145–158.
- Jolivet, L. and Brun J-P., 2010. Cenozoic geodynamic evolution of the Aegean. *International Journal of Earth Sciences (Geol Rundsch)*, 99, 1, 109-138.
- Jones, C.E., Tarney, J., Baker, J.H. and Gerouki, F., 1992. Tertiary granitoids of Rhodope, Northern Greece: Magmatism related to extensional collapse of the Hellenic Orogen? *Tectonophysics*, 210, 3-4, 295-314.
- Karampelas, S., Kiefert L., 2012. Gemstones and Minerals. In Edwards, H. and Vandenabeele, P. (eds) *Analytical Archaeometry*. The Royal Society of Chemistry, Cambridge, 291-317.
- Katzir, Y., Valley, J.W., Matthews, A. and Spicuzza, M.J., 2002. Tracking fluid flow during deep crustal anatexis: metasomatism of peridotites (Naxos, Greece). *Contribution to Mineralogy and Petrology*, 142, 700-713.
- Keay, S., 1998. *The geological evolution of the Cyclades, Greece: constraints from SHRIMP U-Pb geochronology*. Ph.D. thesis, Australian National University, Canberra, Australia, 320 pp.
- Keay, S., Lister, G., and Buick, I., 2001. The timing of partial melting, Barrovian metamorphism and granite intrusion in the Naxos metamorphic core complex, Cyclades, Aegean Sea, Greece. *Tectonophysics*, 342, 3, 275-312.
- Kievlenko, E., 2003. *Geology of Gems*. Soregaroli, A. (ed.), Ocean Pictures Ltd., Littleton, Colorado, 432 pp.

- Kolocotroni, C. and Dixon, J.E., 1991. The origin and emplacement of the Vrontou granite, Serres, NE Greece. *Bulletin of Geological Society of Greece*, XXV, 1, 469-483.
- Krenn, K., Bauer, C., Proyer, A., Klötzli, U. and Hoinkes, G., 2010. Tectonometamorphic evolution of the Rhodope orogen, *Tectonics*, 29, TC4001, doi:10.1029/2009TC002513.
- Krenn, K., Bauer, C., Proyer, A., Mposkos, E. and Hoinkes, G., 2008. Fluid entrapment and reequilibration during subduction and exhumation: a case study from the high-grade Nestos shear zone, Central Rhodope, Greece. *Lithos*, 104, 1, 33-53.
- Krenn, K., Bauer, C., Proyer, A., Mposkos, E. and Hoinkes, G., 2008. Fluid entrapment and re-equilibration during subduction and exhumation: A case study from the high-grade Nestos Shear Zone, central Rhodope, Greece, *Lithos*, 104, 33-53.
- Ktenas, C., 1969. La géologie de l' île de Nikaria (rédigée des restes de l'auteur par G. Marinos). *Geological and Geophysical Researches*, Athens, 13, 57-85.
- Kydonakis, K., Brun, J-P., Sokoutis, D., 2015a. North Aegean core complexes, the gravity spreading of a thrust wedge. *Journal of Geophysical Research: Solid Earth*, 120, 595–616.
- Kydonakis, K., Brun, J-P., Sokoutis, D. and Gueydan, F., 2015b. Kinematics of Cretaceous subduction and exhumation in the western Rhodope (Chalkidiki block). *Tectonophysics*, 665, 218–235.
- Kydonakis, K., Gallagher, K., Brun, J-P., Jolivet, M., Gueydan, F. and Kostopoulos, D., 2014. Upper Cretaceous exhumation of the western Rhodope Metamorphic Province (Chalkidiki Peninsula, northern Greece). *Tectonics*, 33, 1113-1132.
- Kydonakis, K., Moulas, E., Chatzitheodoridis, E., Brun, J-P. and Kostopoulos, D., 2015c. First-report on Mesozoic eclogite-facies metamorphism preceding Barrovian overprint from the western Rhodope (Chalkidiki, northern Greece). *Lithos*, 220-223, 147-163.
- Lamb, W.M. and Valley, J.W., 1984. Metamorphism of reduced granulites in low-CO₂ vapour-free environment. *Nature*, 312, 56-58.

Lee, J. and Lister, G.S., 1992. Late Miocene ductile extension and detachment faulting, Mykonos, Greece, *Geology*, 20, 121-124.

Lewis, S., Holness, M., and Graham, C., 1998. Ion microprobe study of marble from Naxos, Greece: grain-scale fluid pathways and stable isotope equilibration during metamorphism. *Geology*, 26, 10, 935-938.

Liati, A., 1986. *Regional metamorphism and overprinting contact metamorphism of the Rhodope zone, near Xanthi (N. Greece): petrology, geochemistry, geochronology*. Ph.D. thesis, Technische Universität Braunschweig, Germany, 186 pp.

Liati, A., 1988. Corundum-and zoisite-bearing marbles in the Rhodope Zone, Xanthi area (N. Greece): Estimation of the fluid phase composition. *Mineralogy and Petrology*, 38, 1, 53-60.

Liati, A., 2005. Identification of repeated Alpine (ultra) highpressure metamorphic events by U-Pb SHRIMP geochronology and REE geochemistry of zircon: the Rhodope zone of Northern Greece. *Contributions to Mineralogy and Petrology*, 150, 6, 608-630.

Liati, A. and Seidel, E., 1994. Sapphirine and hōgbomite in overprinted kyanite-eclogites of central Rhodope, N. Greece: first evidence of granulite-facies metamorphism. *European Journal of Mineralogy*, 6, 5, 733-738.

Liati, A. and Seidel, E., 1996. Metamorphic evolution and geochemistry of kyanite eclogites in central Rhodope, Northern Greece. *Contribution to Mineralogy and Petrology*, 123, 3, 293-307.

Liati, A. and Skarpelis, N., 2004. The metabauxites of Ikaria island, Eastern Aegean, Greece. *5th International Symposium on eastern Mediterranean Geology, 14-20 April, 2004, Thessaloniki, Greece*, 1427-1430.

Liati, A., Gebauer, D. and Wysoczanski, R., 2002. U-Pb SHRIMP-dating of zircon domains from UHP garnet-rich mafic rocks and late pegmatoids in the Rhodope zone (N. Greece); evidence for Early Cretaceous crystallization and Late Cretaceous metamorphism. *Chemical Geology*, 184, 3-4, 281-299.

Marchev, P., Georgiev, S., Raicheva, R., Peytcheva, I., von Quadt, A., Ovtcharova, M. and Bonev, N., 2013. Adakitic magmatism in post-collisional setting: An example

from the Early-Middle Eocene magmatic belt in Southern Bulgaria and Northern Greece. *Lithos*, 180-181, 159-180, 10.1016/j.lithos.2013.08.024.

Marchev, P., Kibarov, P., Spikings, R., Ovtcharova, M., Márton, I. and Moritz, R., 2010. $^{40}\text{Ar}/^{39}\text{Ar}$ and U-Pb geochronology of the Iran Tepe volcanic complex, Eastern Rhodopes. *Geologica Balcanica*, 39, 3, 3-12.

Marchev, P., Raicheva, R., Downes, H., Vaselli, O., Chiaradia, M. and Moritz, R., 2004. Compositional diversity of Eocene-Oligocene basaltic magmatism in the Eastern Rhodopes, SE Bulgaria: Implications for genesis and tectonic setting, *Tectonophysics*, 393, 1-4, 301-328.

Marchev, P., von Quadt, A., Peytcheva, I. and Ovtcharova, M., 2006. The age and origin of the Chuchuliga and Rozino granites, Eastern Rhodopes. *Bulgarian National Conference "GEOSCIENCES 2006"*, 213-216.

Mattauer, M., Matte, Ph. and Jolivet, J.L., 1999. A 3D model of the India-Asia collision at late scale. *Comptes Rendus de l'Académie des Sciences, Series IIA, Earth and Planetary Sciences*, 328, 499-508.

Melfos, V. and Voudouris, P., 2017. Cenozoic metallogeny of Greece and potential for precious, critical and rare metals exploration. *Ore Geology Reviews*, 89, 1030-1057.

Menon, R.D., Santosh, M. and Yoshida, M., 1994. Gemstone mineralization in southern Kerala, India. *Journal of Geological Society of India*, 44, 241-252.

Mercier, A., Debat, P. and Saul, J.M., 1999a. Exotic origin of the ruby deposits of the Mangari area in SE Kenya. *Ore Geology Reviews*, 14, 83-104.

Mercier, A., Rakotondrazafy, M. and Ravalomandrinarivo, B., 1999b. Ruby mineralization in Southwest Madagascar. *Gondwana Research*, 2, 233-438.

Merle, O., Michon, L., Camus, G. and De Goer, A., 1998. L'extension oligocène sur la transversale septentrionale du rift du Massif Central. *Bulletin de la Société Géologique de France*, 169, 615-626.

- Mezger, K. and Okrusch, M., 1985. Metamorphism of a variegated sequence at Kallithea, Samos, Greece. *Tschermaks mineralogische und petrographische Mitteilungen*, 34, 67-82.
- Moon, A.R. and Philips, M.R., 1994. Defect clustering and color in Fe,Ti: α -Al₂O₃. *Journal of The American Ceramic Society*, 77, 2, 356-367.
- Moon, A.R. and Phillips, M.R., 1991. Defect clustering in H,Ti: α -Al₂O₃. *Journal of Physics and Chemistry of Solids*, 52, 1087-1099.
- Morrison, J. and Valley, J.W., 1988. Post-granulite facies fluid infiltration in the Adirondack Mountains. *Geology*, 16, 6, 513-516.
- Moulas, E., Kostopoulos, D., Burg, J-P. and Connolly, J., 2010. High-precision P-T estimates for retrogressed kyanite eclogites from Thermes, central Rhodope (Greece). *19th Congress of the Carpathian-Balkan Geological Association, 23-26 September, 2010, Thessaloniki, Greece, Geologica Balcanica*, 39, 263-264.
- Moulas, E., Kostopoulos, D., Connolly, J. and Burg, J-P., 2013. P-T estimates and timing of the sapphirine-bearing metamorphic overprint in kyanite eclogites from Central Rhodope, Northern Greece. *Petrology*, 21, 5, 507-521.
- Mountrakis, D., 1986. The Pelagonian Zone in Greece: A Polyphase-Deformed Fragment of the Cimmerian Continent and Its Role in the Geotectonic Evolution of the Eastern Mediterranean. *The Journal of Geology*, 94, 3, 335-347.
- Mposkos, E. and Kostopoulos, D., 2001. Diamond, former coesite and supersilicic garnet in metasedimentary rocks from the Greek Rhodope: a new ultrahigh-pressure metamorphic province established. *Earth and Planetary Science Letters*, 192, 4, 497-506.
- Mposkos, E. and Krohe, A., 2000. Petrological and structural evolution of continental high pressure (HP) metamorphic rocks in the Alpine Rhodope Domain (N. Greece). In: Panayides, I., Xenophontos, C. and Malpas, J. (eds) *Proceedings of the Third International Conference on the Geology of the Eastern Mediterranean*. Geological Survey of Cyprus, Nicosia, 2000, 221-232.

- Mposkos, E., and Krohe, A., 2001. Structural evolution and exhumation history of the Rhodope UHP-HP metamorphic province (Northern Greece). *Bulletin of the Geological Society of Greece*, 34, 75-82.
- Mposkos, E., Baziotis, I., Proyer, A. and Hoinkes, G., 2006. Dolomitic marbles from the ultra-high pressure metamorphic Kimi complex in Rhodope, N.E. Greece. *Mineralogy and Petrology*, 88, 341.
- Muhlmeister, S., Fritsch, E., Shigley, E.J., Devouard, B. and Laurs, M.B., 1998. Separating natural and synthetic rubies on the basis of trace-element chemistry. *Gems & Gemology*, 34, 2, 80-101.
- Nagel, T., Schmidt, S., Janak, M., Jahn-Awe, S., Froitzheim, N. and Georgiev, N., 2010. Significance of the Nestos Shearzone in the southern Rhodopes (Northern Greece/Southern Bulgaria). *EGU General Assembly 2010, 2-7 May, 2010, Vienna, Austria, Geophysical Research Abstracts*, 12, 10547.
- Newton R.C., 1986. Fluids of granulite facies metamorphism. In Walther, J.V. and Wood, B.J. (eds) *Fluid-rock interactions during metamorphism*. Advances in Physical Geochemistry, vol. 5, Springer Verlag, New York, 36-59.
- Newton R.C., Smith J.V. and Windley B.F., 1980. Carbonic metamorphism, granulites and crustal growth. *Nature*, 288, 45-50.
- Ockenga, E., 2000. *Petrologie und Geochemie von Metabauxiten der Zentral- und Ost-Ägäis (Griechenland)*. Ph.D. thesis, Bayerische Julius-Maximilians- Universität Würzburg, Germany.
- Okay, A.I., 2001. Stratigraphic and metamorphic inversions in the central Menderes Massif: a new structural model. *International Journal of Earth Sciences*, 89, 4, 709-727.
- Ovtcharova, M., von Quadt, A., Heinrich, C.A., Frank, M., Kaiser-Rohrmeier, M., Peytcheva, I. and Cherneva Z., 2003. Triggering of hydrothermal ore mineralization in the Central Rhodopean Core Complex (Bulgaria) - Insight from isotope and geochronological studies on tertiary magmatism and migmatization. *7th Biennial*

Meeting, Society for Geology Applied to Mineral Deposits, Mineral Exploration and Sustainable Development, Mill press, Rotterdam, 367-370.

- Ozerov, K., 1945. Form of corundum crystals as dependent upon chemical composition of medium. *Doklady Akademii Nauk SSSR*, XLVII, 49-52.
- Papanikolaou, D., 1978. Contribution to the geology of Ikaria island, Aegean Sea. *Annales Géologiques des Pays Helleniques*, 29, 1-28.
- Papanikolaou, D., 1986. *Geology of Greece*. Heptalofos, Athens, 240 pp.
- Papanikolaou, D., 1987. Tectonic evolution of the Cycladic blueschist belt (Aegean Sea, Greece). *Chemical transport in metasomatic processes*, Springer, Dordrecht, 429-450.
- Papanikolaou, D., 2013. Tectonostratigraphic models of the Alpine terranes and subduction history of the Hellenides. *Tectonophysics*, 595-596, 1-24.
- Papanikolaou, D. and Panagopoulos, G., 1981. On the structural style of Southern Rhodope (Greece). *Geologica Balcanica*, 11, 13-22.
- Pe-Piper, G., Kotopouli, C.N. and Piper, D.J., 1997. Granitoid rocks of Naxos, Greece: regional geology and petrology. *Geological Journal*, 32, 2, 153-171.
- Peretti, A. and Smith, C.P., 1993. A new type of synthetic ruby on the market, offered as hydrothermal rubies from Novosibirsk. *Australian Gemmologist*, 18, 5, 149-156.
- Peretti, A., Mullis, J., Kundig, R., 1990. Die Kaschmir-Saphire und ihr geologisches Erinnerungsvermögen. *NZZ Neue Zürcher Zeitung*, 187, 59.
- Perraki, M., Proyer, A., Mposkos, E., Kaindl, R. and Hoinkes, G., 2006. Raman micro-spectroscopy on diamond, graphite and other carbon polymorphs from the ultrahigh-pressure metamorphic Kimi Complex of the Rhodope Metamorphic Province, NE Greece. *Earth and Planetary Science Letters*, 241, 3-4, 672-685.
- Peucat, J.J., Ruffault, P., Fritsch, E., Bouhnik-Le Coz, M., Simonet, C. and Lasnier, B., 2007. Ga/Mg ratio as a new geochemical tool to differentiate magmatic from metamorphic blue sapphires, *Lithos*, 98, 261-274.

- Peytcheva, I., Kostitsin, Y., Salnikova, E., Kamenov, B. and Klain, L., 1998. Rb-Sr and U-Pb isotope data for the Rila-Rhodope batholith. *Geochemistry Mineralogy and Petrology*, 35, 93-105 (in Bulgarian, with English abstract).
- Pham Van, L., Hoáng Quang, V., Garnier, V., Giuliani, G., Ohnenstetter, D., Lhomme, T., Schwarz, D., Fallick, A.E., Dubessy, J. and Phan Trong, T., 2004. Gem corundum deposits in Vietnam. *Journal of Gemmology*, 29, 129–147.
- Phan, T.M.D., 2015. *Internal characteristics, chemical compounds and spectroscopy of sapphire as single crystals*. Ph.D. thesis, Johannes Gutenberg-Universität, Mainz, Germany, 140 pp.
- Proyer, A., Mposkos, E., Baziotis, I. and Hoinkes, G., 2008. Tracing high-pressure metamorphism in marbles: phase relations in high-grade aluminous calcite-dolomite marbles from the Greek Rhodope massif in the system CaO-MgO-Al₂O₃-SiO₂-CO₂ and indications of prior aragonite, *Lithos*, 104, 1-4, 119-130.
- Rakotondrazafi M.A.F., Giuliani, G., Ohnenstetter, D., Fallick, A.E., Rakotosamizanany, S., Andriamamonjy, A., Ralantoarison, T., Razanatseheno, M., Offant, Y., Garnier, V., Maluski, H., Dunaigre, C., Schwarz, D. and Ratrimo, V., 2008. Gem corundum deposits of Madagascar: a review. *Ore Geology Reviews*, 34, 134-154.
- Rakotondrazafi, M.A.F., Moine B., Cuney M., 1996. Mode of formation of hibonite (CaAl₁₂O₁₉) within the U-Th skarns from the granulites of S-E Madagascar. *Contributions to Mineralogy and Petrology*, 123, 190-201.
- Rakotosamizanany, S., 2003. *Les gisements de rubis de Soamiakatra: caractères minéralogiques-gemmologiques-conditions de formation (au Sud d'Antanifotsy)*. M.Sc. thesis, University of Antananarivo, Madagascar, 74 pp.
- Reischmann, T. and Kostopoulos, D., 2002. Timing of UHPM in metasediments from the Rhodope Massif, N. Greece. *Goldschmidt Conference Abstracts 2002*, A634.
- Ring, U., 2007. The Geology of Ikaria Island: the Messaria extensional shear zone, granites and the exotic Ikaria nappe. *Journal of the Virtual Explorer*, 27, Paper 3.
- Ring, U. and Layer, P.W., 2003. High-pressure metamorphism in the Aegean, eastern Mediterranean: underplating and exhumation from the Late Cretaceous until the

Miocene to Recent above the retreating Hellenic subduction zone. *Tectonics*, 22, 3, doi:10.1029/2001TC001350.

Ring, U., Glodny, J. and Thomson, S., 2010. The Hellenic subduction system: high-pressure metamorphism, exhumation, normal faulting and large-scale extension. *Annual Review of Earth and Planetary Sciences*, 38, 45-76.

Ring, U., Glodny, J., Will, T. and Thomson, S., 2007. An Oligocene extrusion wedge of blueschist-facies nappes on Evia, Aegean Sea, Greece: implications for the early exhumation of high-pressure rocks. *Journal of the Geological Society of London*, 164, 637-652.

Royden, L.H. and Papanikolaou, D.J., 2011. Slab segmentation and late Cenozoic disruption of the Hellenic arc. *Geochemistry, Geophysics, Geosystems*, 12, 3, doi:10.1029/2010GC003280.

Rupasinghe, M.S. and Dissanayake, C.B., 1985. Charnockites and the genesis of gem minerals, *Chemical Geology*, 53, 1-16.

Sackler, A., 2003. *Scientific Examination of Art - Modern techniques in conservation and analysis*. The National Academy Press, Washington DC, doi.org/10.17226/11413.

Santosh, M. and Collins, A., S., 2003. Gemstone mineralization in the Palghat-Cauvery shear zone system (Kakur-Kangayam belt), Southern India. *Gondwana Research*, 6, 911-918.

Schmetzer, K., 1987. Zur Deutung der Farbursache blauer Sapphire - eine Diskussion. *Neues Jahrbuch für Mineralogie, Monatshefte*, 8, 337-343.

Schmetzer, K., Bosshard, G. and Hänni, H.A., 1982. Naturfarbene und behandelte gelbe und orange-braune Sapphire. *Zeitschrift der Deutschen Gemmologischen Gesellschaft*, 31, 4, 265-279.

Schmetzer, K., Bosshard, G. and Hänni, H.A., 1983. Naturally coloured and treated yellow and orange-brown sapphires. *Journal of Gemmology*, 18, 607-622.

- Schmidt, S., Nagel, T.J. and Froitzheim, N., 2010. A new occurrence of microdiamond-bearing metamorphic rocks, SW Rhodopes, Greece. *European Journal of Mineralogy*, 22, 189-198.
- Schuiling, R.D. and Kreulen, R., 1979. Are thermal domes heated by CO₂-rich fluids from the mantle? *Earth and Planetary Science Letters*, 43, 2, 298-302.
- Schumann, W., 2001. *Gemstones of the world*. Robert Hale Ltd, London, 280 pp.
- Schwarz, D., 1998. Aus Basalten, Marmoren und Pegmatiten. Spezielle Ursachen formten in der Erdkruste edle Rubine und Saphire. In Weise, C. (ed) *Rubin, Saphir, Korund: schön, hart, selten, kostbar*. ExtraLapis, 15, 5-9.
- Schwarz, D., Kanis, J. and Schmetzer, K., 2000. Sapphires from Antsirananana Province, Northern Madagascar. *Gems & Gemology*, 36, 3, 216-233.
- Schwarz, D., Pardieu, V., Saul, J.M., Schmetzer, K., Laus, B.M., Giuliani, G., Klemm, L., Malsy, A., Erel, E., Hauzenberger, C., Toit, G.D., Fallick, A.E. and Ohnenstetter, D., 2008. Rubies and Sapphires from Winza, Central Tanzania, *Gems & Gemology*, 44, 4, 322-347.
- Shigley, J.E., Wang, W., Bordelon, O. and Kane, R.E., 2003. Beryllium diffusion of ruby and sapphire, *Gems & Gemology*, 3, 2, 84-135.
- Simonet, C., Fritsch, E. and Lasnier, B., 2008. A classification of gem corundum deposits aimed towards gem exploration. *Ore Geology Reviews*, 34, 127-133.
- Simonet, C., Paquette, J.L., Pin, C., Lasnier, B. and Fritsch, E., 2004. The Dusi (Garba Tula) sapphire deposit, Central Kenya - a unique Pan-African corundum-bearing monzonite. *Journal of African Earth Sciences*, 38, 401-410.
- Skarpelis, N., Kyriakopoulos, K. and Villa, I., 1992. Occurrence and ⁴⁰Ar/³⁹Ar dating of a granite in Thera (Santorini, Greece). *Geologische Rundschau*, 81, 3, 729-735.
- Skoog, D.A., Holler, J.F., Crouch, S.R., 2000. *Chimica analitica strumentale*. Sabbatini, L. (ed.), Edises, 1054 pp.
- Smith, C.P., 1995. A contribution to understanding the infrared spectra of rubies from Mong Hsu, Myanmar. *Journal of Gemmology*, 24, 5, 321-335.

Smith, C.P., 2010. Inside sapphires. *Rapport Magazine*, 33, 7, 123-132.

Smith, C.P., Kammerling, R.C., Keller, A.S., Peretti A., Scarratt, K.V., Khoa, N.D. and Repetto, S., 1995. Sapphires from southern Vietnam, *Gems & Gemology*, 31, 3, 168-186.

Soldatos, T., Koroneos, A., Christofides, G. and del Moro, A., 2001. Geochronology and origin of the Elatia plutonite (Hellenic Rhodope Massif, N. Greece) constrained by new Sr isotopic data. *Neues Jahrbuch für Mineralogie, Abhandlungen*, 176, 2, 179-209.

Soldatos, T., Koroneos, A., Kamenov, B., Peytcheva, I., von Quadt, A., Christofides, G., Zheng, X. and Sang, H., 2008. New U-Pb and Ar-Ar mineral ages for the Barutin-Buynovo-Elatia-Skaloti-Paranesti batholith (Bulgaria and Greece): refinement of its debatable age. *Geochemistry Mineralogy and Petrology*, 46, 85-102.

Spanos, D., Koukouvelas, I., Kokkalas, S. and Xypolias, P., 2010. Patterns of ductile deformation in Attico-Cycladic Massif. *Bulletin of the Geological Society of Greece*, 43, 1, 368-378.

Srithai, B. and Rankin, A.H., 1999. Fluid inclusion characteristics of sapphires from Thailand. In: *Mineral Deposits: Stanley, C.J. (ed) Processes to Processing*. Proceedings of the Fifth Biennial SGA Meeting and the Tenth Quadrennial IAGOD Symposium, 22-25 August, 1999, London, 107-110.

Steppan, N., Kalt, A., and Altherr, R., 2002. Partitioning of Li, Be and B between minerals in metapelitic rocks-case studies of Ikaria Island (Greece), Kunisches Gebirge (Germany), Campo Tencia (Swiss Alps). *Goldschmidt Conference Abstracts 2002*, A740.

Stern, R.J., Tsujimori, T., Harlow, G., and Groat, L.A., 2013. Plate tectonic gemstones, *Geology*, 41, 7, 723-726.

Sutherland, F.L., Coenraads, R.R., Schwarz, D., Raynor, L.R., Barron, B.J., Webb, G.B., 2003. Al-rich diopside in alluvial ruby and corundum-bearing xenoliths, Australian and SE Asian basalt field. *Mineralogical Magazine*, 67, 717-732.

Sutherland, F.L., Schwarz, D., Jobbins, E.A., Coenraads, R.R., Webb, G., 1998.

Distinctive gem corundum from discrete basalt fields: a comparative study of Barrington, Australia, and west Pailin, Cambodia gem fields. *Journal of Gemmology*, 26, 65-85.

Sutherland, F.L., Zaw, K., Meffre, S., Giuliani, G., Fallick, A.E., Graham, I.T. and Webb, G.B., 2009. Gem corundum megacrysts from East Australia basalt fields: trace elements, O isotopes and origins, *Australian Journal of Earth Sciences*, 56, 1003-1020.

Theophrastus, 1956 [315 BC]. *Theophrastus On Stones: Introduction, Greek text, English translation, and Commentary*. Ohio State University, Columbus, Ohio, 238 pp. (translated by Caley, E.R. and Richards, J.F.C.).

Tomaschek, F., Kennedy, A.K., Villa, I.M., Lagos, M. and Ballhaus, C., 2003. Zircons from Syros, Cyclades, Greece - recrystallization and mobilization of zircon during high-pressure metamorphism. *Journal of Petrology*, 44, 1977-2002.

Touret J.L.R., 1971. Le facies granulite en Norvege meridionale. II. Les inclusions fluids. *Lithos*, 4, 423-436.

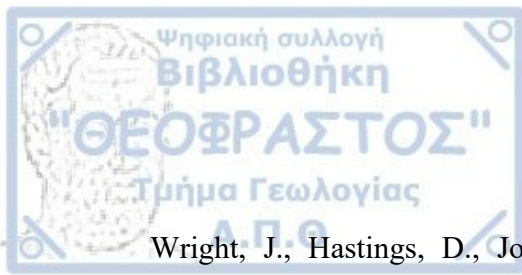
Turpaud, P., 2006. *Characterization of igneous terranes by zircon dating: implications for the UHP relics occurrences and suture identification in the Central Rhodope, Northern Greece*. Ph.D. thesis, Johannes-Gutenberg Universität, Mainz, Germany, 107 pp.

Turpaud, P. and Reischmann, T., 2010. Characterization of igneous terranes by zircon dating: implications for UHP occurrences and suture identification in the Central Rhodope, Northern Greece. *International Journal of Earth Sciences (Geol Rundsch)*, 99, 3, 567-591.

Urai, J.L. and Feenstra, A., 2001. Weakening associated with the diaspore-corundum dehydration reaction in metabauxites: an example from Naxos (Greece). *Journal of Structural Geology*, 23, 6, 941-950.

Urai, J.L., Schuiling, R.D., and Jansen, J.B.H., 1990. Alpine deformation on Naxos (Greece). *Geological Society of London, Special Publications*, 54, 1, 509-522.

- van der Maar, P.A. and Jansen, J.B.H., 1983. The geology of the polymetamorphic complex of Ios, Cyclades, Greece and its significance for the Cycladic Massif. *Geologische Rundschau*, 72, 1, 283-299.
- van Hinsbergen, D.J.J., Hafkenscheid, E., Spakman, W., Meulenkamp, J.E. and Wortel, R., 2005. Nappe stacking resulting from subduction of oceanic and continental lithosphere below Greece. *Geology*, 33, 4, 325-328.
- Volynets, F.K., Sidorova, E.A. and Stsepuro, N.A., 1972. OH-groups in corundum crystals which were grown with the Verneille technique. *Journal of Applied Spectroscopy*, 17, 6, 1626-1628.
- Volynets, F.K., Vorobev, V.G., and Sidorova, E.A., 1969. Infrared absorption bands in corundum crystals. *Journal of Applied Spectroscopy*, 10, 6, 665-667.
- Voudouris, P., 2010. Gemstones and Mineral-megacrysts in Greece. *Presentation*, University New South Wales, Sydney, Australia, doi:10.13140/RG.2.2.11525.04323.
- Voudouris, P., Graham, I., Melfos, V., Zaw, K., Lin, S., Giuliani, G., Fallick, A. and Ionescu, M., 2010. Gem corundum deposits of Greece: diversity, chemistry and origins. *Proceedings of the 13th Quadrennial IAGOD Symposium, Adelaide, Australia*, 69, 429-430.
- Walton, L., 2004. Exploration criteria for coloured gemstone deposits in the Yukon. *Yukon Geological Survey*, Open file 2004-10, May 2004.
- Wang, K.K., Graham, I.T., Lay, A., Harris, S.J., Cohen, D.R., Voudouris, P., Belousova, E., Giuliani, G., Fallick, A.E. and Greig, A., 2017. The origin of a new pargasite-schist hosted ruby deposit from Paranesti, Northern Greece. *The Canadian Mineralogist*, 55, 535-560.
- Weidmann, M., Solounias, N., Drake, R.E. and Curtis, G.H., 1984. Neogene stratigraphy of eastern basin, Samos Island, Greece. *Geobios*, 17, 477-490.
- Wijbrans, J.R., Schliestedt, M. and York, D., 1990. Single grain argon laser probe dating of phengites from the blueschist to greenschist transition on Sifnos (Cyclades, Greece). *Contributions to Mineralogy and Petrology*, 104, 582-593.



Wright, J., Hastings, D., Jones, W. and Williams, H., 1985. *Geology and mineral resources of West Africa*. Allen & Unwin, London, 187 pp.

Wybrans, J.R. and McDougall, I., 1988. Metamorphic evolution of the Attic Cycladic Metamorphic Belt on Naxos (Cyclades, Greece) utilizing $^{40}\text{Ar}/^{39}\text{Ar}$ age spectrum measurements. *Journal of Metamorphic Geology*, 6, 571-594.

Yager, T.R., Menzie, W.D., and Olson, D.W., 2008. Weight of production of emeralds, rubies, sapphires, and tanzanite from 1995 through 2005. *U.S. Geological Survey, Open-File Report 2008-1013*, 9 p., available only online, <http://pubs.usgs.gov/of/2008/1013>.

Web pages

Block Engineering

Block Engineering: Quantum Cascade Laser (QCL) Technology Overview, 2017.

<http://blockeng.com/technology/ftirtechnology.html>

(retrieved February 2, 2016).

Gemdat.org

Ruby, Ruby gemstone information, 2017.

<https://www.gemdat.org/gem-3473.html>

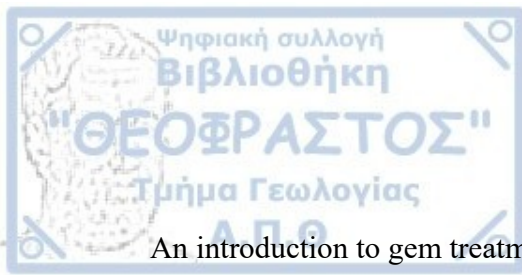
(retrieved June 16, 2017).

Sapphire, Sapphire gemstone information, 2017.

<https://www.gemdat.org/gem-3529.html>

(retrieved June 15, 2017).

Gia.edu:



An introduction to gem treatments, 2017.

<https://www.gia.edu/gem-treatment>

(retrieved June 15, 2017).

Ruby gemstone- Ruby stone- GIA, 2017.

<https://www.gia.edu/ruby>

(retrieved June 26, 2017).

Ruby history and lore., 2017.

<https://www.gia.edu/ruby-history-lore>

(retrieved June 26, 2017).

Ruby quality factors, 2017.

<https://www.gia.edu/ruby-quality-factor>

(retrieved June 21, 2017).

Sapphire gemstone- Sapphire stone- GIA, 2017.

<https://www.gia.edu/sapphire>

(retrieved June 26, 2017).

Sapphire history and lore, 2017.

<https://www.gia.edu/sapphire-history-lore>

(retrieved June 26, 2017).

Sapphire quality factors, 2017.

<https://www.gia.edu/sapphire-quality-factor>

(retrieved June 21, 2017).

Microscopy News

Operating Manual Axioskop 40 / Axioskop 40 FL Routine microscope, 2001.

https://microscopy-news.com/download-center2/Axioskop_40_Axioskop_40_FL_Routine_Microscope_e.pdf

(retrieved November 4, 2017).



The precious gemstone ruby, Ruby: The gemstone ruby information and pictures, 2017.

http://www.minerals.net/gemstone/ruby_gemstone.aspx

(retrieved June 26, 2017).

The precious gemstone sapphire, Sapphire: The gemstone sapphire information and pictures, 2017.

http://www.minerals.net/gemstone/sapphire_gemstone.aspx

(retrieved June 26, 2017).

The mineral corundum, 2017.

<http://www.minerals.net/mineral/corundum.aspx?img=/Image/16/51/Corundum.aspx>

(retrieved November 4, 2017).

Mindat.org

Ruby, 2017.

<https://www.mindat.org/min-3473.html>

(retrieved November 4, 2017).

MSU Chemistry

Visible and Ultraviolet Spectroscopy. Reusch, 2013.

<https://www2.chemistry.msu.edu/faculty/reusch/virttxtjml/Spectrpy/UV-Vis/spectrum.htm>

(retrieved November 4, 2017).

FMF- Minerals Forum

FMF - Friends of Minerals Forum, discussion and message board, 2017.

<http://www.mineral-forum.com/message-board/viewtopic.php?p=32483>

(retrieved November 4, 2017).



Synthetic sapphires, Sapphire.com, 2017.

<http://www.chm.bris.ac.uk/webprojects2004/hall/synthetic.htm>

(retrieved June 16, 2017).



